Mechano-synthesis and degradation of an equimolar Li-Sn alloy

Sara Sofia dos Santos Elias

Thesis to obtain Master of Science Degree in

Materials Engineering

Supervisors: Professor Alberto Eduardo Morão Cabral Ferro
Doctor Rodrigo Clemente Velez Mateus

Examination Committee

Chairperson: José Paulo Sequeira Farinha
Supervisor: Professor Alberto Eduardo Morão Cabral Ferro
Member of the Committee: António Cândido Lampreia Pereira Gonçalves

May 2022

Declaration

I declare that this document is an original work of my own authorship and that it fulfils all the requirements of the Code of Conduct and Good Practices of the Universidade de Lisboa.

Declaração

Declaro que o presente documento é um trabalho original da minha autoria e que cumpre todos os requisitos do Código de Conduta e Boas Práticas da Universidade de Lisboa.

Acknowledgments

I would like to acknowledge the Foundation for Science and Technology (FCT, Portugal) for the financial support under projects UIDB/04540/2020 (CeFEMA) and PTDC/FIS-PLA/31629/2017-LMWALLS.

A special acknowledge to Makin Metal Powders Ltd for supplying the tin powder used in this work.

To my thesis supervisor, Professor Alberto Ferro, I am profoundly grateful for always having believed in my abilities, always encouraging me to go beyond and to get out of my comfort zone. If it were not for his constant push and dedication, I would not have grown and achieved as much as I did. I will carry all the knowledge, methodologies, and rigorous scientific thinking passed on to me for the rest of my life.

My sincere gratitude to my co-supervisor Dr. Rodrigo Mateus, for his guidance and availability to help me with all the necessary procedure for IBA analysis.

A special thank you to Professor Mafalda Guedes for all the help with the techniques used in this work, for the borrowed books, and availability to answer my questions whenever necessary.

I would also like to thank CQE-IST X-RAY Diffraction Facilities laboratory and, in particular, Dr. Auguste Fernandes for all the X-ray diffraction knowledge transmitted to me.

I would also like to mention Pedro Teixeira, from LEM2 laboratory, for all the help designing the screw press machine used in this work.

I express my profound gratefulness to Miguel, my “adopted supervisor”, for always being one phone message away. Thank you for all the zoom calls, insightful advice, honest reviews, and scientific debates.

My sincerest gratitude to my mom and my dad, for all the efforts and sacrifices, all the love and support, and for the values of humility and hard work instilled in me. To my sister, for always being there for me.

Last but not least, to all of my IST colleagues, especially Carlota, Raposo, Inês, Brito, and João for their friendship which helped me keep my sanity throughout these years at IST.

Abstract

Lithium-Tin (Li-Sn) alloys are an attractive solution for plasma facing components of nuclear fusion reactors and have received considerable attention regarding lithium-ion batteries. Mechano-synthesis, via high energy milling, has been demonstrated to be an effective method to produce prototype Li-Sn alloys. However, due to the large number of parameters involved in this processing route, their effects on the final microstructure and composition of the alloys remain relatively understudied. The description and understanding of the reaction path remain rather incomplete.

In this work, the impact of the milling rate (150 rpm and 500 rpm) and milling ball diameter (6 mm, 10 mm, and 15 mm) on the final microstructure of an equimolar Li-Sn alloy is studied. Milling times from 0.5 h to 64 h are tested. The resultant phase composition was assessed in detail by a combination of ion beam analysis, X-ray diffraction, differential scanning calorimetry, and gravimetric analysis.

Milling rate is the milling parameter presenting the major effect on reaction kinetics. Milling experiments at 500 rpm, using 10 mm balls, presented the highest milling efficiency (milling mass yield, y_M ~ 86%), and resulted in the most homogeneous equimolar alloy, with LiSn as the major phase.

Mechano-synthesis progresses in two fronts: Li-rich Li-Sn intermetallics preferentially form at the surface of the initial (Li) cuts, whereas Sn-rich Li-Sn intermetallics preferentially form at the surface of the original β-Sn powders. These two fronts converge, at a later stage, to a base LiSn composition, with Li_2Sn_5 and possibly with small crystallite size Li-rich Li-Sn intermetallics.

Keywords: Li-Sn alloys; Mechano-synthesis; Oxidation; X-ray Diffraction.

Resumo

As ligas de Lítio-Estanho (Li-Sn) são uma solução para a formação de paredes líquidas de contenção do plasma em reatores de fusão nuclear. Estas têm também recebido atenção considerável na área das baterias de iões de Lítio. A eficácia da mecano-síntese, por moagem mecânica de alta energia, para produção de ligas Li-Sn foi já demonstrada. Contudo, devido ao número elevado de parâmetros envolvidos no processo, o seu efeito na microestrutura e composição permanece pouco estudado. O conhecimento do caminho de reação é ainda bastante incompleto.

Nesta tese, estuda-se o impacto da velocidade de moagem (150 rpm e 500 rpm) e do diâmetro das esferas (6 mm, 10 mm e 15 mm) na microestrutura final de uma liga Li-Sn equimolar. Estudam-se tempos de moagem entre 0.5 h e 64 h. A caracterização da composição fásica foi realizada por análise de feixe de iões, difração de raios-X, calorimetria diferencial de varrimento e análise gravimétrica.

A taxa de moagem é o parâmetro que mais influencia a cinética de reação. Moagens com 500 rpm, utilizando esferas de 10 mm, foram as mais eficientes (rendimento y_M ~ 86%), tendo resultado numa liga homogénea, cuja principal fase constituinte é o LiSn.

A síntese mecânica progride em duas frentes: preferencialmente, os intermetálicos Li-Sn ricos em Li formam-se na superfície dos pedaços iniciais de (Li), enquanto os ricos em Sn se formam na superfície dos pós inicias de β-Sn. À medida que a moagem progride, estas duas frentes convergem até se atingir uma composição base de LiSn, com Li_2Sn_5 e, eventualmente, intermetálicos Li-Sn ricos em Li, com tamanho de cristalite reduzido.

Palavras-chave: Ligas Li-Sn; Mecano-síntese; Oxidação; Difração de raios-X.

Table of Contents

List of Figures

List of Tables

List of Acronyms

AIRSS - *Ab Initio* Random Structure Searching
BPR - Ball-To-Powder Weight Ratio
CIF - Crystallographic Information Files
COD - Crystallographic Open Database
CPS - Capillary Porous Systems
CTN – Campus Tecnológico e Nuclear
DEM - Discrete Element Method
DFT - Density Functional Theory
DIFFER - Dutch Institute For Fundamental Energy Research
DSC – Differential Scanning Calorimetry
ERDA - Elastic Recoil Detection Analysis
IBA - Ion Beam Analysis
ICP-AES – Inductively Coupled Plasma Atomic Emission Spectroscopy
ICP-OES - Inductively Coupled Plasma Optical Emission Spectroscopy
IST - Instituto Superior Técnico
ISTTOK – Instituto Superior Técnico Tokamak
MA - Mechanical Alloying
MD - Molecular Dynamics
MM - Mechanical Milling
MS - Mechano-Synthesis
NRA - Nuclear Reaction Analysis
NTP – Normal Temperature and Pressure
ODS - Oxide Dispersion Strengthen
PIXE - Particle Induced X-ray Emission
RBS - Rutherford Backscattering Spectrometry
RM - Reaction Milling
SEM – Scanning Electron Microscopy
GA - Thermogravimetric Analysis
XRD – X-Ray Diffraction

List of Symbols

A – Ampere
θ – Angle of incident beam
Å – Angstrom
Z – Atomic number
at. % - Atomic percentage
º - Degree
º C - Degree Celsius
cm - Centimetre
c.p.s. – Counts per second
eV – Electron-Volt
G – Giga (10^9)
g – Gram
h – Hour
k – Kilo
M – Mega (10^6)
m – Meter
μ – Micro
μm – Micron
mL – Millilitre
mm – Millimetre
ms – Millisecond
min – Minute
nm - Nanometre
N – Newton
ppm – Parts per million
Pa – Pascal
p – Proton
Q – Cumulative charge
rpm - Rotations per minute
s – Second
V - Volt
wt - Weight
wt. % - Weight percentage

Chapter 1. Introduction

During the past few decades, Lithium-Tin (Li-Sn) alloys have received considerable attention regarding lithium-ion batteries [1]. Recently, they have also been identified as attractive candidates for plasma facing components of fusion nuclear reactors [2]. However, production of these alloys presents some challenges: the chemical reactivity of Li must be mitigated, requiring special conditions during processing to avoid sample contamination, and the formation of stable high melting temperature Li-rich Li-Sn intermetallics, which must be prevented. Mechano-synthesis, via high energy milling, is an alternative method to casting [3–11] to produce prototype Li-Sn alloys, allowing access to a wider range of compositions and microstructures. Mechano-synthesis has been demonstrated to be an effective technique for production of Li-Sn alloys with Li content up to 50 at.% [12–16]. Nevertheless, the predominant cold-welding behaviour of these alloys results in a low milling mass yield, and, due to the large number of parameters involved in this processing route, their effects on the final microstructure and composition remain relatively understudied. The description and understanding of the reaction path during mechano-synthesis remains rather incomplete.

This thesis aims at producing an equimolar Li-Sn alloy, for later production of Li-Sn alloys with Li content below 5 at. % to be exposed to deuterium plasmas in ISTTOK, sited at Instituto Superior Técnico (IST), and in MAGNUM-PSI facilities, sited at the Dutch Institute for Fundamental Energy Research (DIFFER). It has the following objectives:

- Study the impact of the milling rate and milling ball diameter on the final microstructure and composition of the equimolar Li-Sn alloy;
- Describe the reaction path during mechano-synthesis;
- Identify the milling parameters (milling rate, and milling ball diameter) which result in both the highest milling mass yield and the most homogenous equimolar Li-Sn alloy;
- Study the equimolar Li-Sn alloy chemical reactivity in air environment and assess the feasibility of X-ray diffraction use to characterize the alloys produced.

This thesis consists of 6 chapters. Chapter 1. Introduction, where the context, motivation, and objectives of the present work are introduced. Chapter 2. State-of-the-art, reviews the Lithium-Tin alloy system, namely the structure and mechanical properties of Li-Sn phases, and the different production and characterization techniques referred in literature. This chapter also provides an overview of Tin and Lithium properties, important for their handling and high energy milling processing, and an overview of the working principles of mechano-synthesis of metallic powders. Chapter 3. Experimental techniques and procedures, describes in detail the materials used, along with the experimental procedure carried out for alloy production and characterization. In Chapter 4. Results and Discussion, the experimental results are critically analysed and discussed. Chapter 5. Conclusions and Future Work, depicts the final conclusions of this work and presents some guidelines for future work in the subject of Li-Sn alloy production. Bibliography, lists the sources and references used in this work.

Chapter 2. State-of-the-art

This chapter depicts the current relevant knowledge about the topic of the present thesis, together with a review of the fundamental concepts discussed in this work. Section 2.1. Tin (Sn) and 2.2. Lithium (Li) delve into Tin and Lithium physical, chemical, and mechanical properties, important for their handling and high energy milling processing. Section 2.3. Lithium-Tin (Li-Sn) alloys reviews the Lithium-Tin alloy system, namely the structure and mechanical properties of Li-Sn phases, and the different production and characterization techniques referred in literature. Section 2.4. Mechano-synthesis of metallic powders (MS) provides an overview of the working principles of mechano-synthesis of metallic powders.

2.1. Tin (Sn)

This section addresses Sn physical, chemical, and mechanical properties, at atmospheric pressure and in the working temperature range of the present work (> 25 º C), important for its handling and high energy milling processing.

2.1.1. Physical and chemical properties of Tin (Sn)

Sn is a low melting point metal (231.9 ºC) [17]. When exposed to air, pure Sn oxidizes, forming a stable passivation layer of tin oxides at its surface. As a result of the dual valency of Sn, which has oxidation states of 2+ and 4+, there are two main oxides of Sn that can form: stannous oxide (SnO) and stannic oxide (SnO_2) [18,19]. Surface passivation layer formation starts with SnO growth, which is followed by SnO_2 formation. Ambient passivation layer thickness is usually in the range 20-40 Å [18].

2.1.2. Microstructure and mechanical properties of Tin (Sn)

At atmospheric pressure, Sn has two allotropic forms [20]: β-Sn (white tin) and α-Sn (grey tin). β-Sn is stable above 13 ºC and has a body-centred tetragonal crystal structure, with a room temperature density of 7.31 g/cm^3 [20]. α-Sn has a cubic diamond crystal structure, with a room temperature density of 5.77 g/cm^3, and is stable below 13 ºC [20].

In the working temperature range of the present work (> 25 ºC), β-Sn is the stable allotropic. The mechanical properties of tetragonal β-Sn have been extensively studied, particularly by creep tests [21–25]. It is general agree that the main deformation mechanisms in β-Sn are slip and twinning [25].

For metals with a low melting point, both dynamic recovery and recrystallization play an important role during mechano-synthesis. When milling ductile powders with low melting points, milling can occur at high homologous temperature, T_M^*, associated with hot-working in metals (homologous temperature of 0.59 ~ 0.6 [26]). Assuming a conservative milling temperature of 30 ºC, $T_{\beta-Sn}^* = 0.60$, β-Sn presents dynamic recrystallization when strained [24,27,28] and static recovery when the stress is removed [22].

In the early stages of deformation, for temperatures up to 74.85 ºC, Sn exhibits a small work hardening [22]. Thereafter, a constant flow stress is observed. At room temperature, only for strain rates as high as 1 ms^{-1}, some work hardening takes place [22].

2.2. Lithium (Li)

In this section, Li physical, chemical, and mechanical properties, at atmospheric pressure and in the working temperature range of the present work (> 25 º C), important for its handling and high energy milling processing, are addressed.

2.2.1. Physical and chemical properties of Lithium (Li)

Li is a metal with low melting point (180.5 ºC) [29]. Due to its high reactivity toward atmospheric gases, and depending on the processing method, Li often presents a native surface film consisting of LiOH and/or Li_2CO_3 on top of Li_2O, with thicknesses in the range of a few tenths to one hundred nanometres [30,31]. Li promptly reacts with moisture leading to the formation of LiOH (dark cusp), whose affinity for carbon dioxide leads to the subsequent formation of Li_2CO_3 (white tone) [32]. Similarly, Li has an inherent reactivity towards nitrogen, forming Li_3N, albeit the reason for such behaviour still remains poorly understood [30]. However, contradicting results have been reported on Li reactivity towards oxygen. Some studies reveal a high reaction rate when clean lithium surfaces are exposed to oxygen [33,34], while others suggest negligible reactivity with little formation of Li_2O (white tone) [35,36]. For these reasons, Li should be handled under controlled atmosphere and be thoroughly scraped before use to remove the native film from the surface.

Li has a reduction action when melted [37] or milled [38] with SnO. In the initial stages of milling, Li metal reduces SnO to Sn [38]. Li diffusion coefficients in Li-Sn were calculated using Density Functional Theory (DFT) to be in the range between 10^{-12}-10^{-11} m^2s^{-1}, at room temperature, which is in agreement with experimental results [39].

2.2.2. Microstructure and mechanical properties of Lithium (Li)

Li has two allotropic forms: (Li) and β-Li. (Li) is stable above -203.15 ºC and has a body-centred cubic crystal structure. β-Li has a hexagonal closed packed crystal structure, being stable below that temperature [40].

Masias *et al.* [41] characterized the mechanical properties of (Li) at room temperature. Using a pulse-echo ultrasonic technique, Young's modulus, shear modulus, and Poisson's ratio were estimated to be 7.82 GPa, 2.83 GPa, and 0.381, respectively. The stress-strain behaviour in tension and compression were studied in an inert atmosphere. The values measured for the yield strength in tension and compression were 0.73 and 0.81 MPa, respectively. Previous studies on (Li) mechanical properties have shown that it is a very ductile metal at room. At room temperature, and for low strain rates, (Li) exhibits elongations as high as 50% before fracture.

2.3. Lithium-Tin (Li-Sn) alloys

For the past few decades, the Li-Sn system has received renewed attention since Li-Sn alloys are seen as potential candidates for replacing graphite anodes in Li-ion batteries [1]. As such, several thermodynamic studies can be found in the literature, namely: reviews [42–46]; experimental studies [7,46–50]; *ab initio* simulations of the voltage profile [47]; *ab initio* random structure searching (AIRSS) and species swapping methods [51]; Density Functional Theory (DFT) investigations [39,52–55]; and CALPHAD modelling studies [3,7,45,56]. The reader is referred to a recent review on the Li-Sn system phase diagram by Wang *et al.* [45] for a more detailed description of the works developed on this topic. There are still some discrepancies between calculated data by different studies, and uncertainties regarding the Li-rich part of the phase diagram at high temperatures.

This section reviews the Li-Sn alloy system, namely the structure and mechanical properties of Li-Sn phases, and the different production and characterization techniques referred in literature.

2.3.1. Li-Sn phase diagram and structure of Li-Sn intermetallics

The 1996 published Li-Sn phase diagram (Figure 2.1) shows the existence of seven intermetallics: Li_2Sn_5, LiSn, Li_7Sn_3, Li_5Sn_2, $Li_{13}Sn_5$, Li_7Sn_2, and $Li_{17}Sn_4$. The structure of the intermetallic of highest Li-content had long been under debate regarding its stoichiometry: $Li_{22}Sn_5$ was the initial suggestion, being later changed to $Li_{17}Sn_4$ [37]. Lupu *et. al* [37] investigated $Li_{22}Sn_5$ structure using X-ray and Neutron diffraction, and reported that $Li_{22}Sn_5$ has a complex cubic crystal structure with the formula of $Li_{341}Sn_{80}$ ($Li_{17}Sn_4$ for sake of simplicity). Nevertheless, ICDD databases still provide reference cards for both $Li_{22}Sn_5$ [57] and $Li_{17}Sn_4$ [58]. In the present work, $Li_{17}Sn_4$ is used as the high Li content intermetallic phase. Table 2.1 summarizes the structural information of Li-Sn phases available in literature.

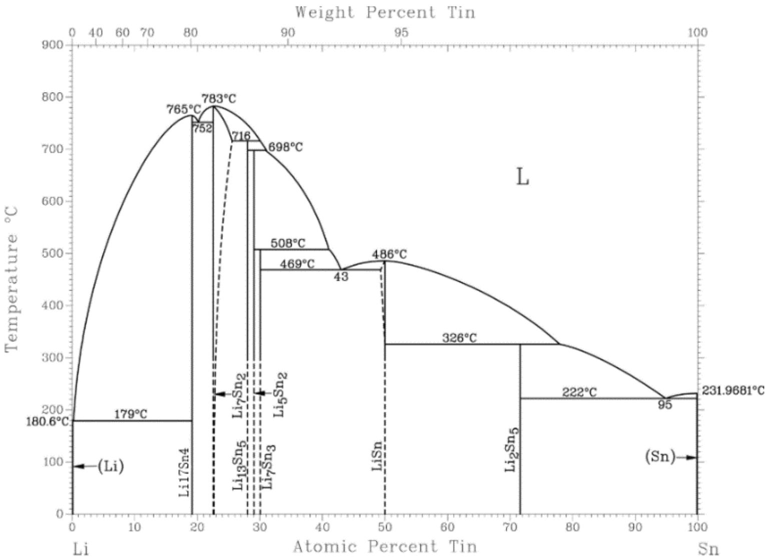

Figure 2.1 - Li-Sn binary phase diagram, adapted from [59].

Table 2.1 - Structure of Li-Sn phases.

Phase	Space Group	Structure	a (Å)	b (Å)	c (Å)	α (º)	β (º)	γ (º)	V (Å^3)	Ref.
β-Sn	I4$_1$/*amd*	body-centred tetragonal	5.792–5.953	5.792–5.953	3.122–3.217	90	90	90	104.78 – 113.59	[60–63]*, [52–54,64]**
Li$_2$Sn$_5$	P4/*mbm*	tetragonal	10.250-10.366	10.250-10.366	2.978-3.169	90	90	90	329.86-338.33	[65]*, [52–54,64]**
LiSn	P2/*m*	monoclinic	5.072-6.993	7.774-7.972	3.032-4.419	90	104.5	90	123.20-126.65	[66]*, [52–54,64]**
Li$_7$Sn$_3$	P2$_1$/*m*	monoclinic	8.228-9.495	8.536-9.450	4.614-4.742	90	105.9	90	367.111-370.120	[67]*, [52–54,64]**
Li$_5$Sn$_2$	R-3*m*	trigonal-rhomboedric	3.183-4.741	3.183-4.741	19.256-19.855	90	90	120	383.75-386.42	[68]*, [52–54,64]**
Li$_{13}$Sn$_5$	P-3*m*1	trigonal	4.569-4.703	4.569-4.703	16.619-17.130	90	90	120	327.514-328.140	[69]*, [52–54,64]**
Li$_7$Sn$_2$	Cmmm	orthorhombic	8.818-9.924	13.838-9.924	4.593-4.752	90	90	90	642.00-654.54	[70]*, [52–54,64]**
Li$_{17}$Sn$_4$	F-43*m*	superstructure of 216 bcc subcells	13.907-19.694	13.907-19.694	13.907-19.694	90	90	90	7608.27-7638.18	[37]*, [52–54,64]**
(Li)	Im3m	bcc	3.436-3.513	3.436-3.513	3.436-3.513	90	90	90	40.57-40.71	[71,72]*, [52–54,64]**

*Experimental data, **Computed data using Density Functional Theory (DFT).

2.3.2. Mechanical properties of Li-Sn intermetallics

Albeit the current interest of Li-Sn system, the mechanical properties of its intermetallics remain a relatively understudied topic. So far, only the elastic behaviour has been studied by first-principle studies based on DFT [39,52–55,64]. Table 2.2 sums up the room temperature Hill[1] values obtained for bulk modulus (K), Young's modulus (E), shear modulus (G), and Poisson's ratio (ν). These moduli decrease approximately linearly with Li concentration. This weakening tendency is likely due to the replacement of Sn-Sn bonds by the weaker Li-Sn and Li-Li bonds [53], but further studies need be carried out.

Table 2.2 - Room temperature above values for bulk modulus (K), Young's modulus (E), shear modulus (G), and Poisson's ratio (ν). All moduli values are in GPa.

Phase	K_H	E_H	G_H	ν_H	Ref.
β-Sn	50.04-61.11	39.98-52.22	14.63-21.11	0.344-0.367	[53,54,64]
Li$_2$Sn$_5$	40.96-45.26	36.86-74.81	13.51-30.74	0.221-0.364	[53,54,64]
LiSn	32.55-37.81	47.40-51.09	18.14-20.04	0.270-0.280	[53,54,64]

---

[1] In the case of polycrystalline materials, the bulk modulus (K), Young's modulus (E), shear modulus (G), and Poisson's ratio (ν) may be calculated from independent monocrystalline elastic constants. The Voigt-Reuss-Hill approximations, also referred as Hill values, consider the arithmetic average of Voigt and Reuss values to be the best estimate of the theoretical polycrystalline elastic moduli [158].

Table 2.2 – Continued.

Phase	K_H	E_H	G_H	ν_H	Ref.
Li_7Sn_3	19.53-33.02	54.41-60.93	25.18-26.30	0.172-0.205	[53,54,64]
Li_5Sn_2	12.19-32.24	43.12-67.58	18.13-29.36	0.145-0.189	[53,54,64]
$Li_{13}Sn_5$	28.89-36.16	48.740-68.85	24.40-29.63	0.125-0.205	[53,54,64]
Li_7Sn_2	15.90-30.35	24.71-61.57	9.97-26.50	0.160-0.239	[53,54,64]
$Li_{17}Sn_4$	26.30-35.16	48.89-54.77	20.74-22.08	0.190-0.240	[53,64]
(Li)	11.99-15.15	15.28-20.07	5.56-8.22	0.218-0.332	[53,54,64]

2.3.3. Li-Sn alloys production and characterization

The different production and characterization techniques regarding Li-Sn alloys are compiled in Table 2.3. Amongst the different processes, melting has been the dominant technique [3–11]. However, obtaining a homogeneous liquid phase is a challenging task as Li tends to segregate to the surface of the molten phase, promoting the formation of Li-rich compounds with high melting points [9,10]. Several solutions to the problem have been proposed, strong stirring being a key component. Natesan *et al.* [10] developed a fabrication method, in which liquid Li is gradually added to a Sn molten bath, with simultaneous continuous stirring, to ensure a slowly increase of the Li content. However, to obtain a fully homogeneous alloy, stirring for 3 days was needed. Similarly, production of the intermetallic compounds for thermodynamic investigations by melting required time-consuming post-annealing treatments, which can involve periods of up to 60 days [44]. Nakajima *et al.* [9] obtained the best results when an initial random layout of the Li and Sn granules was used in the crucible, and a vertical stirring motion was applied.

Mechano-synthesis of Sn powders with Li cuts from ribbons has been suggested as a promising alternative method to produce these alloys [13,14], but the process and relevant parameters remain relatively understudied. In the next section (section 2.4. Mechano-synthesis of metallic powders (MS)), an overview of the working principles of mechano-synthesis of metallic powders is provided, followed by an analysis of the main results for the Li-Sn alloys.

Table 2.3 - Overview of the production techniques and characterization studies of Li-Sn alloys.

Nominal composition (at. %)	Production Technique	Heat Treatment	Characterization Studies	Phase Analysis	Ref.
90Li-10Sn	Melting route: Heating at 200 ºC for 60 days	None	XRD, DSC	$Li_{17}Sn_4$; Li	[44]
81.5Li-18.5Sn	Melting route: Heating at 400 ºC for 40 days	None	XRD, DSC	$Li_{17}Sn_4$; Sn	[44]
81Li-19Sn	Melting route: Heating at 400 ºC for 14 days	None	XRD, DSC	$Li_{17}Sn_4$; Li_7Sn_2	[44]
80.95Li-19.05Sn ($Li_{17}Sn_4$)	Melting route: Heating 30 ºC above the appropriate melting point for 3-5 h	None	XRD, ICP-OES, DSC	$Li_{17}Sn_4$	[4]
	Melting route: Sequence of heating cycles at different T for 2 weeks	None	XRD, ICP-OES, DSC	$Li_{17}Sn_4$	[5]

Table 2.3 – Continued.

Nominal composition (at. %)	Production Technique	Heat Treatment	Characterization Studies	Phase Analysis	Ref.
80.95Li-19.05Sn ($Li_{17}Sn_4$)	Mechanical alloying route: planetary ball mill, 5 h milling time, 510 rpm, 10 mm milling balls	None	XRD, SEM	$Li_{22}Sn_5$	[73]
	Mechanical alloying route: vibratory mill, 20 Hz, BPR 50:1, 48 h milling time	Annealing at 150ºC for 7 days	XRD, Mossbauer spectroscopy	$Li_{22}Sn_5$	[74]
	Mechanical alloying route: vibratory mill, 2 milling balls, 48 h milling time	Annealing (no information on T and duration)	XRD, Mossbauer spectroscopy	$Li_{22}Sn_5$	[75]
80Li-20Sn	Melting route: Heating at 400 ºC for 4 days	None	XRD, DSC	$Li_{17}Sn_4$; Li_7Sn_2; Sn	[44]
79Li-21Sn	Melting route: Heating at 400 ºC for 4 days	None	XRD, DSC	$Li_{17}Sn_4$; Li_7Sn_2	[44]
78Li-22Sn (Li_7Sn_2)	Melting route: Heating 30 ºC above the appropriate melting point for 3-5 h	None	XRD, ICP-OES, DSC	Li_7Sn_2	[4]
	Melting route: Heating at 600 ºC (no information on duration)	Annealing at the same T for 30h	XRD, Mossbauer spectroscopy	Li_7Sn_2; ($Li_{13}Sn_5$)	[6]
	Mechanical alloying route: vibratory mill, 20 Hz, BPR 50:1, 48 h milling time	Annealing at 600 ºC for 7 days	XRD, Mossbauer spectroscopy	Li_7Sn_2	[74]
	Mechanical alloying route: vibratory mill, 2 milling balls, 48 h milling time	Annealing (no information on T and duration)	XRD, Mossbauer spectroscopy	Li_7Sn_2	[75]
76Li-24Sn	Melting route: Heating at 450 ºC for 21 days	None	XRD, DSC	Li_7Sn_2; $Li_{13}Sn_5$	[44]
74Li-26Sn	Melting route: Heating at 400 ºC for 42 days	None	XRD, DSC	Li_7Sn_2; $Li_{13}Sn_5$	[44]
73.3Li-26.7Sn ($Li_{13}Sn_5$)	Mechanical alloying route 1 h	12-13 h thermal treatment 30 ºC below the peritectic temperature	XRD, ICP-OES, DSC	$Li_{13}Sn_5$	[4]
	Melting route: Heating at 550 ºC (no information on duration)	Annealing at the same T for 24 h	XRD, Mossbauer spectroscopy	$Li_{13}Sn_5$	[6]
	Mechanical alloying route: vibratory mill, 20 Hz, BPR 50:1, 48 h milling time	Annealing at 400 ºC for 7 days	XRD, Mossbauer spectroscopy	$Li_{13}Sn_5$; Sn	[74]
	Mechanical alloying route: vibratory mill, 2 milling balls, 48 h milling time	Annealing (no information on T and duration)	XRD, Mossbauer spectroscopy	$Li_{13}Sn_5$	[75]
72.9Li-27.1Sn (Li_5Sn_2)	Mechanical alloying route 1 h	12-13 h Thermal Treatment 30 ºC below the peritectic temperature	XRD, ICP-OES, DSC	Li_5Sn_2	[4]
	Melting route: Heating at 550 ºC (no information on duration)	Annealing at the same T for 48 h	XRD, Mossbauer spectroscopy	Li_5Sn_2; (Li_7Sn_3)	[6]
	Mechanical alloying route: vibratory mill, 20 Hz, BPR 50:1, 48 h milling time	Annealing at 420 ºC for 7 days	XRD, Mossbauer spectroscopy	Li_5Sn_2; Sn; (Li_7Sn_3)	[74]
	Mechanical alloying route: vibratory mill, 2 milling balls, 48 h milling time	Annealing (no information on T and duration)	XRD, Mossbauer spectroscopy	Li_5Sn_2	[75]
72.2Li-27.9Sn	Melting route: Heating at 400 ºC for 42 days	None	XRD, DSC	$Li_{13}Sn_5$; Sn	[44]
71Li-29Sn	Melting route: Heating at 450 ºC for 21 days	None	XRD, DSC	Li_7Sn_3; Li_5Sn_2; Sn; LiSn	[44]

Table 2.3 – Continued.

Nominal composition (at. %)	Production Technique	Heat Treatment	Characterization Studies	Phase Analysis	Ref.
70Li-30Sn (Li_7Sn_3)	Melting route 2 weeks	None	XRD, ICP-OES, DSC	Li_7Sn_3	[7]
	Melting route: Heating at 510 ºC (no information on duration)	Annealing at 400 ºC for 4 h	XRD, Mossbauer spectroscopy	Li_7Sn_3; ($LiSn$)	[6]
	Mechanical alloying route: vibratory mill, 20 Hz, BPR 50:1, 48h milling time	Annealing at 400 ºC for 7 days	XRD, Mossbauer spectroscopy	Li_7Sn_3; Sn; (Li_5Sn_2)	[74]
	Mechanical alloying route: vibratory mill, 2 milling balls, 48 h milling time	Annealing (no information on T and duration)	XRD, Mossbauer spectroscopy	Li_5Sn_2	[75]
60Li-40Sn	Melting route: Heating at 300 ºC for 21 days	None	XRD, DSC	LiSn; Li_7Sn_3; Sn	[44]
50Li-50Sn (LiSn)	Melting route: Heating at 300 ºC for 21 days	None	XRD, DSC	LiSn; Li_2Sn_5; Sn	[44]
	Melting route: Heating at 510 ºC (no information on duration)	Annealing at 435 ºC for 2 h	XRD, Mossbauer spectroscopy	LiSn; (Li_2Sn_5)	[6]
	Mechanical alloying route: vibratory mill, 20 Hz, BPR 50:1, 48 h milling time	Annealing at 250 ºC for 7 days	XRD, Mossbauer spectroscopy	LiSn	[74]
	Mechanical alloying route: vibratory mill, 2 milling balls, 48 h milling time	Annealing (no information on T and duration)	XRD, Mossbauer spectroscopy	LiSn	[75]
	Mechanical alloying route: planetary ball mill, 500 rpm, BPR 10:1, 10 mm milling balls, milling time 8 h	None	XRD, SEM, RBS + NRA	Sn	[13]
	Mechanical alloying route: planetary ball mill, 500 rpm, BPR 10:1, 10 mm milling balls, milling time 8 h	Annealing at 160 ºC for 2 h	XRD	Sn; Li_2Sn_5; LiSn	[13]
40Li-60Sn	Melting route: Heating at 573K for 14 days	None	XRD, DSC	Li_2Sn_5; LiSn; Sn	[44]
30Li-70Sn	Melting route: at the Nuclear Radiations Laboratory at the U. Illinois Urbana	None	---	---	[8]
	Melting route: Heating at 350ºC for 10min	None	ICP-AES	---	[9]
28.6Li-71.4Sn (Li_2Sn_5)	Melting route: Heating at 425ºC (no information on duration)	Annealing at 300 ºC for 24 h	XRD, Mossbauer spectroscopy	Li_2Sn_5	[6]
	Mechanical alloying route: vibratory mill, 20 Hz, BPR 50:1, 48 h milling time	Annealing at 150 ºC for 7 days	XRD, Mossbauer spectroscopy	Li_2Sn_5; Sn	[74]
	Mechanical alloying route: vibratory mill, 2 milling balls, 48 h milling time	Annealing (no information on T and duration)	XRD, Mossbauer spectroscopy	Li_2Sn_5	[75]
25Li-75Sn	Melting route: Sequence of heat cycles at different T with a total duration of 4 days	None	XRD, SEM, Vickers hardness measurements	Sn; eutectic Sn and Li_2Sn_5	[10]
	Mechanical alloying route: planetary ball mill, 150 rpm, BPR 10:1, 6 mm milling balls, milling time 12 h	None	XRD, SEM, RBS + NRA	Sn; Li_2Sn_5; LiSn	[14]
	Mechanical alloying route: planetary ball mill, 150 rpm, BPR 10:1, 6 mm milling balls, milling time 12 h	Annealing at 160 ºC for 2 h	XRD	Sn; Li_2Sn_5; LiSn	[14]
	Melting route: Heating at 350 ºC for 10 min	None	ICP-AES	---	[9]

Table 2.3 – Continued.

Nominal composition (at. %)	Production Technique	Heat Treatment	Characterization Studies	Phase Analysis	Ref.
20Li-80Sn	Melting route: commercially available (Princeton Sci. Corp., Easton, PA, USA)	None	---	---	[11]
	Melting route: Heating at 350 ºC for 10 min	None	ICP-AES	---	[9]
15Li-85Sn	Mechanical alloying route: planetary ball mill, 150 rpm, BPR 10:1, 6 mm milling balls, milling time 12 h	None	SEM, RBS + NRA	---	[14]
5Li-95Sn	Mechanical alloying route: planetary ball mill, 150 rpm, BPR 10:1, 6 mm milling balls, milling time 12 h	None	SEM, RBS + NRA	---	[14]

Characterization Studies: XRD – X-ray diffraction, ICP-OES - Inductively coupled plasma optical emission spectroscopy, ICP-AES – Inductively coupled plasma atomic emission spectroscopy, DSC – Differential scanning calorimetry, SEM – Scanning Electron Microscopy, RBS - Rutherford backscattering spectrometry, NRA - Nuclear reaction analysis.

2.4. Mechano-synthesis of metallic powders (MS)

Mechano-synthesis (MS) is a process in which chemical reactions between mixtures of powders are induced by mechanical action [76,77]. In the study field of mechano-synthesis of metallic powders, depending on whether or not material transfer is involved, two different terms are used to describe powder mechanical processing [78]: Mechanical Alloying (MA) which denotes the milling of powder mixtures where material transfer takes places between powders, and Mechanical Milling (MM) in which average particle size reduction is the sole goal. In the present work, MA is the milling process used, via high-energy ball milling, so the remainder of this subsection will focus on it. It is important to note that MA, a MS process method, is often used as a generic milling term, also referring to reaction milling (RM) [78,79].

MA was developed in the 1960s for the production of oxide dispersion strengthen (ODS) alloys [78]. During MA, metallic particles suffer strong plastic deformation with subsequent work-hardening. As milling progresses, the particles are continually compacted, fractured and cold-welded [76]. Through high-energy ball milling, it is possible to synthesize both equilibrium and non-equilibrium (metastable) phases, such as supersaturated solid solutions, amorphous alloys, and high entropy alloys [76,80,81]. As a result of MA capability to produce phases with outstanding properties, it has been widely explored for the production of novel materials, such as high-temperature superconductors, metallic glasses, nanostructured materials, nanocomposites, and superhard carbo-nitrides [82]. When compared to other non-equilibrium processing methods, such as rapid solidification, irradiation/ion implantation, and condensation from vapor phase, MA has the advantage of being a less expensive, simple and versatile process [76].

2.4.1. Milling parameters

Important components of the MA process are the starting raw powders, the milling system, and the processing variables. The upper limit for the input milling particle size is defined by the milling ball diameter: the particle size should be smaller than the milling ball diameter [76].

There are different types of high energy milling equipment (e.g., planetary ball mills, attrition mills, SPEX shaker mills, vibratory mills, etc.). In the present work, a planetary ball mill is used. Figure 2.2 illustrates its working principle. A planetary ball mill combines two different types of motion: the rotation of the disc supporting the grinding vial, known as sun disc, and the rotation of the vial around its own axis in the opposite direction. Milling rate always refers to the sun disc angular velocity and is expressed in rotations per minute (rpm).

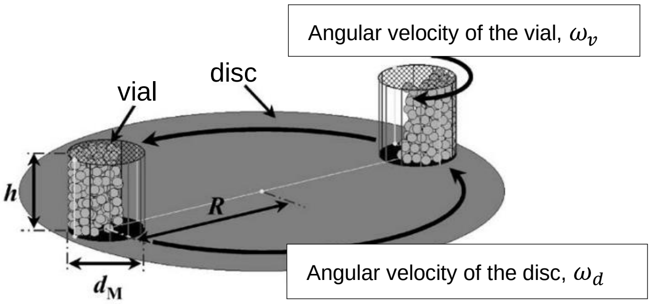

Figure 2.2 - Schematic diagram of a planetary ball mill, adapted from [83].

Several parameters can have a pronounced effect on the final product, including [84–86]:

- (i) geometrical parameters - milling container dimensions, distance between rotational axis, and ratio between the angular velocity of the sun disc and the angular velocity of the vial;
- (ii) processing parameters - milling rate; milling time; material, size, and size distribution of the milling medium; ball-to-powder weight ratio (BPR); volume filling ratio of the vial; milling atmosphere, and temperature.

For a large number of milling balls, Burmeister *et al.* [85] identified three milling regimes (Figure 2.3) as a function of the milling parameters:

1. cascading regime, in which friction between milling balls is dominant. In this regime, the balls are taken along the vial walls and unroll upon each other from the bulk top to its base;
2. cataracting regime, in which the balls detach from the wall and impact other balls or the opposite wall. This is an impact predominant regime;
3. rolling regime, in which the balls move together with the vial with almost no relative velocity. Friction between milling media is dominant.

The balls motion evolves from cascading to cataracting and up to the rolling regime with increasing filling ratio and/or increasing milling rate [87–91].

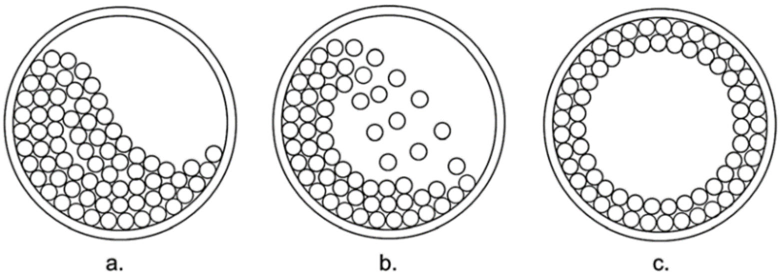

Figure 2.3 - Schematics of ball motion pattern in a planetary ball mill vial – (a) cascading, (b) cataracting, (c) rolling, [85].

The microstructure of the final powder particles is affected by the milling regime [92]. The ball movement influences the number of collisions, the ball velocity, and, consequently, the ball impact force, which contributes to the energy transmitted to the powders. The main events to consider are the ball-ball and ball-wall collisions, and friction between the milling media [93]. As a rule of thumb, 50% of the vial space should be left empty so that the milling balls and powder particles can move freely inside the vial and generate impacts on the particles [76]. For small capacity mills, a BPR of 10:1 is the most often used [76].

The mechanisms involved in MA in a planetary ball mill are complex and dependent on both the powders properties and milling parameters. Hence, the optimum milling parameters must be assessed for each individual system, according to the intended experimental aims.

2.4.2. Alloying Mechanisms

During MA of metal based powder batches, two competing mechanisms are considered to occur: fracture and cold-welding [76]. Cold-welding results in particle size growth, whereas fracture in its reduction. Most metallic powders, and especially pure metals powders, are generally considered capable of plastic deformation. For most cases, particles are expected to either flatten or fracture. Steady-state equilibrium is said to be achieved when there is a balance between the cold-welding rate and the fracture rate [76]. Once such state is achieved, the particle size does not change significantly. The conditions of such equilibrium limit the achievable minimum particle size.

In the review work of Suryanarayana [76], the author divides the expected mixing behaviour of the powders according to the properties of the raw material. He considers three main regimes: ductile-ductile, brittle-ductile, and brittle-brittle. The alloying mechanisms suggested by Suryanarayana are summarized on Table 2.4. However, due to the complexity of the process involved, and the amount of effects which may occur, there is no consensus on a complete description of the effects induced by MA when different powders are mixed [93]. The next subsection (subsection 2.4.2.1. Mechano-synthesis modelling) delves into the topic of MS modelling and the efforts being made to better understand the influence of the different milling parameters on the alloying mechanisms and milling powder final output properties.

Table 2.4 - Three main regimes of powders mixing behaviour, proposed by Suryanarayana [76].

Pure metals and/or alloys combination	**Alloying Mechanism**	
	Initial stage	**Increasing milling time**
Ductile-ductile	Flattening and simultaneous cold-welding of the ductile particles, resulting in the formation of a composite lamellar structure accompanied by particle size growth.	Fragmentation of composite particles due to their work-hardening and reduction of particle size. Convolution of the lamellar structure and refinement of the interlamellar spacing, reducing the diffusion distances, and promoting the formation of solid solutions, and/or intermetallics.
Brittle-ductile	Flattening of ductile particles and fragmentation of brittles particles. Inclusion of the fragmented brittle components in the ductile particles.	Work-hardening of the ductile components, particle fragmentation, and reduction of particle size. If brittle component is not soluble in the ductile matrix, a dispersion of brittle particles is obtained. If it is soluble, alloying occurs with formation of solid solutions, and/or intermetallics.
Brittle-brittle	Fragmentation of the powder particles and reduction of their size.	Structure refinement in the nanometre range.

2.4.2.1. Mechano-synthesis modelling

MS is a complex stochastic process with a dynamic behaviour involving a multitude of physical phenomena, which occur at different length scales. The problem is complicated even when simplification is attempted due to considerable amount of both independent and dependent variables that can affect the final output. Though understanding all processes involved in MS can prove to be a dauting task, great effort has been put into modelling them as to predict the outcomes of the process for a particular set of conditions. An effective model would, in principle, be able to predict the optimum process parameters for a desired aim without the need for long, time-consuming experiments.

There are two possible approaches to MS modelling analytical or numerical. Some studies have attempted to analytically model the ball motion and its mechanical action depending on the operating parameters of a planetary ball mill. Some of the most widely used models include those developed in the nineteen's (1990-1996) by Courtney *et al.* [94–97], Gaffet *et al.* [98,99], Iasonna *et al.* [100–102], and Watanabe *et al.* [103]. In these initial models, the balls velocity and trajectory in the vial are described by kinematic equations, and impact events between balls and vial walls are expected to be the governing energy transfer events. To the extent of the author's knowledge, no recent studies have been published by these groups.

Although analytical models are simple and, to some extent, informative, they have limitations due to their simplifying assumptions (e.g., perfect inelastic collisions, "no-slip" and "no-friction" conditions). In-situ observations [90,92] revealed that there are different ball movement regimes depending on the predominant interaction events (ball-ball, ball-powder, and ball-vial interactions). On the other hand, numerical multibody models, despite requiring more computational power, are able to more accurately account for the complexity of the milling process and deliver more accurate predictions. Some recent works on modelling of mechanical milling [84,88,104–107] have used the Discrete Element Method (DEM) to perform 3D numerical simulations, reproduce the complex ball motion pattern and quantify the effects of BPR, variable sizes and numbers of particles and balls, rotational speed of the vial, and vial geometry on energy dissipation. The cataracting regime has been identified as the most efficient for energy dissipation. So far, however, brittle powders (silica glass [104], alumina [84], calcium fluoride [106], etc.) have been the main subject of study, as they correspond to less complicated mechanical systems to be modelled, when compared to ductile powders. Thus, expanding the scope of DEM to simulate the mechano-synthesis of ductile powders would the next step.

At the atomic level, some studies have used Molecular Dynamics (MD) simulations to better understand the mechanisms that occur during mechanical alloying of binary mixtures [93,108–113]. All studies identified the intimate coupling between mechanical properties, crystallographic structure, interface coherence, and chemical mixing at the atomic scale, being specific for each binary system. Among the systems studies are Cu-Ag [109–111], Fe-Cu [109,110], Ni-Al [93], Ti-Al [93], Fe-Ni [93], and Fe-Cr [93].

Although analytical modelling techniques, in particular DEM and MD, still need be refined, their joint use with experimental analysis is a powerful tool to gain further knowledge on the complex mechano-synthesis process.

2.4.3. Mechano-synthesis of Li-Sn alloys

Intermetallic phases synthesized by MS include both equilibrium and metastable phases [76]. In some cases, synthesis of equilibrium crystalline phases was observed following MS; in others, formation of target intermetallics may require additional heat treatment following MS.

In the case of (Li) and β-Sn, which have low melting points, it should be noted that room temperature milling corresponds to a significantly high homologous temperature. Thus, these metals possess a tendency for welding during milling, which, despite being denominated cold-welding (due to the term being commonly used in the literature for welding in a mill at room temperature), may correspond to a considerably hot mechanism for these metals. Nevertheless, for the remainder of the present work, the welding phenomenon that takes place during milling/mechanical alloying is referred to as cold-welding for consistence with literature.

The first studies reporting the use of mechano-synthesis to produce Li-Sn intermetallics were carried out in the field of Li-ion batteries. They mainly focused on the characterization of the electrochemical properties of Li-rich intermetallics [73–75], and heat capacity calculations for improving the thermodynamic description of the Li-Sn system in the Li-rich part of the phase diagram [7]. Two studies reported mechano-synthesis of LiSn and Li_2Sn_5 using a vibratory mill, for 48 h of milling time, with subsequent 7 day annealing treatment [74,75]. Comprehensive phase characterization of the MS output, however, was not carried out and no description of the mechano-synthesis process, nor of the alloying mechanisms was presented.

Recently, Li-Sn alloys, in particular with low Li content (< 25 at. %), have received considerable attention for application in plasma facing components of nuclear fusion reactors [12–16]. Costa *et al.*

[14] reported the successful production of Li-Sn alloys with Li compositions in the 5-25 Li (at. %) interval through mechano-synthesis. Formation of both equilibrium and out of equilibrium crystalline intermetallics was observed. 25Li-Sn (at. %) alloy milled for 12 h presented β-Sn, Li_2Sn_5 and LiSn. Post-annealing at 160º for 2 h promoted growth of the stable Li_2Sn_5 intermetallic, with a correspondent partial decrease of the fraction of LiSn.

Nevertheless, the predominant cold-welding behaviour of these alloys when mechanically milled results in low milling mass yields (< 20 % [16]). The higher the β-Sn content, the lower the milling mass yield. Moreover, due to the low density of Li compared to Sn, preparation of alloys with Li content below 5 at. %, is difficult. Mateus *et al.* [13] developed a lithium dilution method for the production of Li-Sn alloys with Li content below 5 at. %. They prepared a 50 Li-Sn (at. %) master powder alloy and then achieved the desired 5Li-Sn (at. %) and 1Li-Sn (at. %) alloys by dilution of the master powders with the correspondent amounts of pure Sn. Although compositional analysis confirmed that the desired Li:Sn stoichiometry was attained, phase characterization of the master alloy revealed the presence of β-Sn, Li_2Sn_5, and LiSn, even after annealing treatment at 160 ºC for 2 h. Therefore, improvement of the mechano-synthesis process and respective phase analysis is still necessary and a comprehensive study of the reaction path and influence of the milling parameters on the final microstructure and composition of Li-Sn alloys is lacking.

Chapter 3. Experimental techniques and procedures

The present chapter provides an in-depth overview of the methodology adopted to endow the developed work with reproducibility and transparency. Information regarding the materials, production procedures and characterization techniques employed is presented. Section 3.1. Materials resumes information relative to the raw materials used to produce the studied equimolar Li-Sn (50:50 at. %) alloy. Section 3.2. Procedure for equimolar Li-Sn alloy production provides a description and explanation of the experimental mechano-synthesis route and parameters used to synthesise the alloy. 3.3. Equimolar Li-Sn alloy characterization contains information on the sample characterization techniques used: IBA (Ion Beam Analysis); XRD (X-Ray Diffraction); DSC (Differential Scanning Calorimetry), and GA (Thermogravimetric Analysis). Subsections 3.3.1. to 3.3.5. briefly describe the fundamental working principles of each technique and explain the reason for its employment and chosen parameters.

3.1. Materials

In this section, a description of the starting materials is provided based on the supplier product information. As starting materials, air atomised Tin powders and cuts of Lithium ribbons were used.

3.1.1. Tin powder

Tin powders (purity 99.9 wt. %, < 45 μm) were kindly supplied by Makin Metal Powders Ltd. They were produced from high purity refined Tin. Table 3.1 presents the supplier powder size distribution information.

Table 3.1 - Powder size distribution of as-supplied Sn.

Granulometry		
Mesh Size (B.S.S.)	**μm**	**Result (wt.%)**
200	>75	0.0
300	>53	0.1
-350	<45	99.9

3.1.2. Lithium ribbons

Lithium ribbons (purity 99.9 at. %) were supplied by Sigma-Aldrich. All as-supplied Li ribbons presented black stains along their surface, which indicates that, most likely, they reacted with moisture leading to the formation of LiOH (dark cusp) during production or handling, which resulted in a native surface film.

3.2. Procedure for equimolar Li-Sn alloy production

This section details the experimental mechano-synthesis route used to produce the equimolar Li-Sn alloy, guaranteeing the reproducibility of the powder samples prepared. For the remainder of the present work, for simplicity, the equimolar Li-Sn alloy will be referred to as 50Li-Sn.

3.2.1. Mechano-synthesis: equipment and process parameters

A PM100 Retsch planetary ball mill was used to produce the equimolar Li-Sn alloy, having a ratio between the rotational speed of the sun disc and the rotational speed of the vial of 1:2. Both milling vial (50 mL) and balls used are made from quenched and tempered 420C AISI Steel to minimize the sources of powder contamination. Milling balls with rugosity grade G10 were selected.

The mass of the powder milling batch was set to 3 g, meaning 2.834 g of Sn and 0.166 g of Li, according to the weight ratio Li:Sn of 50Sn-Li alloy (1:17). As a result, to have a BPR of 10:1, 34 spheres of 6 mm, 7 spheres of 10 mm, and 2 spheres of 15 mm were used.

The method for preparation of the initial powder milling batch and placement inside the vial required special care as to prevent mass loss to the milling media during milling. A piece of Li was cut from a ribbon and its surface was lightly sanded with SiC grinding paper to remove the surface native film. Then, it was cut into square pieces with approximately 2 mm, using a sharp stainless-steel blade. First, Sn powder was added into the vial, then the cut Li pieces were added and covered with Sn powder to ensure there were no fresh cut Li surfaces that could stick with other Li surfaces or the vial walls. Once a homogenized mixture was obtained, the milling balls were added.

Also, to prevent powder contamination from atmospheric gases, starting and processed materials storage, vial loading, sealing, opening, and sample handling was carried out under argon atmosphere (< 0.1 ppm H_2O/O_2), inside a glovebox (MBraun Unilab Plus). To seal the vial atmosphere during milling, a security hatch was used. Samples were carried to the characterization facilities inside small HDPE flasks sealed with an O-ring.

Milling experiments were designed to maintain reproducible constant conditions inside the vial, while minimising experiment time. Weight-normalized cumulative energy transferred from the balls to the powders depends on the powder weight [94,100,102,114,115]. Thus, as a rule, for each time condition studied, a full continuous milling run was carried out and samples for characterization were collected at the end of the run. With this procedure, the powder batch mass is kept constant throughout the milling run.

Two milling rates (150 rpm and 500 rpm), three milling ball diameters (6 mm, 10 mm, and 15 mm), and milling times from 0.5 h to 64 h were tested to produce the equimolar alloy. The milling parameters tested, and respective acronyms are summarized in Table 3.2, making up a total of 21 powder batches and continuous milling experiments. All continuous milling cycles were carried out with 10 min uninterrupted milling followed by a 5 min stopping interval to allow the milling media and milled batch to cool, avoiding overheating. The effective milling time refers to the sum of the total uninterrupted milling periods. When referring to a particular effective milling time, for a certain milling condition, the effective milling time is added to the milling condition base acronym, e.g.: 500rpm-10mm-8h, meaning 500 rpm, 10 mm diameter milling balls and 8 h effective milling time.

Table 3.2 - Experimental milling conditions and respective milling parameters.

Milling condition base acronym	**Milling rate (rpm)**	**Milling ball diameter (mm)**	**BPR (wt/wt)**	**Uninterrupted milling time (min)**	**Stopping time (min)**	**Effective milling times (h)**
150rpm-6mm-t	150	6	10:1	10	5	0.5, 2 and 8
150rpm-10mm-t		10				
150rpm-15mm-t		15				
500rpm-6mm-t	500	6				
500rpm-10mm-t		10				0.5, 2, 8, 16, 32 and 64
500rpm-15mm-t		15				0.5, 2 and 8

To characterize the mass output of the milling process, y_M, the overall mass yield, is defined as the ratio of the mass of the loose powder collected at the end of the milling cycle, M_{end}^{Pw}, to the initial mass of the powder batch, M_{init}^{Pw}:

$$y_M = \frac{M_{end}^{Pw}}{M_{init}^{Pw}} \text{ x } 100 \qquad \text{(Equation 3. 1)}$$

Besides y_M, the mass fraction loss due to the mass gain of the milling balls, F_M^B, and the mass fraction loss due to vial mass gain, F_M^{VW}, are also defined as the ratio of the respective mass gain (balls or vial) to the initial mass of the powder batch, M_{init}^{Pw}, so that:

$$y_M + F_M^B + F_M^{VW} = 1 \qquad \text{(Equation 3. 2)}$$

The initial mass of the powder batch, M_{init}^{Pw}, is known for all milling experiments. After milling, powder was brushed from the walls and balls, and weighted. Material that had sticked to the walls and balls, and was not removed easily by the brush, was not considered as powder output.

For certain time conditions, the mechano-synthesis product was composed by both powder and disc-like particles. The disc-like particles were considered for milling mass yield calculations but were separated from the powders for characterization (using a sieve inside the glovebox), as it was suspected that they derived from the initial Li pieces. As will be observed in the next chapter, subsection 4.4.5.2. XRD results and discussion, XRD measurements on the disc-like particles confirmed that their phase composition was composed of (Li) and Li-rich Li-Sn intermetallics. As such, DSC measurements (subsection 3.3.3. Differential scanning calorimetry (DSC)) were only performed on powders, without the disc-like particles, due to the high risk of Li reaction with the sample holder for temperatures above Li melting point.

3.2.2. Cold-pressing

Cold pressing was used to produce powder pellets for IBA and XRD measurements. Since the pressing machine was to be used inside the glovebox, systems with common lubricants could not be employed. As such, a manual pressing machine was modified to a screw press. Figure 3.1 displays the set-up used to measure the maximum force developed by the press when operated by the author. The press could develop a maximum force of around 5.7 kN, delivering a maximum compressive stress of ~ 90 MPa for the Ø9 mm pellets produced.

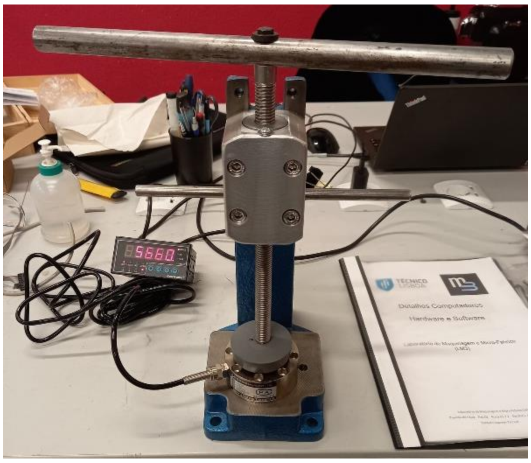

Figure 3.1 - Set-up for the measurement of the maximum force developed by the press.

Figure 3.2 shows the full set-up used to produce the powder pellets: the modified press, Ø9 mm die tool, base plate, and punch. The die was made of cold working tool steel. For all samples prepared by this method, powder was measured so that pellets of approximately Ø9 x 2 mm were produced. As an example, the pellets produced for IBA analysis are presented in Figure 3.3.

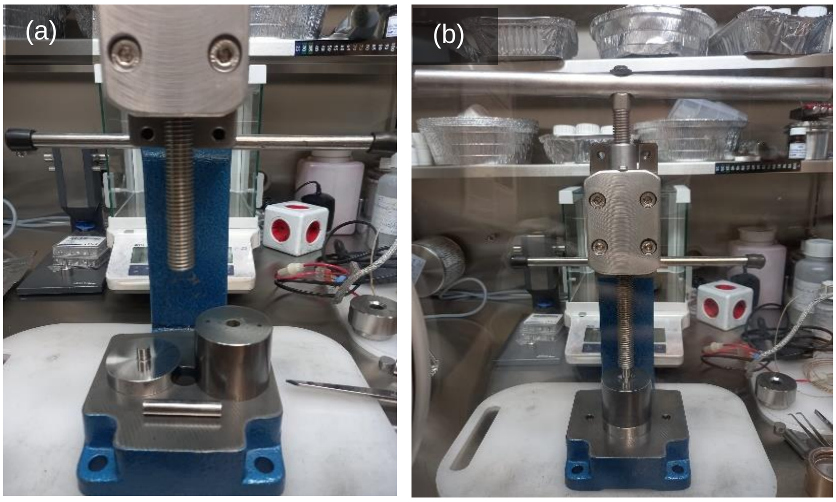

Figure 3.2 - (a) on the back, from left to right: base plate and die. On the front: punch. (b) full set-up for powder pellet preparation.

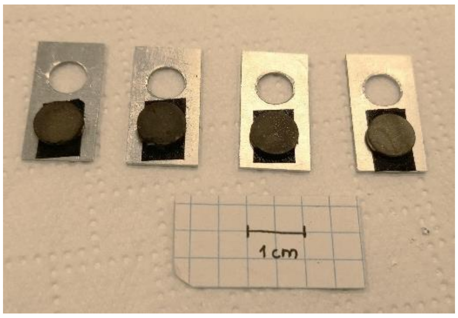

Figure 3.3 - Pellets prepared mounted on IBA sample holders.

3.3. Equimolar Li-Sn alloy characterization

Samples from the milling experiments were collected, prepared, and analysed to evaluate chemical composition and phases present. IBA supplied qualitative and quantitative chemical composition characterization, particularly about Li and possible contaminant contents; XRD was used for phase identification and quantitative phase analysis; DSC was carried out to access phase transitions and transformations, and GA provided information on sample mass variation when exposed to air atmosphere, at NTP conditions.

3.3.1. Ion beam analysis (IBA)

Ion Beam Analysis (IBA) refers to the group of surface characterization techniques which make use of the fundamental physics of the interactions between incident ion beams and target atoms present in the sample's surface to infer about the material elemental composition and elemental depth profile. An ion beam of a known element, usually Hydrogen (H^+) or Helium (He^+) ions, impinges the atoms and nuclei in the sample's surface. As a result of these interactions, different products (particles and photons) are emitted from the sample: secondary electrons, γ-rays, X-rays, recoils, scattered ions, and nuclear reaction products [116]. Elements in the target are identified by measuring the energies of the emitted products, and modelling, assuming known or calculated cross-sections of the events, allows the quantification of individual elemental contents [117]. The collection of all the individual products in the spectra holds information on elemental composition. For complementary elemental analysis or for unambiguous results to be obtained, different techniques are often employed simultaneously. One of the most widespread combinations, already referred to as Total-IBA, consists of Rutherford Backscattering Spectrometry (RBS), Nuclear Reaction Analysis (NRA), and Particle Induced X-ray Emission (PIXE) [118]. Part of the incident ions impinge atoms at the sample surface. The remaining ion beam will interact with target nuclei and electrons as ions penetrate along the sample depth, losing energy. In RBS and NRA spectra, the energy loss is easily visualised by detecting particles at lower energies, enabling to quantify elemental depth profiles [119,120].

In RBS, the energy of the ions which are elastically backscattered from nuclei of sample atoms is measured. The energy with which the ions arrive at the detector is affected by the involved Rutherford backscattering cross-section, detection geometry, mass of both incident ion and target nucleus and by the depth at which the scattering event occurs. In general, RBS provides 10-30 nm of in-depth resolution [119]. The maximum depth range for the incident ions depends on the elements present in the sample as well as on the ion beam energy, while the energy loss is typically lower for lighter atoms and decreases at higher incident energies. Regarding detection limits, heavier elements may have lower concentration detection limit than lighter ones (few ppm for heavy elements vs. few percent for light ones) [119]. Lower detection limits are achieved when the superposition of elemental yields is avoided. The sensitivity of RBS analysis enhances at specific resonant backscattering yields when incident proton beams impinging light elements are used (p-RBS) [121]. Nevertheless, incident ions are backscattered by lighter elements with lower energies [119,120]. For thick sample analysis, the elemental yields become commonly superimposed and typically, RBS lacks sensitivity for light element detection.

NRA measures the energy of the products of nuclear reactions occurring between impinged ions and target nuclei: emitting γ-rays, nucleons (neutrons and protons), and groups of nucleons (deuterons, α-particles, etc.) [120]. Analysis of the collected energies provides information on the specific target nucleus, through induced nuclear reactions identification, and on the depth at which the reaction event took place. Similar to RBS, NRA in-depth resolution depends on the particular reaction and sample matrix, ranging from a few nanometres to several tens of nanometres [120]. Detected energies in NRA spectra typically depend on the same factors applied to RBS, but also on the amount of energy absorbed or released by the nuclear reaction (Q value of the reaction), and generally, advantage of the involved cross-sections and resonant energies is taken [120].

With ion beam energies generated by most common IBA facilities, resonant energies enhancing nuclear reaction yields for heavier elements are difficult to achieve, and therefore, no signal is produced from heavy elements by NRA [120,122]. What differentiates NRA from RBS is its sensitivity towards light element detection, when the NRA cross-sections are high enough to extremely enhance the elemental yield in the spectra. A second example that really improves light element detection by NRA is the case of specific nuclear reactions inducing the emission of high energetic particles, avoiding the superposition of both RBS and NRA yields in the particle spectra [120].

In the case of parallel detection, particle yields of RBS and NRA are usually presented together, being referred to as RBS-NRA spectra.

In the present work, the in-depth quantification of Li on a Li-Sn matrix was carried out with RBS-NRA spectra involving the ^{7}Li(p,α)^{4}He nuclear reaction. 2.0 MeV H^+ incident ion beams were used. In this reaction, a ^{7}Li nucleus reacts with an incident proton, generating two ^{4}He particles. Each event releases an energy of 17.35 MeV (the Q value of the nuclear reaction) [12,120]. For the detection geometry in use, the ^{4}He particle is detected with 7.9 MeV, and the superposition between the NRA yield and the RBS one, induced by heavy Sn, is largely avoided. Incident protons also lose energy inside the Li-Sn matrix, enabling to evaluate the depth profile of Li by NRA yield down to a depth range close to 20 μm.

PIXE records the products of another event: when ions collide with target atoms, ejection of the inner-shell electrons occurs; as electronic deexcitation occurs, X-rays photons are emitted which are characteristic of the respective element, being the cross-sections dependent on the incident ion (H^+ or He^+) and energy beam [123]. In the present analysis, Sn contents were quantified from the Sn-K_α X-ray emission. If superposition of X-rays peaks is not observed, the sensitivity of PIXE for element detection may lie in the range 1-10 µg/g [123]. Therefore, the technique is useful to identify minor contaminants in the samples.

All experiments were carried out in the 2.5 MeV Van de Graaff accelerator of CTN/IST. Total-IBA analysis was carried out on 4 pellet samples: 500rpm-10mm-0.5h, 500rpm-10mm-2h, 500rpm-10mm-8h, and 500rpm-10mm-16h. A nuclear microprobe, with an image pixel size of 3 x 3 μm^2, was used to scan 512 x 512 μm^2 areas, each sample being scanned twice. In total, 256 x 256 µ-RBS-NRA and µ-PIXE individual spectra were collected simultaneously, and elemental maps for Li, Sn, and contaminants were carried out to evaluate the pellet elemental homogeneity. For this purpose, two depth energy ranges in the µ-RBS-NRA were selected from Li-NRA yields to evaluate the spread of Li in Sn nearby the superficial layers and at deeper depths. Sn maps were also selected from an energy range in the Sn-RBS yield nearby the superficial layers. Additionally, mapping of Sn and minor contaminants was carried out by selecting peak areas in the µ-PIXE spectra corresponding to the Sn-K_α, Cr- K_α, Fe- K_α, Cu-K_α, and Pb-K_α X-ray emissions, as Cr, Fe, Cu, and Pb were identified as minor contaminants. µ-NRA provides the main information about Li-Sn alloy stoichiometry and Li in-depth content. Both features were evaluated from the sum of all spectra. Quantitative analysis was carried out using DataFurnace software [124]. Elemental quantification by PIXE was done with GUPIXWIN software [125]. As the particle detector was not polarized during analysis of samples from milling experiments run for 0.5 h, 2 h, and 8 h, Li-Sn alloy elemental and stoichiometry quantification could only be carried out for sample from the milling experiment run for 16 h.

3.3.2. X-Ray diffraction (XRD)

As previously referred, XRD was used for phase identification and quantitative phase analysis. Acquisition of good quality XRD data presented several challenges due to the intrinsic properties of the alloy under study and the underlying fundamental principles of the X-ray diffraction characterization technique. In this work, a diffractometer with no atmosphere controlled stage was used. Therefore, Li high chemical reactivity when exposed to atmospheric air during XRD analysis needed to be mitigated. Furthermore, Li has a very low scattering factor, due to its low atomic number, which means that the diffracted intensity of the phases with Li atoms in their crystal structure is much lower. This effect is even worse when phases have low phase fractions, which revealed to be the present case. This meant that the XRD test parameters needed to be selected as to result in diffractograms with high signal to background ratios. For the abovementioned reasons, selection of the best XRD test parameters was required as to obtain a balance between high signal to background ratios and short run duration to prevent sample degradation. A preliminary XRD Context Study was conducted in which the effectiveness of liquid paraffin as a protective degradation coating and the feasibility of using XRD to characterize the produced 50Li-Sn powders was assessed. This subsection has the following subdivision: subsection 3.3.2.1. XRD Theory summarizes the relevant fundamental working principles; subsection 3.3.2.2. XRD Diffractometer and Test Parameters presents the different parameters used for data collection; 3.3.2.3. Sample Preparation describes the employed sample preparation methods; subsection 3.3.2.4. XRD Context Study: 50Li-Sn alloy chemical reactivity in air environment provides the methodology adopted for the preliminary study, and subsection 3.3.2.5 XRD data analysis and graphing explains in detail the methods used for phase identification and quantitative phase analysis assessment.

3.3.2.1. XRD Theory

XRD techniques are based on coherent X-ray scattering: an X-ray beam, when incident upon a sample, induces the coherent oscillation of the electrons of the atoms in the crystal structure, resulting in the emission of coherent X-rays in all directions [126]. A detector captures the sum of all diffracted X-rays, producing a diffractogram. For the X-rays to be detected, the interference between the diffracted X-rays needs to be constructive. For a 3D crystal, diffraction from a certain set of *(h k l)* planes occurs depending on two conditions, regarding [126]: 1. the incoming beam orientation with respect to the plane, and 2. the position of the atoms within the unit cell with respect to the plane. *Bragg equation* (Equation 3. 3) is the mathematical representation of the necessary first condition:

$$2d\ sin\theta = n\lambda \qquad \text{(Equation 3. 3)}$$

Bragg equation states that both the X-ray wavelength λ and the interplanar spacing *d* determine the diffracted beam angle θ (Bragg angle) at which constructive interference from a set of consecutive parallel planes can occur. The integer number *n* defines the order of the diffraction process. However, this equation only states the geometrical constraints which must be satisfied. The scattering of X-rays from a crystal must also consider the relative position of all scattering atoms in the unit cell. The *structure factor* (F_{hkl}) is the quantity that describes this scattering. Its square modulus is proportional to the intensity of the diffracted beam from the *(hkl)* planes:

$$F_{hkl} = \sum_{j=1}^{N} f_j\ e^{2\pi i(hx_j+ky_j+lz_j)} \qquad \text{(Equation 3. 4)}$$

$$I_{hkl} = |F_{hkl}|^2 \qquad \text{(Equation 3. 5)}$$

where *N* is the number of atoms in the unit cell. Even if the Bragg condition is satisfied for a particular plane, there will be no diffracted beam if the structure factor is zero. (Equation 3. 4) and (Equation 3. 5), show that the intensity of the diffracted beam depends on the position of the atoms in the atomic planes (x_j, y_j, z_j) and the elemental nature of the atoms (f_j, the scattering factor which quantifies the contribution of an atom to the diffraction from the plane *(hkl)*). In the case of the of alloys of the Li-Sn system, as aforementioned, the Li atom contribution to the intensity of the diffracted beam is small due to its low scattering factor (low atomic number, Z=3).

3.3.2.2. XRD Diffractometer and Test Parameters

The diffractometer used in this work was a Bruker D8 ADVANCE Powder Diffractometer using Cu-K_α radiation (electric potential difference of 40 kV, and electric current of 30 mA). Its features and specifications are presented in Table 3.3. A zero-signal sample holder, made from a silicon wafer, was used for all tests.

Table 3.3 - Summary of instrument conditions for data collection.

Instrument	**Bruker D8 ADVANCE**
Incident radiation	Cu K_α
Tube electric potential difference (kV)	40
Tube electric current (mA)	30
Instrument radius (mm)	217.5
Divergence slits (º)	0.34
Soller slits (º)	2.5
Diffracted beam filter	Ni
Detector type	Bruker LynxEye SSD160

To mitigate the problem of low peak intensity associated with phases containing Li, selection of the most suitable XRD test parameters to obtain high signal to background ratio was required. The signal to background ratio is mainly controlled by the acquisition time, among other factors. As will be discussed in subsection 4.3.1. XRD context study: 50Li-Sn alloy chemical reactivity in air environment, liquid paraffin only provides partial degradation protection. As such, a balance had to be found between the duration of the XRD run and the signal to background ratio. The selected test parameters and respective test acronyms (2θ interval (º): step size (º): step acquisition time (s)) are presented in Table 3.4. For later Rietveld refinements, an XRD measurement of SRM 660c (Standard Reference Material LaB_6) [127] was carried out for calibration of diffraction line positions and line shapes. The XRD test parameters used for this measurement are also presented in Table 3.4.

Table 3.4 - XRD test parameters used throughout the present work.

XRD Test acronym	**2θ interval (º)**	**Step size (º)**	**Step acquisition time (s)**	**Collection time (h: min: s)**	**Use**
15-55: 0.05: 0.5	15-55	0.05	0.5	00: 07: 00	Some samples XRD Context Study
15-55: 0.04: 0.8	15-55	0.04	0.8	00: 14: 39	All other samples
15-80: 0.005: 1.0	15-80	0.005	1.0	03: 36: 39	SRM 660c

3.3.2.3. Sample Preparation

As previously referred, for certain milling time conditions, both powders and disc-like particles composed the mechano-synthesis product. Powders, as well as disc-like particles, were characterized using XRD.

To minimize *h* displacement error inhomogeneity related to sample surface rugosity, two powder sample preparation methods were used, depending on the powder particle size after milling, assessed by visual inspection: powder film sample (particle size < 1 mm) or powder pellet sample (particle size > 1 mm). For film samples, powders were, as a rule, dispersed in liquid paraffin. Pellets, produced as previously described (subsection 3.2.2. Cold-pressing), were used directly for pellet samples and coated with liquid paraffin. The two sample preparation methods were performed inside the glovebox. Either powders, disc-like particles, or pellets were put inside a small flask, two to three drops of liquid paraffin were added and then the flask was closed, sealed with an O-ring. Disc-like particles were treated as powders samples.

Pw (for powder sample), Pl (for pellet sample), and D (for Discs) are the acronyms used for each sample condition. These can be added to the milling condition base acronym for clarification.

3.3.2.4. XRD Context Study: 50Li-Sn alloy chemical reactivity in air environment

The diffractometer used in this work does not possess an available controlled atmosphere stage, neither a portable sample holder could be developed within the framework of this work. So, Li high chemical reactivity, when exposed to atmospheric air, during XRD sample preparation and analysis, needed to be mitigated. Liquid paraffin was considered as a possible surface diffusion barrier as it is inert regarding Li and Li alloys [128]. Also, its non-volatility allowed for its safe handling inside the glovebox.

So, the suitability of liquid paraffin to act as protective coating was investigated. Liquid paraffin, supplied by José Manuel Gomes dos Santos, LDA., was selected for this purpose. Tests were carried out on 500rpm-10mm-8h milled samples because this milling experiment presented the highest milling mass yield (report to section 4.1. Milling mass yield evolution with time). The set of XRD tests carried out are summarized in Table 3.5.

Table 3.5 - Samples and test conditions used in the XRD Context Study.

Test	**XRD Sample Condition**	**Prior XRD Analysis air exposure duration (h: min: s)**	**XRD test conditions**	**XRD Runs**
1	Uncoated film	04: 18: 00	15-55:0.04:0.8	1
2	Coated film	04: 18: 00		1
3	Uncoated film	00: 01: 57		5
4	Coated film	00: 02: 40		5

3.3.2.5 XRD data analysis and graphing

In this subsection, a detailed description of the methods used for phase identification and quantitative phase analysis assessment is provided.

Phase identification and graphing

For phase identification, the Search-Match functionality of Profex software [129] was used. The experimental data was matched to those present in the Crystallographic Open Database (COD). Crystallographic Information Files (CIF) were imported to Profex, which contain information regarding the space group, the lattice parameters, unit cell atoms, and their respective spatial positions and Wyckoff positions. The CIFs used in the present work, together with their crystallographic information and reference are presented in Table 3.6.

For graphing, a baseline was fitted to the background and subtracted, and intensities were normalized as a 100% percentage of intensity of the most intense peak (100%).

Table 3.6 - Crystallographic Information Files imported to Profex software for phase identification.

Formula	**COD ID**	**Space Group**	**Cell Parameters**						**Cell Volume (Å^3)**	**Ref.**
			a (Å)	**b (Å)**	**c (Å)**	**α (º)**	**β (º)**	**γ (º)**		
β-Sn	9008570	$I4_1/amd$	5.8197	5.8197	3.17488	90	90	90	107.53	[60]
(Li)	9008542	Im3m	3.5093	3.5093	3.5093	90	90	90	43.218	[60]
Li_2Sn_5	2106975	P4/mbm	10.274	10.274	3.12500	90	90	90	329.86	[65]
LiSn	7221163	P2/m	5.17	3.18	7.74	90	104.5	90	123.197	[66]
Li_7Sn_3	7221164	$P2_1/m$	8.56	4.72	9.45	90	105.95	90	367.111	[67]
Li_5Sn_2	7221114	R-3m	4.74	4.74	19.83	90	90	120	385.842	[68]
$Li_{13}Sn_5$	7221116	P-3m1	4.7	4.7	17.12	90	90	120	327.514	[69]
Li_7Sn_2	7221115	Cmmm	9.8	13.8	4.75	90	90	90	642.39	[70]
$Li_{17}Sn_4$	4313755	F-43m	19.6907	19.6907	19.6907	90	90	90	7634.6	[37]
SnO	9008956	P4/nmm	3.802	3.802	4.836	90	90	90	69.905	[60]
SnO_2	9009082	$P4_2/mnm$	4.73727	4.73727	3.186383	90	90	90	71.508	[60]
Li_2O	9009059	Fm-3m	4.619	4.619	4.619	90	90	90	98.547	[60]
Li_3N	1544904	P6/mmm	3.652	3.652	3.866	90	90	120	44.65	[130]
LiH	9008668	Fm-3m	4.0271	4.0271	4.0271	90	90	90	65.31	[60]
HLiO	9008958	P4/nmm	3.546	3.546	4.334	90	90	90	54.496	[60]
Li_2C_2	1521871	Immm	3.652	4.8312	5.4344	90	90	90	95.882	[131]
Li_2C_2	1521872	Fm-3m	5.965	5.965	5.965	90	90	90	212.242	[131]
H_3LiO_2	1010456	C2/m	7.37	8.26	3.19	90	110.3	90	182.1	[132]
Li_2CO_3	2310703	C12/c1	8.39	5.00	6.21	90	114.5	90	237.054	[133]
$LiNO_3$	1011340	R-3c	5.74	5.74	5.74	48.05	48.05	48.05	95.8	[134]
LiN_3O_4	4117032	$I4_1/a:2$	5.9164	5.9164	19.712	90	90	90	689.99	[135]

COD - Crystallographic Open Database.

Rietveld Refinement

The Rietveld method is a whole-pattern-fitting method of structure refining in which an iterative least-squares refinement is conducted until the best fit is achieved between all points in the observed powder diffractogram and all points in the calculated diffractogram [136]. This method assumes that intensity is a single discrete function that can be fitted by a multi-parameter model [126]. The calculated pattern is based on models for background intensity, peak shape (location, intensity, FWHM and tails), crystal structures (lattice parameters, atoms positions and occupations in the unit cell), diffraction optics effects, instrumental factors, and other specimen characteristics (e.g., Debye-Waller factors) [136].

The Rietveld method is a very powerful tool since it allows the extraction of a lot of information from the powder diffractogram: estimate of lattice parameters; quantitative analysis of both crystalline and amorphous phases; estimate of crystallite size and of residual strain. In the present work, Rietveld Refinement of a total of 10 diffractograms was conducted for quantitative phase analysis of diffractograms from tests 3 and 4 of the XRD Context Study. The Rietveld method was not used for quantitative phase assessment of powder phase evolution with milling time of the main study because it requires that all phases contributing to the diffractogram are known, which, as will be discussed in subsection 4.4.5.2. XRD results and discussion, proved to be difficult. Moreover, lattice parameters determination was not carried out using Rietveld Refinement as accurate results require data collection over higher 2θ angles (> 110 º) [137].

The refinements were conducted in the open-source GSAS-II software [138]. The order of parameter refinement was chosen such that the parameter having the highest impact, on the difference between observed and calculated points, was first refined [139]. Prior to Rietveld Refinement, determination of approximate instrument profile parameters was carried out by peak fitting of the diffractogram collected from standard SRM 660c [140]. The values calculated were stored in a .instprm file, which, together with the CIF files (Table 3.6) from the phases of interest, were imported to define starting parameter values of the quantitative phase analysis model. The sequence in which parameters were added, refined, or fixed is detailed in Table 3.7.

Table 3.7 - Sequence of parameter addition and refinement in the quantitative phase analysis model.

Refinement step	Parameters refined
1	only Q^{-2} power series background
2	only sample displacement
4	only Li_2Sn_5 unit-cell parameters
5	only LiSn unit-cell parameters
6	only Sn unit-cell parameters
7	Li_2Sn_5, LiSn and Sn unit-cell parameters
8	Refining (7) + Li_2Sn_5, LiSn and Sn scale factor
9	Refining (8) + Li_2Sn_5, LiSn and Sn domain size
10	Refining (8) + Li_2Sn_5, LiSn and Sn microstrain
11	Refining (8) + Li_2Sn_5, LiSn and Sn domain size

Among the eight background functions available in GSAS-II, Q^{-2} power series was selected. It should be noted that proper background fitting was the main challenge encountered when preforming Rietveld Refinement due to high scattering on the low-angle range. A beam knife edge would reduce the scattering in this angle region [141].

There are a series of agreement indexes which can be computed to provide information on the "goodness of the fit". In the present work, the weighted profile R-factor (R_{wp}) was considered [136]:

$$R_{wp} = \sqrt{\frac{\sum_i w_i\ (y_i(obs) - y_i(calc))^2}{\sum_i w_i\ (y_i(calc))^2}} \qquad \text{(Equation 3. 6)}$$

In which $y_i(obs)$ are the observed intensity values and *i* indicates that the intensity was measured at 2θ value $2θ_i$; $y_i(calc)$ are the intensity values simulated from the model, and w_i are the weights for each intensity value at 2θ value $2θ_i$. In GSAS-II environment, the weights are defined as [142]:

$$w_i = \frac{1}{\sigma_i^2} \qquad \text{(Equation 3. 7)}$$

Where σ_i is the standard uncertainty of the experimental intensity measured at each 2θ value $2θ_i$, which is given by [142,143]:

$$\sigma_i^2 = y_i(obs) \qquad \text{(Equation 3. 8)}$$

It should be noted that this figure of merit is only an attempt to establish a criterion for evaluating the quality of a Rietveld model and allowing its comparison with other models. Visual inspection of the fits, identifying systematic discrepancies in the residuals, combined with continuous judgement of the physical and chemical plausibility of the model is the best method to ascertain the quality of a Rietveld fit [143]. As such, the experimental XRD diffractograms and their respective simulated fits are presented in Appendix B.

Simulation of XRD diffractograms

Besides providing an environment for Rietveld Refinement of diffraction data, GSAS-II also allows the simulation of diffraction patterns. For the simulated patterns to be considered as quantitative models of the experimental observations, an accurate instrument description must be provided [144]. Thus, the file .instprm created for Rietveld Refinement, from the XRD measurement of the standard SRM 660c, was also used for the simulations. The refinable parameters, in the context of Rietveld Refinement, are also used as input parameters in the context of powder pattern simulations. In GSAS-II environment, the following expression is used for total powder diffraction profile intensity calculation [142]:

$$I = I_b + S \sum_p S_p\ Y_{ph} \qquad \text{(Equation 3. 9)}$$

Where I_b is the background intensity, S is the histogram scale factor, S_p is the individual phase scale factor, and Y_{ph} is the contribution from the h^{th} reflection of the p^{th} phase (Bragg intensity). Among the eight background functions available in GSAS-II, chebyschev-1 was selected.

The two scale factors play an important role for multiphase mixtures analysis. The histogram scale factor, S, is a scalar that equally scales all reflections' intensity allowing to control the counting rate (counts per second, c.p.s.), thus is the analogue of the experimental parameter acquisition time. As information regarding the phases sensitivity and detection limit was of interest, it was crucial to set S such that the counting rate matched the experimental counting rate. In X-ray diffraction, the sensitivity of a phase, S_i, is defined as the rate of change in net signal output, I_i (c.p.s.), with respect to concentration X_i (%), and is given by the ratio I_i/X_i [145]. S_i is related with the detection limit of the phase i, $X_i\ (d.l)$, through the expression [145]:

$$X_i\ (d.l) = \frac{3}{S_i}\sqrt{\frac{I_b}{t}} \qquad \text{(Equation 3. 10)}$$

Where I_b is the background counting rate (c.p.s.), and t is the background counting time (s). Considering the above, the histogram scale factor was set to 1.

The individual phase scale factor is used for quantitative phase analysis as it allows the determination of the phase weight fraction through the following expression [142]:

$$W_p = \frac{S_p\, m_p}{\sum_{p=1}^{Np} S_p\, m_p} \qquad \text{(Equation 3. 11)}$$

Where m_p is the unit cell mass of phase p. So, to simulate mixtures of phases with a certain phase weight fraction, the respective phase scale factor must first be calculated. The Bragg intensity is given by [142]:

$$Y_{ph} = F_{ph}^2\, H(2\theta - 2\theta_{ph})\, K_{ph} \qquad \text{(Equation 3. 12)}$$

Where F_{ph} is the structure factor, $H(2\theta - 2\theta_{ph})$ is the value of the profile peak shape function for the reflection at a position 2θ displaced from its expected $2\theta_{ph}$ position, and K_{ph} is the product of the intensity correction factors [142]:

$$K_{ph} = \frac{E_{ph}\, A_h\, O_{ph}\, M_p\, L}{V_p} \qquad \text{(Equation 3. 13)}$$

Where E_{ph} is the extinction correction, A_h is the absorption correction, O_{ph} is the preferred orientation correction, M_p is the reflection multiplicity, L is the angle dependent correction (Lorentz-polarization), and V_p is the unit cell volume of the phase. The CIF data (Table 3.6) was used to set the phase structural parameters (unit cell and atom parameters).

The primary interest of the simulation series was to understand the influence of phase weight fraction and crystallite size on peak profile. It rose from the necessity to acquire knowledge regarding the diffractograms of Li-rich Li-Sn intermetallics to overcome the problems encountered in phase identification, which are discussed in depth in subsection 4.4.5.2. XRD results and discussion. Phase scale factor and crystallite mean size were the two parameters operated. For each of the five Li-rich Li-Sn intermetallics, seven simulations were carried out for variable phase weight percentages and crystallite mean sizes. Table 3.8 compiles the information of all simulation conditions carried out. For each simulation, the acronym adopted was Awt.%-Bnm (A – phase weight percentage value, and B – crystallite mean size value). The calculated phase scale factors are not presented because their relationship with phase weight fractions is software dependent [146]. The reason for the choice of the values of phase weight fraction and crystallite mean size is detailed in subsection 4.4.5.2. XRD results and discussion. The 50Li-Sn mass stoichiometry was not respected as material losses during milling and Li oxidation during XRD analysis may occur, and a broader knowledge of the system was meant.

Table 3.8 - Weight fraction (wt.%) and crystallite mean size (nm) values considered in each simulation model and respective simulation acronym.

Simulation Acronym	**Li-rich intermetallic under study**	**Input parameters defined**															
		Weight Fraction (wt.%)								**Crystallite Mean Size (nm)**							
		β-Sn	**Li_2Sn_5**	**LiSn**	**Li_7Sn_3**	**Li_5Sn_2**	**$Li_{13}Sn_5$**	**Li_7Sn_2**	**$Li_{17}Sn_4$**	**β-Sn**	**Li_2Sn_5**	**LiSn**	**Li_7Sn_3**	**Li_5Sn_2**	**$Li_{13}Sn_5$**	**Li_7Sn_2**	**$Li_{17}Sn_4$**
40wt.%-50nm	Li_7Sn_3	20	25	15	40	---	---	---	---	0.5	0.05	0.05	0.05	---	---	---	---
	Li_5Sn_2				---	40	---	---	---				---	0.05	---	---	---
	$Li_{13}Sn_5$				---	---	40	---	---				---	---	0.05	---	---
	Li_7Sn_2				---	---	---	40	---				---	---	---	0.05	---
	$Li_{17}Sn_4$				---	---	---	---	40				---	---	---	---	0.05
60wt.%-5nm	Li_7Sn_3	17.5	15	7.5	60	---	---	---	---	0.5	0.05	0.05	0.005	---	---	---	---
	Li_5Sn_2				---	60	---	---	---				---	0.005	---	---	---
	$Li_{13}Sn_5$				---	---	60	---	---				---	---	0.005	---	---
	Li_7Sn_2				---	---	---	60	---				---	---	---	0.005	---
	$Li_{17}Sn_4$				---	---	---	---	60				---	---	---	---	0.005
50wt.%-5nm	Li_7Sn_3	20	20	10	50	---	---	---	---	0.5	0.05	0.05	0.005	---	---	---	---
	Li_5Sn_2				---	50	---	---	---				---	0.005	---	---	---
	$Li_{13}Sn_5$				---	---	50	---	---				---	---	0.005	---	---
	Li_7Sn_2				---	---	---	50	---				---	---	---	0.005	---
	$Li_{17}Sn_4$				---	---	---	---	50				---	---	---	---	0.005
40wt.%-5nm	Li_7Sn_3	20	25	15	40	---	---	---	---	0.5	0.05	0.05	0.005	---	---	---	---
	Li_5Sn_2				---	40	---	---	---				---	0.005	---	---	---
	$Li_{13}Sn_5$				---	---	40	---	---				---	---	0.005	---	---
	Li_7Sn_2				---	---	---	40	---				---	---	---	0.005	---
	$Li_{17}Sn_4$				---	---	---	---	40				---	---	---	---	0.005
30wt.%-5nm	Li_7Sn_3	20	30	20	30	---	---	---	---	0.5	0.05	0.05	0.005	---	---	---	---
	Li_5Sn_2				---	30	---	---	---				---	0.005	---	---	---
	$Li_{13}Sn_5$				---	---	30	---	---				---	---	0.005	---	---
	Li_7Sn_2				---	---	---	30	---				---	---	---	0.005	---
	$Li_{17}Sn_4$				---	---	---	---	30				---	---	---	---	0.005
20wt.%-5nm	Li_7Sn_3	25	32.5	22.5	20	---	---	---	---	0.5	0.05	0.05	0.005	---	---	---	---
	Li_5Sn_2				---	20	---	---	---				---	0.005	---	---	---
	$Li_{13}Sn_5$				---	---	20	---	---				---	---	0.005	---	---
	Li_7Sn_2				---	---	---	20	---				---	---	---	0.005	---
	$Li_{17}Sn_4$				---	---	---	---	20				---	---	---	---	0.005
15wt.%-5nm	Li_7Sn_3	30	32.5	22.5	15	---	---	---	---	0.5	0.05	0.05	0.005	---	---	---	---
	Li_5Sn_2				---	15	---	---	---				---	0.005	---	---	---
	$Li_{13}Sn_5$				---	---	15	---	---				---	---	0.005	---	---
	Li_7Sn_2				---	---	---	15	---				---	---	---	0.005	---
	$Li_{17}Sn_4$				---	---	---	---	15				---	---	---	---	0.005

3.3.3. Differential scanning calorimetry (DSC)

Differential Scanning Calorimetry (DSC) is a thermal characterization technique used for quantitative and qualitative phase transformation analysis.

In a differential scanning calorimeter, the sample (a few mg of material), and the reference (usually an empty sample holder) undergo the same thermal cycle (commonly linear temperature ramps or isothermal holds), and the heat flow difference necessary to maintain at the same temperature, both the sample and the reference, is measured. Heat flow differences are due to physical transformations, such as a phase transition or a chemical reaction, and an amount of heat will need to flow in (for endothermic events), or out (for exothermic events). Valuable information about the analysed samples is supplied by the identification of the starting temperature and of the amount of heat flow difference during exothermic and endothermic events.

In this work, DSC 200 F3 Maia, from NETZSCH Premier Technologies, was used. N_2 was the chosen purge gas (50mL/min purge flow). Tzero Hermetic TA Aluminium sample holders and 5-7 mg samples were used in all tests. To prevent sample degradation, the sample holders were sealed inside the glovebox.

The thermal cycle used for DSC analysis is presented in Table 3.9. Segments 3 and 4 were carried out to access if reactions observed in segments 1 and 2 were either reversible or irreversible within the thermal interval used. Ideally, the maximum temperature of the heating ramp segment would have been 500 ºC, which would allow to detect the congruent fusion of LiSn at 485 ºC, the eutectic reaction LiSn + Li_7Sn_3 ⇌ Liquid (469 ºC), and the peritectic reaction LiSn + Liquid ⇌ Li_2Sn_5 (325 ºC) [59], and thus to identify the presence of Li_7Sn_3, LiSn and Li_2Sn_5. However, the high Li content of the formed liquid could induce a strong reaction and perforation of the aluminium sample holder. Also, strong gravity segregation of Li to the surface of the molten phase would induce the formation of Li-rich Li-Sn intermetallics, with higher melting points, up to 783 ºC, and misleading results [9,10]. As such, 250 ºC, above the Li_2Sn_5 + β-Sn ⇌ Liquid (222 ºC) eutectic [59], and of pure (Li) (180.6 ºC) and β-Sn (232.0 ºC) melting points, was set as the maximum temperature. In total, 11 samples were analysed: all 500rpm-10mm-t milled samples (0.5 h, 2 h, 8 h, 16 h, 32 h, and 64 h), and all 8h milling conditions (150rpm-6mm, 150rpm-10mm, 150rpm-15mm, 500rpm-6mm, and 500rpm-15mm).

Table 3.9 - Thermal cycle used for DSC analysis.

Segment	Description
1	Heating Ramp 10ºC/min to 250ºC
2	Cooling Ramp 10ºC/min to 150ºC
3	Heating Ramp 10ºC/min to 250ºC
4	Cooling Ramp 10ºC/min to 150ºC

3.3.4. Gravimetric analysis (GA)

Gravimetric analysis (GA) is an analytical technique in which the mass of a sample is measured during a selected time cycle, in a controlled atmosphere. The sample mass change is measured in a thermobalance, which is composed by an electronic microbalance, a furnace and temperature control system. This technique is commonly used to study materials mass gain/loss associated with oxidation, decomposition, dehydration, and loss of volatiles [147].

GA analysis aimed to confirm the formation of Li-air reaction products when 50Li-Sn alloy is exposed to air, at NTP conditions, as well as the suitability of liquid paraffin as a protective coating.

GA analysis was carried out in Setsys Evo 16 equipment, from Setaram, under air atmosphere. A gas flow of 30 mL/min was used. Each test had a duration of 3 h, and the sample temperature was kept constant at 22 ºC. A total of 3 tests were conducted under this time-temperature program: (1) baseline (empty sample holder); (2) 40 mg of powder without liquid paraffin, and (3) 40 mg of powder with 50 mg of liquid paraffin.

Chapter 4. Results and Discussion

In this chapter, results regarding the mechano-synthesis experiments and characterization of 50Li-Sn alloys and the related degradation phenomena are presented and discussed. Section 4.1. Milling mass yield evolution with time addresses the mass yield of the milling experiments. Section 4.2. 50Li-Sn powder composition analysis presents and discusses the composition analysis of the produced alloys by IBA in order to access the final Li content of the mechano-synthetised 50Li-Sn alloys. Section 4.3. 50Li-Sn powder phase evolution and degradation is dedicated to the structural and phase analysis of the milled products (DSC and XRD) as well as to the degradation phenomena that affects this study.

4.1. Milling mass yield evolution with time

As previously referred (subsection 2.4.3. Mechano-synthesis of Li-Sn alloys), when milling ductile powders with low melting points, milling can occur at high homologous temperature, T_M^*, leading to enhanced dynamic and static recovery and recrystallization, so that cold welding of the powders prevails over strain hardening and facture. Particularly in an oxygen free environment, extensive plastic deformation leads to the development of a pristine metal surface prone to adhesion and cold welding between themselves and to the milling media. This induces a detrimental reduced mass yield of the milling process, y_M (defined as the ratio of the mass of the loose powder collected at the end of the milling cycle, to the initial mass of the powder batch), which tends to intensify for longer milling times [76].

In this subsection, the dependence of y_M on milling parameters is discussed. Besides y_M, the mass fraction loss due to milling balls' mass gain, F_M^B, and the mass fraction loss due to vial mass gain, F_M^{VW}, are also defined as the ratio of the respective mass gain (balls or vial) to the initial mass of the powder batch, such that:

$$y_M + F_M^B + F_M^{VW} = 1 \qquad \text{(Equation 4. 1)}$$

However, as previously mentioned in subsection 2.4.2.1. Mechano-synthesis modelling, it should be noted that mechano-synthesis is a complex stochastic process and that only one milling experiment for each milling time was carried out. As such, caution must be taken when drawing conclusions.

Figure 4.1 shows that, overall, the milling efficiency of 50Sn-Li alloy is considerable larger than of Li-Sn alloys with Li content below 25 at.%, for which milling mass yields below 20 % [16] have been reported. Except for milling experiments 500rpm-6mm, all the remaining milling experiments present milling mass yields above 40 %, more than double.

The observed difference in milling efficiency is due to the difference in powder phase composition and in the mechanical properties of each phase. When milling ductile powders with low melting points, milling can occur at high homologous temperature, T_M^*. In the case of (Li) and β-Sn, assuming a conservative milling temperature of 30 ºC, $T^*_{(Li)} = 0.67$ and $T^*_{\beta-Sn} = 0.60$, which indicates a hot-working environment, instead of cold-working. For β-Sn, dynamic recrystallization is known to occur when strained [24,27,28] and static recovery is known to occur when the stress is removed [22], hindering work-hardening. For (Li), to the best of the author's knowledge, there is no information on the predominant process of stored deformation energy release. Extensive plastic deformation takes place and cold-welding of the deformed powders prevails over fracture, leading to extensive adhesion and cold-welding of the deformed powders to the milling media surfaces. This induces a reduced mass yield of the milling process, which tends to intensify for longer milling times [76]. For Li-Sn alloys with Li content below 25 at.%, β-Sn phase was identified as the major constituent, being responsible for the predominant adhesion and cold-welding behaviour of the powders, which resulted in low y_M [16]. On the other hand, as will be observed in section 4.3. 50Li-Sn powder phase evolution and degradation, for 50Li-Sn alloy, milled powders possess a base LiSn composition, plus Li_2Sn_5, or even Li-rich Li-Sn intermetallics. These are not as ductile as the pure metals, and their homologous temperature (considering their decomposition temperature) is lower, respectively, $T^*_{LiSn} = 0.40$, $T^*_{Li2Sn5} = 0.51$, and as low as ~ 0.30 for some Li-rich Li-Sn intermetallics. Their formation accounted for the reversal of the predominant adhesion and cold-welding behaviour of the powder batches, with strain hardening and fracture competing against cold-welding.

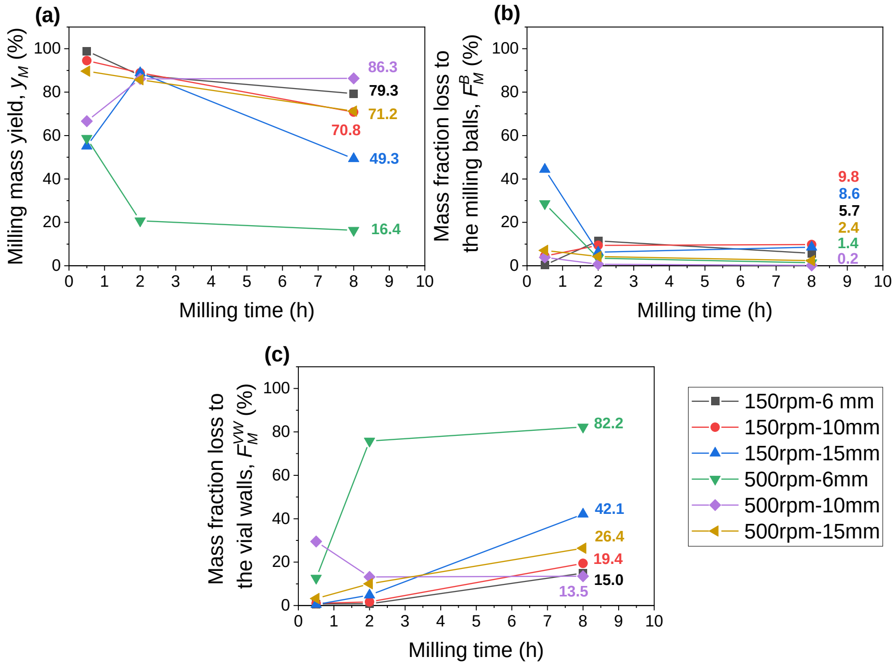

Figure 4.1. - Milling mass yield evolution with milling time: (a) milling mass yield, y_M, (b) mass fraction loss to the milling balls, F^B_{mass}, and (c) mass fraction loss to the vial walls, F^{VW}_{mass}.

Nevertheless, as Figure 4.1 illustrates, there is still a general loss of process efficiency due to material adhesion and cold-welding to the milling media, as milling time progresses. Particularly for milling time above 2 h, the main source of material loss is powder adhesion and cold-welding to the vial walls, F^{VW}_M, with a general increasing tendency with milling time. On the other hand, adhesion, and cold-welding to the milling balls, F^B_M, randomly oscillates, being responsible for less than 10% of the total mass loss.

It is difficult to infer, however, about the influence of milling parameters on the magnitude of the increasing tendency of material loss due to powder adhesion and cold-welding to the vial walls as the differences observed among the majority of the different milling conditions lie within the standard deviation associated with the stochastic nature of mechano-synthesis. Milling experiments 150rpm-15mm and 500rpm-6mm are the ones experiencing the most severe mass loss to the milling media, as illustrated in Figure 4.2. Although special care was taken in the preparation of the initial powders batch inside the vial, if by some random event, in the early stages of milling, a considerable amount of (Li) pieces or β-Sn powders adhere to the milling media, those surface areas will act as preferable locations for cold-welding of the milling powders as milling progresses, affecting milling efficiency. For each milling time, more milling experiments should be carried out for the results to present a higher confidence level.

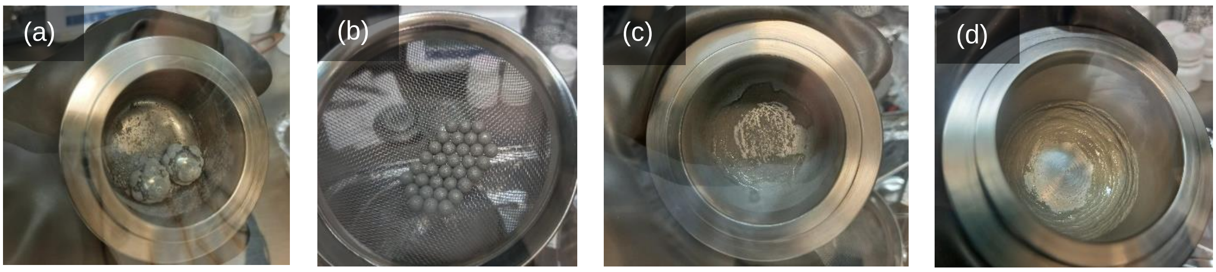

Figure 4.2 - Adhesion and cold-welding to the milling media: (a) 150rpm-15mm-0.5h sample, (b) 500rpm-6mm-0.5h sample, (c) 150rm-15mm-8h sample, and (d) 500rpm-6mm-8h sample.

Milling experiments 500rpm-10mm produce the most promising results as the mass loss increasing tendency seems to have been countered. An almost stationary $y_M \sim 86\%$ is reached after 2 h. To confirm if a steady state is indeed achieved, additional milling experiments were carried out for 16 h, 32 h, and 64 h. Figure 4.3 comprises the respective y_M, F_M^{VW}, and F_M^{B} evolution with milling time. Results show that, for milling experiments 500rpm-10mm, a quasi-steady state is achieved, suggesting that, upon 2 h milling, equilibrium between cold-welding and fracture is attained. Such behaviour agrees with the observed powder phase evolution (subsection 4.4.5.2. XRD results and discussion). XRD analysis disclosed that, shortly after 2 h milling, a steady state is achieved with all peak intensities (of β-Sn, Li_2Sn_5, and LiSn phases) being similar.

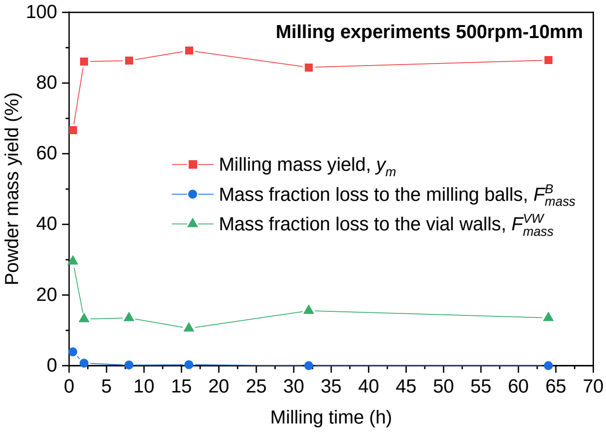

Figure 4.3 - Powder mass yield evolution with milling time for milling experiments with 500rpm-10mm, run for 0.5 h, 2 h, 8 h, 16 h, 32 h and 64 h.

4.1.1. Milling mass yield evolution with time conclusions

The complex stochastic nature of the mechano-synthesis process, together with the fact that only one milling experiment for each milling time was carried out, do not allow to draw accurate conclusions on the influence of milling parameters on the milling mass yield. For each milling time, further milling experiments should be carried out for the results to present a higher confidence level.

Milling efficiency of 50Sn-Li alloy has revealed to be considerable larger than of Li-Sn alloys with Li content below 25 at. %. Overall, all milling experiments present milling mass yields above 40 %, more than double of previously reported results. The observed difference in milling efficiency is due to the difference in powder phase composition. Milled powders are predominantly composed by a base LiSn composition, plus Li_2Sn_5, or even small crystallite Li-rich Li-Sn intermetallics. These are not as ductile as the pure metals, and their formation accounted for the reversal of the predominant adhesion and cold-welding behaviour of the powder batches, with strain hardening and fracture competing against cold-welding.

As milling progresses, loss of process efficiency is observed due to material adhesion and cold-welding to the milling media. The main source of material loss is powder adhesion and cold-welding to the vial walls, with a general increasing tendency with milling time. Adhesion, and cold-welding to the milling balls, is responsible for less than 10% of the total mass loss.

Milling experiments with 500rpm-10mm produce the most promising results as the mass loss rising trend was countered. Shortly after 2 h milling, a quasi-steady state is achieved between cold-welding and fracture, with an almost stationary milling mass yield, $y_M \sim 86\%$, up to 64 h milling.

4.2. 50Li-Sn powder composition analysis

In this section, composition homogeneity of 4 samples from milling experiments 500rpm-10mm, run for 0.5 h, 2 h, 8 h, and 16 h is discussed. As previously described, Ø9 x 2 mm pellets were prepared and loaded in the IBA stage. A nuclear microprobe, with an image pixel size of 3 x 3 μm^2, was used to scan 512 x 512 μm^2 areas, each sample being scanned twice. For each sample, only one scan is presented in this section, the second scan can be consulted on Appendix A.

4.2.1. IBA results and discussion

It should be noted that calibration of the collected particles' signals, using standard samples, was not carried out. For this reason, no numerical scale, and instead a colour scale is presented. Warmer tones indicate that higher overlapping of particles in the detector was registered. Therefore, analysis of elemental maps should bear in mind that the collected particles' yields are affected by the energy of the particles and the cross-sections of the events. The ascending order of energy, of the emitted particles selected for the present study, is: Sn RBS backscattered protons yield < ^4He particles emitted by the $^7Li(p,\alpha)^4He$ nuclear reaction (the NRA yield). On the other hand, cross-sections of the respective events have the opposite trend. The descending order of cross-sections, is: backscattered protons > ^{4}He particles. Thus, although protons backscattered by Sn nuclei have lower energy than the emitted ^{4}He particles, their emission has higher cross-sections, resulting in higher overlapping of particles in the detector, and hence in warmer tones in the elemental maps. Nevertheless, the high energy of the emitted ^{4}He particles avoids the superposition of most of the NRA yield with the RBS one, enabling the identification and quantification of Li amounts.

At lower energy, the ^{7}Li-RBS yield, related to the backscattering of protons by ^{7}Li, is also observed. However, the cross-section of the events is very low. The ^{7}Li-RBS yield is difficult to observe, as it is superimposed to the Sn-RBS yield and, consequently, it cannot be considered for Li quantification.

Sn X-ray emission peaks are the main components in the Li-Sn PIXE spectra. As a result, Sn amounts are easily quantified by PIXE.

For all four samples from milling experiments 500rpm-10mm run for 0.5 h (Figure 4.4), 2 h (Figure 4.5), 8 h (Figure 4.6), and 16 h (Figure 4.7), a mismatch between Sn-PIXE or Sn-RBS maps, and Li-NRA maps is observed. Although Sn depleted regions (black circles) are observed in Sn-PIXE and Sn-RBS maps, no correspondent Li-rich regions are observed in Li-NRA maps. Moreover, for samples run for 0.5 h (Figure 4.4a and b), 2 h (Figure 4.5a and b), and 16 h (Figure 4.7b) preferred orientation, similar to Sn depleted zones, is observed (dashed arrows). Such observations are most likely a result of surface roughness of the pellets, introduced by the press punch. In the case of PIXE, surface roughness leads to partial absorption of emitted Sn-K_α X-rays by surface asperities, which hinders its detection. In the case of RBS, protons backscattered by Sn nuclei located at surface asperities have distinct pathways inside the sample, which results in distinct energy loss before detection [148]. Furthermore, the roughness effect is more pronounced in PIXE maps, than in RBS maps. This is due to the difference in energy of the emitted Sn-K_α X-rays and backscattered protons and respective cross-sections, as aforementioned. Although the roughness effect cannot be avoided in the case of PIXE, in the case of RBS it can. Due to the observed 50Li-Sn high chemical reactivity in air environment (subsection 4.3.1. XRD context study: 50Li-Sn alloy chemical reactivity in air environment), degradation was expected to occur during sample mounting and the energy window used to map Sn was selected as to avoid possible C and O yields (incident protons backscattered by C or O nuclei), that would mean the formation of Li-air reaction products at the surface (see the grey window at lower energy represented in Figure 4.8). As the C and O yield barriers were not observed, in future work, larger energy windows (corresponding to Sn deeper in the sample) can be considered which will counter the observed surface roughness effect.

Due to the mentioned surface roughness effect, Li maps provide the best information on samples' homogeneity. To map Li, two energy windows were used (grey window at higher energies representing the ^{7}Li(p,α)^{4}He yield in Figure 4.8) so that, if sample degradation occurred, Li segregation to the surface could be detected by the increment. For all samples, the results reveal that the Li in-depth profile (< 20 μm) is constant, with no Li surface segregation observed. Sample from milling experiment run for 2 h is the exception (Figure 4.5 black/white arrows), with an apparent 90 x 35 μm^2 Sn enriched, Li depleted, zone. Nevertheless, in general, nuclear microprobe measurements suggest a homogeneous spread of Li, at a 3 x 3 μm^2 scale, without any relevant Li-enriched zones, even for milling times as short as 0.5 h.

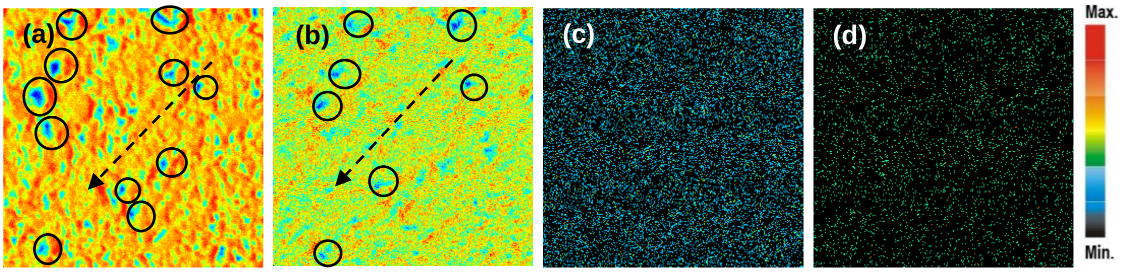

Sn-L$_\alpha$, PIXE Sn, RBS Li bulk, NRA Li surface, NRA

Figure 4.4 - Sample 500rpm-10mm-0.5h (Scan 1). 512 x 512 μm^2 maps of (a) Sn-L$_\alpha$ PIXE/ Sn map obtained from Sn-L$_\alpha$ emission in PIXE spectra, (b) Sn-RBS/ Sn map obtained from Sn barrier in RBS, (c) Li bulk NRA/ Li map obtained from Li barrier in NRA, and (d) Li surface NRA/ Li map obtained from Li barrier in NRA. Dashed arrows: direction of the preferred orientation; black circles: Sn depleted regions.

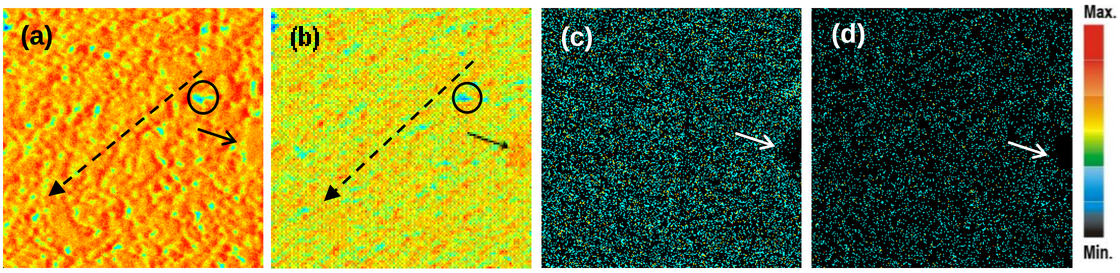

Sn-L$_\alpha$, PIXE Sn, RBS Li bulk, NRA Li surface, NRA

Figure 4.5 - Sample 500rpm-10mm-2h (Scan 1). 512 x 512 μm^2 maps of (a) Sn-L$_\alpha$ PIXE/ Sn map obtained from Sn-L$_\alpha$ emission in PIXE spectra, (b) Sn-RBS/ Sn map obtained from Sn barrier in RBS, (c) Li bulk NRA/ Li map obtained from Li barrier in NRA, and (d) Li surface NRA/ Li map obtained from Li barrier in NRA. Dashed arrows: direction of the preferred orientation; black circles: Sn depleted regions; black/white arrows: Li depleted, Sn rich region.

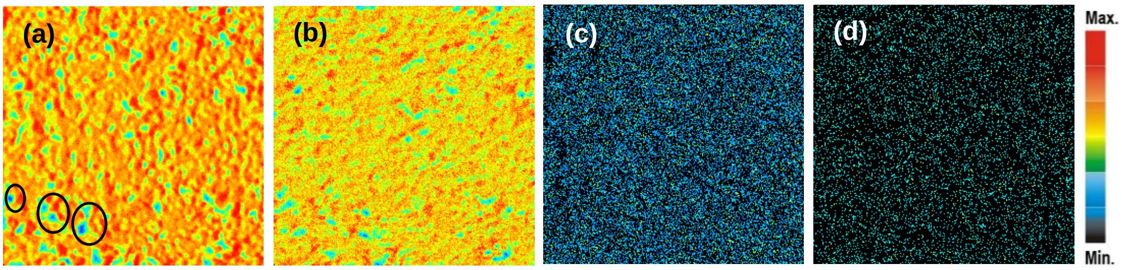

Sn-L$_\alpha$, PIXE Sn, RBS Li bulk, NRA Li surface, NRA

Figure 4.6 - Sample 500rpm-10mm-8h (Scan 1). 512 x 512 μm^2 maps of (a) Sn-L$_\alpha$ PIXE/ Sn map obtained from Sn-L$_\alpha$ emission in PIXE spectra, (b) Sn-RBS/ Sn map obtained from Sn barrier in RBS, (c) Li bulk NRA/ Li map obtained from Li barrier in NRA, and (d) Li surface NRA/ Li map obtained from Li barrier in NRA. Black circles: Sn depleted regions.

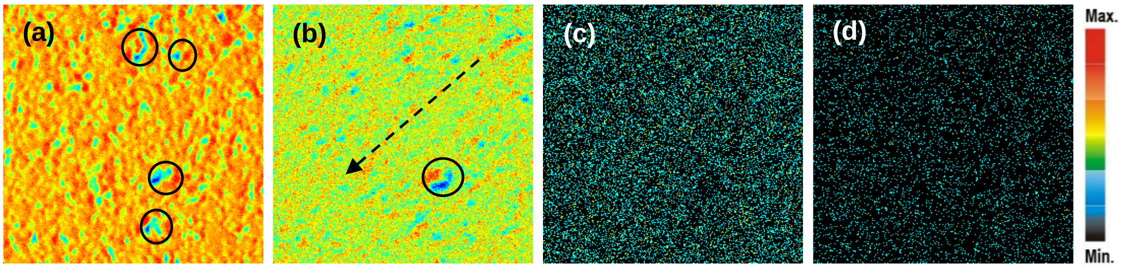

Sn-Lα, PIXE Sn, RBS Li bulk, NRA Li surface, NRA

Figure 4.7 - Sample 500rpm-10mm-16h (Scan 1). 512 x 512 μm^2 maps of (a) Sn-Lα PIXE/ Sn map obtained from Sn-Lα emission in PIXE spectra, (b) Sn-RBS/ Sn map obtained from Sn barrier in RBS, (c) Li bulk NRA/ Li map obtained from Li barrier in NRA, and (d) Li surface NRA/ Li map obtained from Li barrier in NRA. Dashed arrows: direction of the preferred orientation; black circles: Sn depleted regions.

However, such powder homogeneity, from 0.5 h to 16 h milling, suggested by nuclear microprobe measurements does not agree with y_M values and phase evolution observations. Only upon 2 h milling, a quasi-steady state is achieved, with an almost stationary $y_M \sim 86\%$ and with stationary XRD peak intensities of β-Sn, Li_2Sn_5, and LiSn phases. As will be later discussed (subsection 4.4.5.2. XRD results and discussion), the mean crystallite size of formed Li-Sn intermetallics is of the order of ~50 nm, which means that, for a pixel size of 3 x 3 μm^2, nuclear microprobe measurements cannot distinguish between them. This may explain the observed contradicting homogeneity of the 0.5 h milled sample.

As previously referred (subsection 3.3.1. Ion beam analysis (IBA)), only μ-RBS-NRA integral particle spectra from 16 h milled sample could be used for alloy stoichiometry determination. Figure 4.8 shows the μ-RBS-NRA integral particle spectra from 16 h milled sample and the calculated stoichiometry is 58Li-42Sn (at. %). This value approaches to the target value of 50Li-50Sn (at. %), within the limitations of the cross-sections published for the $^7Li(p,\alpha)^4He$ nuclear reaction used for Li quantification [149]. So, milling experiments 500rpm-10mm seem very promising for effective production of the 50Li-Sn alloy. Alloy stoichiometry quantification of the remaining samples will be repeated in the next future, using a broad proton beam.

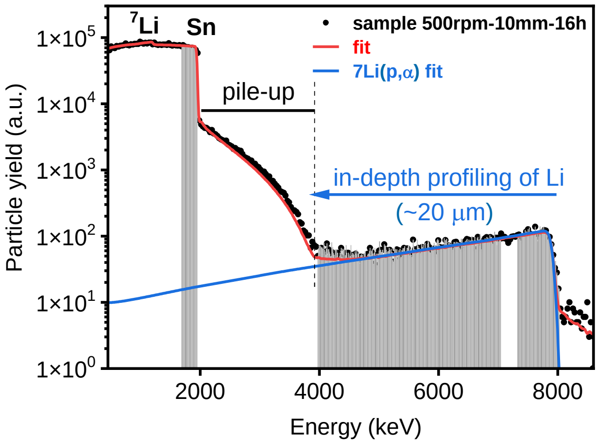

Figure 4.8 - RBS-NRA integral yield spectra collected from sample 500rpm-10mm-16h, and fit line for elemental analysis. Energy ranges used to map Li and Sn represented as grey windows.

The spread homogeneity of Sn could also be followed by PIXE by selecting an energy window in the spectra related to the Sn X-ray peak of higher yield, i.e., the Sn-L$_\alpha$ peak. In the same way, all the remaining elements, as minor contaminants, could be identified and quantified by PIXE by choosing corresponding X-ray emissions of higher yields. For the reason aforementioned, only the integral PIXE yield spectra of 16 h milled sample is presented (Figure 4.9). Besides Sn, PIXE spectra identified the following contaminants: chromium (Cr), iron (Fe), copper (Cu), lead (Pb), and zirconium (Zr). Detection of Zr-K$_\alpha$ and Zr-K$_\beta$ emissions arises from the internal Zr collimator in the detector. To obtain the higher sensitivities needed for PIXE quantification, the corresponding contents were quantified from the yields of the Cr-K$_\alpha$, Fe-K$_\alpha$, Cu-K$_\alpha$ and Pb-L$_\alpha$ emissions, respectively. The source of Cr and Fe contamination is the milling media, which is made from AISI 420C stainless steel, which has an average Cr content of 14.5 wt. % [150]. Pb and Cu contaminants come from the Sn powder itself, according to the supplier. Results from PIXE elemental quantification for the four samples are presented in Figure 4.10. Pb and Cu contents are invariant over time, all below 200 ppm, which agrees with its identified source. However, Cr and Fe content increases with increasing milling time, which is a well-known mechano-synthesis problem [76]. For this reason, milling times should only be long enough as to achieve the steady state phase composition.

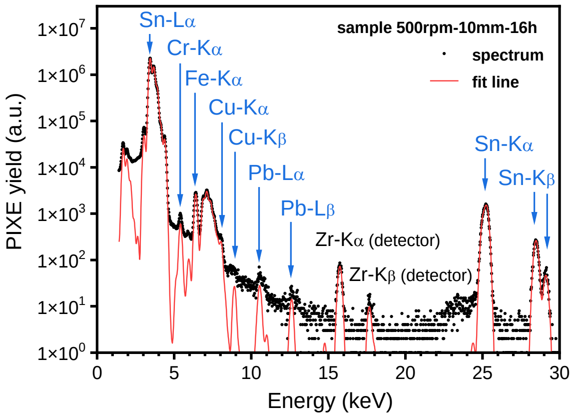

Figure 4.9 - PIXE integral yield spectra collected from sample 500rpm-10mm-16h and fit line for elemental analysis.

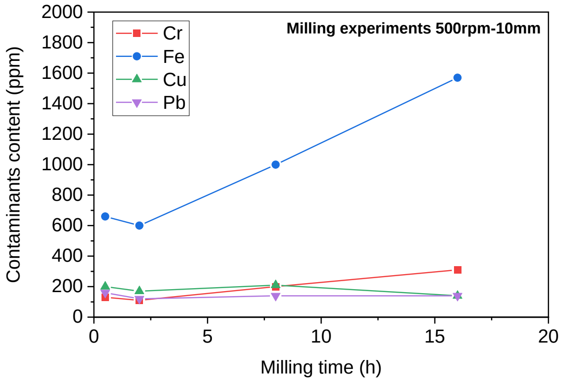

Figure 4.10 - Contaminants content (ppm) evolution with milling time (h), for the milling experiments 500rpm-10mm, determined by µ-PIXE analysis.

4.2.2. Composition analysis conclusions

Nuclear microprobe analysis of samples from milling experiments 500rpm-10mm run for 0.5 h, 2 h, 8 h, and 16 h, have provided valuable information. The collected Sn and Li elemental maps reveal that produced powders present elemental homogeneity, even for the shortest milling time tested 0.5 h. Overall, no Sn, nor Li rich zones were observed, with Li widely spread in the samples. The observed powder homogeneity for the 0.5 h milled sample does not agree with the y_M value and phase evolution observations. Nuclear microprobe pixel size of 3 x 3 µm^2 does not have sufficient resolution to distinguish between the formed Li-Sn intermetallics, LiSn and Li_2Sn_5, with mean crystallite size of ~50 nm.

µ-RBS-NRA quantitative elemental analysis of 16 h milled sample yields an alloy composition of 58Li-42Sn (at. %) which approaches to the target composition of 50Li-50Sn (at. %), within the frame of the fitting model used. Alloy stoichiometry quantification of the remaining samples could not be precisely assessed as the particle detector was not polarized during the analysis. These measurements will be repeated in the next future using a broad proton beam.

µ-PIXE elemental analysis identified the presence of contaminants Cr and Fe, from the milling media, and Cu and Pb, from Sn powder. Cu and Pb content do not vary with milling time, remaining below 200 ppm. Contrarily, Fe and Cr content become larger for longer milling times, increasing from 660 ppm and 200 ppm, for 2 h, to 1570 ppm and 310 ppm, for 16 h, respectively.

4.3. 50Li-Sn powder phase evolution and degradation

This section presents and discusses the structural and phase analysis of the milled products (DSC and XRD). Discussion of the results from the study of 50Li-Sn alloy chemical reactivity in air environment is also presented.

4.3.1. XRD context study: 50Li-Sn alloy chemical reactivity in air environment

X-ray diffraction characterization of the produced 50Li-Sn alloy presents several challenges due to the intrinsic properties of the alloy under study and the underlying fundamental principles of the X-ray diffraction. From the equilibrium point of view, a 100 % LiSn phase composition is expected for a perfect equimolar Li-Sn alloy, after severe mechano-synthesis processing. In the starting stages of the mechano-synthesis process, mixtures with unreacted (Li) and β-Sn phases would be anticipated, which, as processing progresses, would evolve into mixtures of the LiSn phase with Li-rich and Sn-rich Li-Sn intermetallics. However, due to Li high diffusivity and chemical reactivity with atmospheric gases (O_2, N_2, H_2O, and CO_2), surface formation of Li-rich air reaction products inevitably occurs, compromising sample integrity. This Li mass transport to the surface depletes the existing Li-Sn intermetallics of their Li content, leading, in a cascade reaction process, to an increase of the surface molar fraction of less rich Li Li-Sn intermetallics and finally, as a consequence of full Li depletion, to β-Sn.

In this work, a sample stage with no controlled atmosphere was used. Therefore, sample exposure to atmospheric gases during XRD analysis needed to be mitigated. Liquid paraffin was considered as a possible surface diffusion barrier as it considered to be inert regarding Li [128]. This subsection discusses the results of the preliminary XRD Context Study conducted to assess the feasibility of XRD use to characterize the produced 50Li-Sn alloy. Subsection 4.3.1.1. XRD analysis deliberates on the suitability of liquid paraffin as a protective coating. Subsection 4.3.1.2. DSC and GA complementary analysis critically examines the results from the complementary characterization techniques employed to support the XRD observations.

For this study, XRD tests were carried out on 500rpm-10mm-8h powder film samples. One XRD run was carried out on each two samples exposed to air for ~258 min prior to XRD analysis, one coated with paraffin and another uncoated; and five consecutive XRD runs were carried out on another set of two coated and uncoated unexposed samples (with only ~2 min exposure to air, prior to XRD start, corresponding to sample preparation delay time).

4.3.1.1. XRD analysis

Li-Sn alloys reactivity toward atmospheric gases is a relatively understudied topic. The reactivity of solid samples of 25Li-Sn (at. %) alloy was studied in air, water, and steam environments in the 150 – 300 ºC temperature range [10]. Samples oxidized for 180 h at 200 ºC presented Li_2CO_3, and traces of Li_2O and SnO. As previously mentioned in subsection 2.2.1. Physical and chemical properties of Lithium (Li), when Li is exposed to air, depending on the moisture content and temperature, a mixture of LiOH, Li_2CO_3, and Li_2O can form. At 25 ºC, the standard Gibbs free energy of formation of these Li-air reaction products is -439 kJ/Li atom [151], -566 kJ/Li atom [152], and -281 kJ/Li atom [153], respectively. Although Li_2CO_3 has the lowest free energy of formation, it depends kinetically on the formation of LiOH. So, it is reasonable to expect these two phases to be predominant when Li-Sn alloys are exposed to air at NTP conditions. Indeed, a surface content increase in Li, C, and O has been reported for a 5Li-Sn (at. %) alloy exposed to air during IBA sample handling [12].

Figure 4.11 and Figure 4.12 display the XRD diffractograms obtained in the XRD Context Study, following the procedure described in subsection 3.3.2.2. XRD Diffractometer and Test Parameters. Figure 4.11 shows that the diffractogram of a paraffin coated film sample exposed to air for 11 min is overall very similar to that of a coated film sample exposed to air for 258 min. These diffractograms present, besides β-Sn, strong Li_2Sn_5 and LiSn peaks. Contrarily, an uncoated film sample, air exposed for 258 min, presents almost only β-Sn peaks. These results clearly confirm the suitability of liquid paraffin as an effective protective coating when film samples are exposed to air prior to XRD analysis.

However, no expected, particularly for the uncoated sample, LiOH, Li_2CO_3, nor Li_2O peaks are observed in the diffractograms. This absence is also noticeable in the remaining diffractograms (Figure 4.12). Therefore, a complementary GA analysis (discussed in subsection 4.3.1.2. DSC and GA complementary analysis) was conducted to confirm the formation of Li-air reaction products when 50Li-Sn alloy is exposed to air, at NTP conditions.

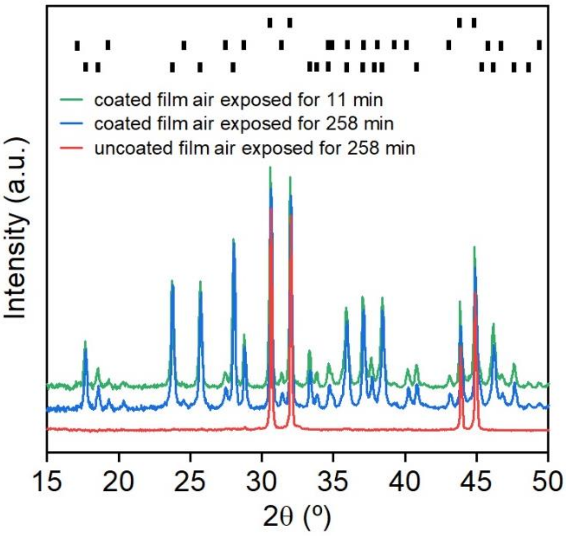

Figure 4.11 - Diffractograms of coated film sample air exposed for 11 min, coated film sample air exposed for 258 min, and uncoated film sample air exposed for 258 min. The patterns of β-Sn (first row), Li_2Sn_5 (second row), and LiSn (third row) are shown. All 500rpm-10mm-8h samples.

The coated film sample diffractograms (Figure 4.12a) show an unexpected loss of liquid paraffin protective capability. Diffractograms from the coated and uncoated film samples exposed for ~27 min are very similar, which indicates that liquid paraffin poorly retarded sample degradation at an early stage. The same similarity is observed among the coated and uncoated film samples exposed for ~43 min. Yet, Li_2Sn_5 and LiSn peak intensity is considerable larger in the coated film samples exposed for ~59 min and ~74 min when compared to their corresponding uncoated counterparts. This may suggest that, in the context of XRD analysis, liquid paraffin still presents protective capability, but the level of protection is much lower.

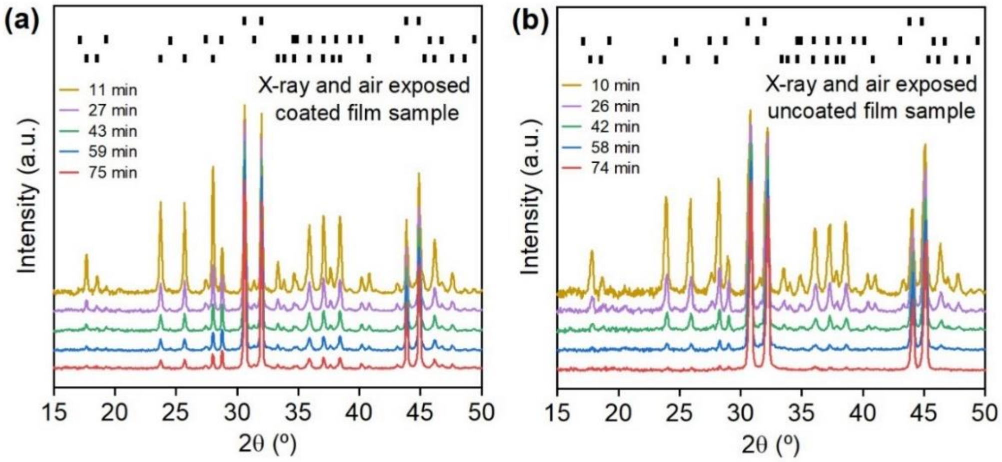

Figure 4.12 - (a) diffractograms from coated film sample during X-ray and air exposure for 11 min, 27 min, 43 min, and 75 min. (b) diffractograms from uncoated film sample during X-ray and air exposure for 10 min, 26 min, 42 min, and 74 min. The patterns of β-Sn (first row), Li_2Sn_5 (second row), and LiSn (third row) are identified. All 500rpm-10mm-8h samples.

Rietveld refinement was carried out to extract information on the phase atomic fraction evolution with X-ray and air exposure time. The refinement model adopted is detailed in subsection Rietveld Refinement. For the experimental XRD diffractograms and their respective simulated fits, please refer to Appendix B. Possible Li-air reaction products (LiOH, Li_2CO_3, nor Li_2O) were not included in the refinement model because, as there are no peaks from these phases in the diffractograms, the only value of phase atomic fraction which would minimize R_{wp} is 0. Therefore, only β-Sn, LiSn, and Li_2Sn_5 phases were considered in the refinement model. However, as one or more Li-air reaction products are indeed forming (as the GA analysis revealed and later discussed in subsection 4.3.1.2. DSC and GA complementary analysis), the values obtained from Rietveld Refinement are inevitably underestimated regarding Li atomic concentration. Also, during each individual XRD run, the sample is continuously degrading, as such, one diffractogram entails information of more than one sample degradation "condition" (of more than one time instant). For higher 2θ values, peaks intensity may be unproportionally lower, which naturally impacts the quality of the Rietveld Refinement results. Each diffractogram was considered to correspond to the middle time of each run.

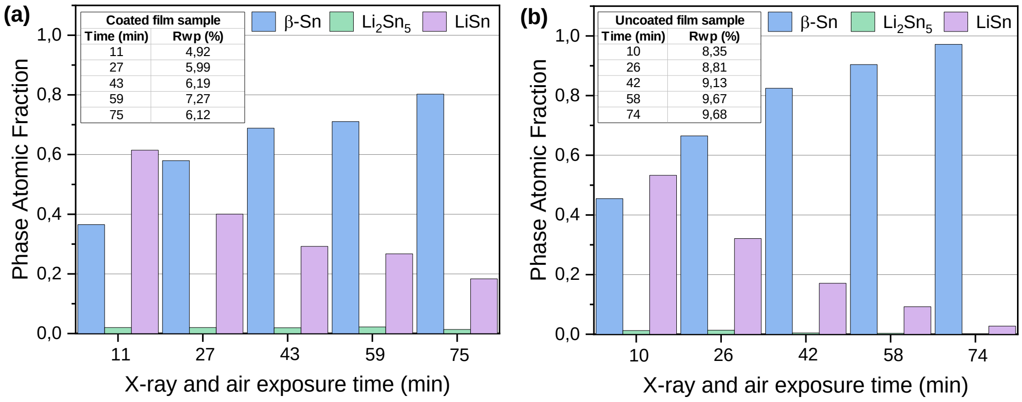

Figure 4.13 - Rietveld refinement results. Phase atomic fraction evolution with X-ray and air exposure time for: (a) coated film sample, and (b) uncoated film sample. All 500rpm-10mm-8h samples.

Figure 4.13 summarizes the values of the obtained phase atomic fractions together with the corresponding R_{wp} value. The model considered proved to be a reasonable fit of the experimental data, with all R_{wp} < 10%. It is perceptible an increase in R_{wp} values with increasing degradation time which stems from the increasing difficulty in fitting LiSn and Li_2Sn_5 peaks' profile as their intensity decreases. Thus, the R_{wp} values of the uncoated film sample are higher than those of the coated film sample.

It can be concluded, comparing coated and uncoated film samples exposed to X-ray and air for ~10 min, that the liquid paraffin coating prevents a 10 at. % increase in β-Sn, and an 8 at.% and a 0.8 at.% decrease in LiSn and Li_2Sn_5, respectively. As X-ray exposure increases, the liquid paraffin coating loses its protective capability and progressive degradation of the coated sample occurs. Bedolla *et al.* [154] proposed a multi-step degradation process of paraffin due to exposure to soft X-rays: X-ray exposure induces the scission of the C-C and C-H bonds of paraffin, and the following exposure to air promotes the adsorption of environmental oxygen and water, resulting in paraffin oxidation. In the present study, hard X-rays were used, which are more energetic than soft X-rays, so it is likely that the observed loss in liquid paraffin protective capability may be attributed to this process. As will be seen in subsection 4.3.1.2. DSC and GA complementary analysis, such hypothesis is sustained by GA measurements, in which no mass gain is detected for the sample coated with liquid paraffin.

Therefore, for full protection from degradation the ideal solution would be designing a portable air-tight argon-filled X-ray sample holder, similar to the one used by Dunlap *et al.* [6] in their study of the Li-Sn system. Such sample holder could not be produced in the context of the present work. Thus, although not the best solution, liquid paraffin protection was the solution of choice and XRD collection time needs to be short.

4.3.1.2. DSC and GA complementary analysis

To complement the above XRD experiments, DSC and GA analysis was conducted. DSC analysis intended to identify the pristine phase composition of the powders, whereas GA analysis aimed to confirm the formation of Li-air reaction products as a result of powder exposure to air. Measurement of the specific surface area of the powders by means of the Brunauer-Emmett-Teller (BET) method, using Kr as an analysis gas, would be important to determine the specific mass gain (mg/cm^2) from GA analysis, however, it could not be carried out in the present work.

Figure 4.14 presents the DSC trace of 500rpm-10mm-8h powder sample, in the 150 - 250 ºC range. In the temperature interval studied, the binary equilibrium Li-Sn phase diagram [59] displays six phase transformations - eutectic melting: $Li_{17}Sn_4$ + (Li) ⟶ Liquid (179 ºC); melting of pure (Li) (180.6 ºC); eutectic melting: Li_2Sn_5 + β-Sn ⟶ Liquid (222 ºC); melting of β-Sn (231.97 ºC), and continuous melting of hypereutectic Li_2Sn_5 (in the temperature interval 222 - 250 ºC) or hypoeutectic β-Sn melting (in the temperature interval 222 - 231.97 ºC). Hence, DSC measurements only allow to access the presence of (Li), β-Sn, $Li_{17}Sn_4$, and Li_2Sn_5 in the samples. The DSC trace of sample 500rpm-10mm-8h registers no phase transformations. This result suggests that LiSn, Li_2Sn_5, and eventually Li-rich Li-Sn intermetallics are the only phases present in pristine milled powders, with no remnant of phase β-Sn that was observed in the XRD analysis. In addition, none of the six aforementioned phase transformations are observed in DSC analysis of samples from milling experiment 500rpm-10mm run for 16 h, 32 h, and 64 h, as discussed later (subsection 4.4.5.1. DSC results and discussion), supporting the hypothesis that LiSn, Li_2Sn_5, and eventually Li-rich Li-Sn intermetallics are the only phases present in these pristine milled powders.

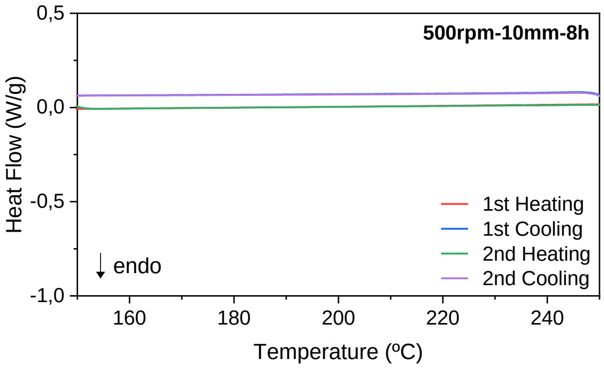

Figure 4.14 - DSC traces of sample 500rpm-10mm-8h.

Figure 4.15 shows the GA traces of powder samples coated and uncoated. A clear difference between the two traces can be observed. It must be noted that the initial small bump observed for the coated sample should not be interpreted as a mass gain but instead as an artifact due to the equipment initial stabilization. Thus, the sample coated with liquid paraffin seems to have suffered no mass change. Contrarily, the uncoated sample experiences a continuous mass change, with a 1.6% mass gain after 3 h exposed to air, at NTP conditions.

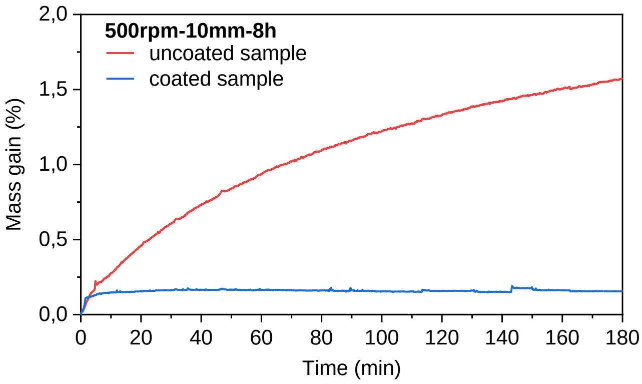

Figure 4.15 - GA traces of samples 500rpm-10mm-8h uncoated (red) and coated (blue).

GA analysis confirms that one or more reaction products form when 50Li-Sn powders are exposed to air, albeit no new peaks are observed in XRD analysis. Such absence is likely due to the low structure factors values of phases with high Li content, and hence low peak intensity values which hampers their detectability, especially when they are not the predominant phases as in the present case (low phase weight fractions). To validate this hypothesis, XRD diffractograms were simulated using GSAS-II software. For each of the three Li-air reaction products likely to be formed (LiOH, Li_2CO_3, and Li_2O), five diffractograms were simulated as to replicate the uncoated film sample test presented in Figure 4.12b. For each exposure time (10 min, 26 min, 42 min, 58 min, and 74 min), the correspondent mass gain observed in the GA analysis was identified and attributed to the formation of a single Li-air reaction product. Then, the phase fraction values of the tested Li-air reaction product were calculated and the phase fractions of β-Sn, LiSn, and Li_2Sn_5, determined by Rietveld Refinement, were corrected considering the progressive increase of the total mass of the sample. This process was repeated for the three possible Li-air reaction products. Having information on the phase weight fraction values, the diffractograms were simulated, being presented in Figure 4.16.

As can be observed, the simulations confirm the proposed hypothesis. For the XRD parameters used, XRD analysis is not able to detect the formation of the Li-air reaction products due to the combined effect of their crystallographic properties and low atomic fractions (and even lower weight fractions).

GA complementary analysis also exposed another important aspect. From 10 min to 26 min of X-ray and air exposure, LiSn atomic percentage decreases ~20 at. % (corresponding to ~10 Li at. % and ~10 β-Sn at. %). However, considering individual Li-air reaction product formation responsible for the observed GA mass gain, from 10 min to 26 min, LiOH formation only accounts for ~0.5 Li at. %, Li_2CO_3 for Li ~0.2 at. %, and Li_2O for Li ~1.3 at. %. Also, an unproportionally ~20 at. % increase of β-

Sn is detected. Thus, besides the effect of the low scattering of Li on diffractions' intensity, another phenomenon must have taken place. X-ray beam depth of penetration depends on the linear absorption coefficient of the sample, X-ray wavelength, and incident angle. For Cu-K_α radiation (1.54 Å = 8.0 keV), the mass absorption coefficient of Sn is 2.5 x 10^2 cm^2/g [155]. For incident angles 2θ = 23.7 ° (most intense LiSn peak) and 2θ = 23.7 ° (most intense Li_2Sn_5 peak), the depth of penetration, for a 90% loss of beam intensity, is 1.29 μm and 1.55 μm, respectively. Thus, it is reasonable to expect that as degradation of 50Li-Sn proceeds and a Li-air reaction products film forms at the particles' surface, the metal layer close to the interface becomes depleted in Li with time, forming a β-Sn layer thick enough to shield XRD penetration and diffraction from the pristine milled powder. Consequently, XRD measurements are biased in favour of the β-Sn phase.

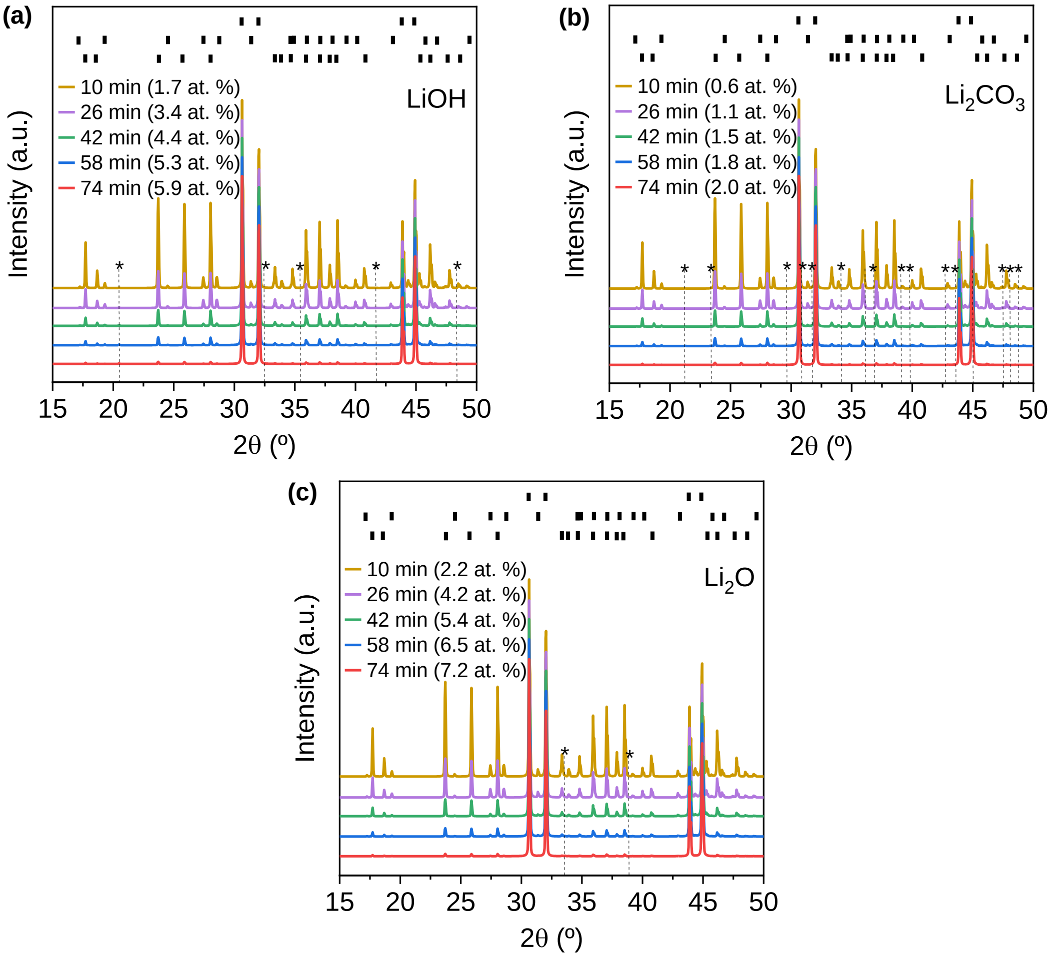

Figure 4.16 - Simulated diffractograms from uncoated film sample during X-ray and air exposure for 10 min, 26 min, 42 min, and 74 min, considering that mass gain observed in GA analysis is due to formation of: (a) LiOH, (b) Li_2CO_3, and (c) Li_2O. The patterns of β-Sn (first row), Li_2Sn_5 (second row), LiSn (third row), and of the tested Li-air reaction products (dashed line plus *) are shown. In brackets, respective Li-air reaction products atomic fraction (at. %), for each exposure time. Sample 500rpm-10mm-8h.

4.3.1.3. XRD Context Study Conclusions

The preliminary XRD Context Study allows to identify vulnerabilities in 50Li-Sn alloy characterization via XRD, when a portable sample stage with controlled atmosphere is not available.

Liquid paraffin proved to be able to retard sample degradation. For long X-ray exposer times, an induced radiation damage process of the protective coating is observed, with liquid paraffin exhibiting a decrease in its level of protective capability. Therefore, a portable air-tight sample holder would have been the best solution to fully mitigate sample degradation during XRD analysis. As such sample holder could not be designed in the present work, protection with liquid paraffin was the methodology adopted. Thus, XRD data collection parameters should be selected as to minimize the total collection time. In order to endow diffractograms interpretation with a higher level of accuracy, DSC and GA complementary analysis was conducted to better understand the degree of protection delivered by the liquid paraffin coating.

DSC analysis, supported by XRD results, suggests that LiSn and Li_2Sn_5, and eventually some Li-rich Li-Sn intermetallics, are the only phases present in the pristine milled powders, with no remnant of the β-Sn phase observed in XRD analysis. GA tests allowed to confirm both the role of X-rays in liquid paraffin loss of protection and the incapacity of XRD technique to detect the formation of Li-air reaction products during 50Li-Sn degradation. Phases with high Li content have low structure factors, and hence low peak intensity values which hampers their detectability, especially when they are not the predominant phases as in the present case. Additional diffractograms simulations carried out confirmed this hypothesis. GA complementary analysis also exposed the bias of XRD towards β-Sn phase. From 10 min to 26 min of X-ray and air exposure, the atomic fraction of Li calculated to have been consumed by Li-air reaction products (~0.5 at. % for LiOH, ~0.2 at. % for Li_2CO_3, and ~1.3 at. % for Li_2O) was considerably lower than the atomic fraction of Li calculated to have been lost (~10 at. %). It is proposed that, as degradation proceeds, Sn-enrichment of the metal layer in the vicinity of the reaction layer interface reduces the X-ray beam depth of penetration, due to Sn high linear absorption coefficient; therefore, LiSn and Li_2Sn_5 detectability decreases and XRD measurements become biased in favour of β-Sn phase.

In summary, the results from the preliminary XRD Context Study imply that, when interpreting XRD results, the aforementioned effects of sample degradation and XRD bias towards β-Sn phase should be carefully considered.

4.3.2. 50Li-Sn powder phase evolution with milling time

The study of phase evolution with time of the mechano-synthesised equimolar 50Li-Sn alloy was carried out through DSC analysis, in the 150-250 ºC temperature range, and XRD analysis of film powder, pellet, and discs samples in the 15-50º 2θ range.

4.4.5.1. DSC results and discussion

In this subsection, DSC analysis of 11 samples is discussed: 6 samples from milling experiments 500rpm-10mm, run for 0.5 h, 2 h, 8 h, 16 h, 32 h, and 64 h, and 5 samples from milling experiments run for 8 h (150rpm-6mm, 150rpm-10mm, 150rpm-15mm, 500rpm-6mm, and 500rpm-15mm). As previously described (subsection 3.3.3. Differential scanning calorimetry (DSC)), the thermal cycle used was composed by four segments, in the 150-250 ºC temperature range: two heating cycles plus two cooling cycles.

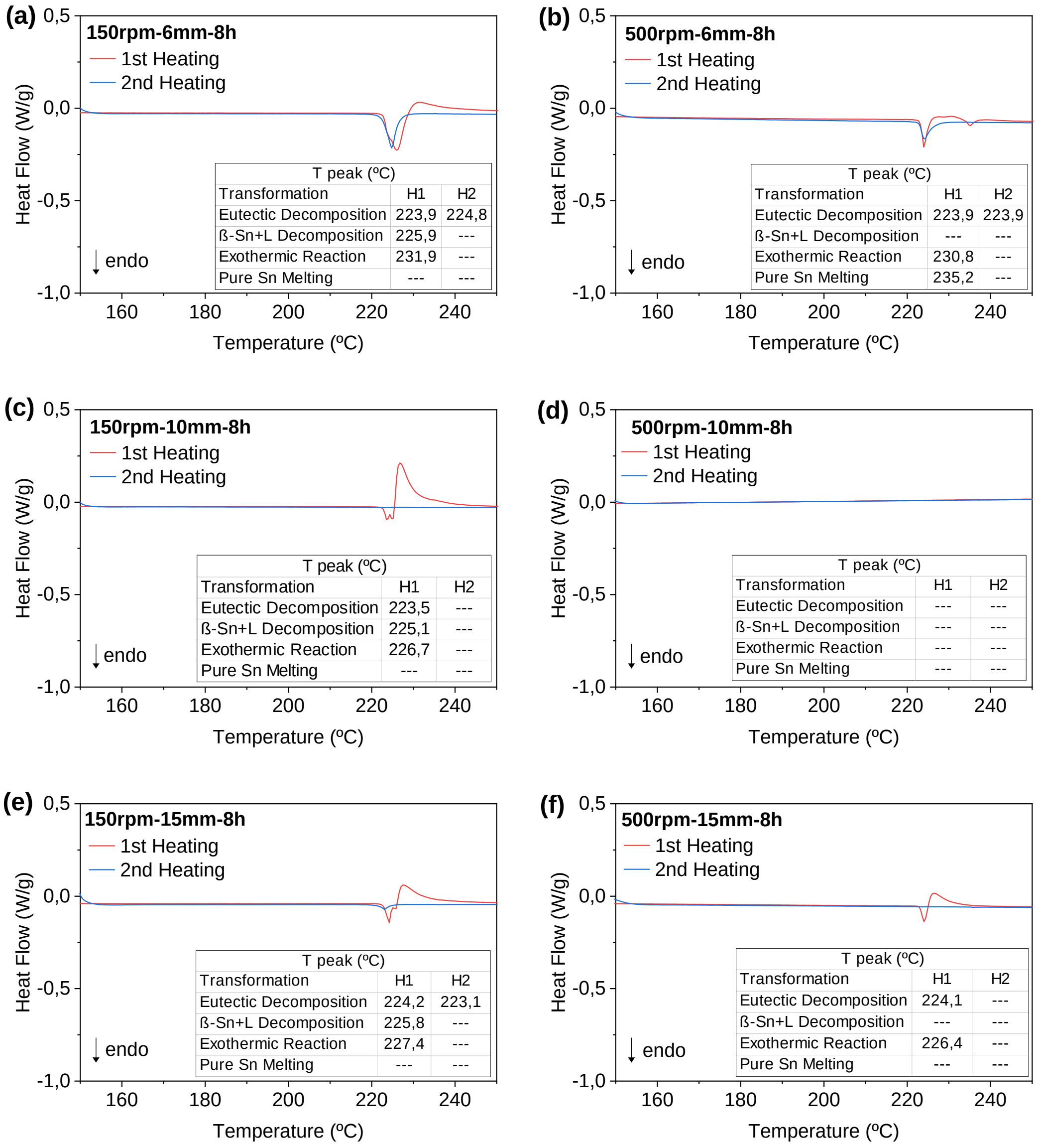

(a)

	T peak (ºC)	
Transformation	H1	H2
Eutectic Decomposition	223,9	224,8
ß-Sn+L Decomposition	225,9	---
Exothermic Reaction	231,9	---
Pure Sn Melting	---	---

(b)

	T peak (ºC)	
Transformation	H1	H2
Eutectic Decomposition	223,9	223,9
ß-Sn+L Decomposition	---	---
Exothermic Reaction	230,8	---
Pure Sn Melting	235,2	---

(c)

	T peak (ºC)	
Transformation	H1	H2
Eutectic Decomposition	223,5	---
ß-Sn+L Decomposition	225,1	---
Exothermic Reaction	226,7	---
Pure Sn Melting	---	---

(d)

	T peak (ºC)	
Transformation	H1	H2
Eutectic Decomposition	---	---
ß-Sn+L Decomposition	---	---
Exothermic Reaction	---	---
Pure Sn Melting	---	---

(e)

	T peak (ºC)	
Transformation	H1	H2
Eutectic Decomposition	224,2	223,1
ß-Sn+L Decomposition	225,8	---
Exothermic Reaction	227,4	---
Pure Sn Melting	---	---

(f)

	T peak (ºC)	
Transformation	H1	H2
Eutectic Decomposition	224,1	---
ß-Sn+L Decomposition	---	---
Exothermic Reaction	226,4	---
Pure Sn Melting	---	---

Figure 4.17 - DSC traces of samples: (a) 150rpm-6mm-8h, (b) 500rpm-6mm-8h, (c) 150rpm-10mm-8h, (d) 500rpm-10mm-8h, (e) 150rpm-15mm-8h, (f) 500rpm-15mm-8h.

As mentioned before, in the studied temperature range, the binary equilibrium Li-Sn phase diagram [59] displays five invariant reactions and the continuous melting of hypereutectic Li_2Sn_5 or hypoeutectic β-Sn. Figure 4.17 shows the DSC traces of the 8 h milled samples for the six milling conditions studied. For none of the samples, pure Li melting was detected.

For the first heating cycle, all samples, except sample 500rpm-10mm-8h, present the 222 ºC eutectic peak (Li_2Sn_5 + β-Sn ⟶ Liquid), meaning that unreacted β-Sn and Li_2Sn_5 are present in the powders. Superposed to the eutectic peak, all samples milled at 150 rpm (Figure 4.17a, c, e) display another peak, of variable size, located at ~225 ºC, corresponding to hypereutectic or hypoeutectic melting, respectively of Li_2Sn_5 or β-Sn. Sample 500rpm-6mm-8h is the only one presenting the pure β-Sn melting peak (Figure 4.17b). Besides these peaks, an exothermic peak, also of variable size, is observed in all samples, also except for sample 500rpm-10mm-8h (Figure 4.17d).

In the second heating cycle, the eutectic peak remained for samples 150rpm-6mm-8h and 500rpm-6mm-8h; decreased in sample 150rpm-15mm-8h; and vanished for samples 150rpm-10mm-8h, and 500rpm-15mm-8h. Also, for all samples, both the endothermic pro-eutectic peak and the exothermic peak are no longer detected.

The DSC cooling traces (Figure 4.18) of most samples present no endothermic peaks. Moreover, the expected exothermic peaks, corresponding to the reversed melting reactions, are either absent (samples 150rpm-10mm-8h (1st and 2nd cycles), 500rpm-10mm-8h (1st and 2nd cycles) and 500rpm-15mm-8h (1st and 2nd cycles)), or present a rather delayed (lower temperature) and much less intense crystallization phenomena, eventually related to the eutectic crystallization (samples 150rpm-6mm-8h (1st cycle), and 150rpm-15mm-8h (1st and 2nd cycles)). The only exception is sample 150rpmm-6mm-8h (2nd cycle) that presents two peaks. Sample 500rpm-6mm-8h, below 200 ºC, presents some serrated small exothermic peaks (1st and 2nd cycles).

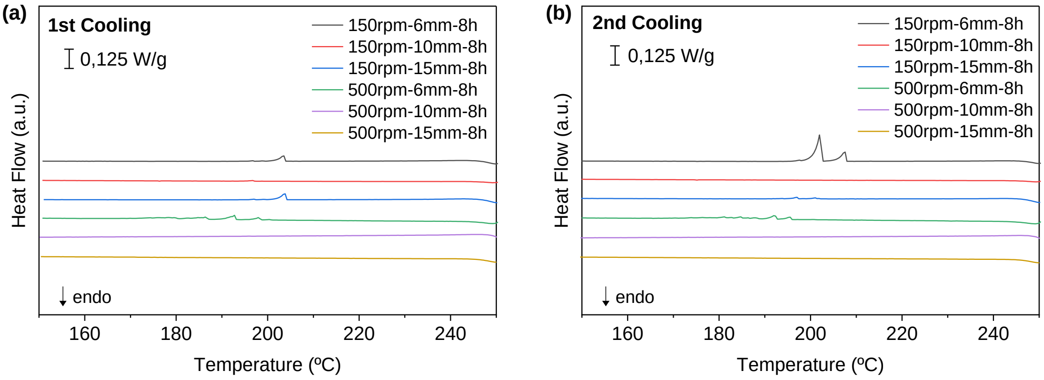

Figure 4.18 - DSC cooling curves for all samples milled for 8 h.

The disappearance, on the second cycle, of the eutectic and pro-eutectic peaks, corroborated by the inexistence of the corresponding exothermic crystallization peaks during cooling, implies that Sn has formed a stable compound that does not decompose or melt below 250 ºC. According to the Li-Sn equilibrium binary phase diagram [59], for the studied 50Li-Sn system, if unreacted β-Sn is present, a 95 at. % Sn liquid (5 at. % Li) should form at the eutectic temperature, 222 ºC. At 250 ºC, maximum temperature studied, the liquidus line in equilibrium with Li_2Sn_5 has 91 at. % Sn (9 at. % Li). As will be discussed in subsection 4.4.5.2. XRD results and discussion, XRD analysis confirmed the existence of the LiSn intermetallic in all milled samples tested by DSC. Thus, the prevailing DSC exothermic peaks, that form immediately after melting, must be assigned to the reaction between the formed Sn-rich liquid and LiSn (or higher Li content Li-Sn intermetallics) to form further Li_2Sn_5 (or further LiSn). In the context of the 50Li-Sn studied system, this reaction can be considered irreversible as it moves the system towards equilibrium, consuming all unreacted β-Sn present after milling. Therefore, when this reaction progresses to completion, no further events can be detected in the DSC traces.

The known gravity segregation of Li in Sn rich melts [9,10] and the reaction of the formed liquid with DSC aluminium pans can be proposed as accountable for the presence of rather delayed (to lower temperature) exothermic crystallization peaks and some serrated exothermic peaks below 200 ºC, during cooling, and for the behaviour of the sample 150rpm-6mm-8h (2nd cooling cycle). Li buoyancy leads to high surface Li content in the melt, promoting the formation of high Li content, high melting point, Li-Sn intermetallics [9,10] that can disturb the route to equilibrium, hampering peak assignment in the DSC traces [16]. In addition, both Li and Sn form eutectic systems with Al, respectively at 179 ºC [156] and 228 ºC [157]. If the Li-Sn melt overcomes the natural existing Al_2O_3 surface passivation layer of the Al pan, and reaction takes place, the melt can be enriched with aluminium forming a ternary liquid with different eutectic temperatures. In the case of the Al-Li system several intermetallics can also form, rendering the analysis more complex. Analysis of the samples after DSC testing would allow the enlightenment of possible reaction events and will be carried out in the future.

DSC analysis shows that mechano-synthesis of powders milled at 500 rpm proceeded faster. No peaks were detected for sample 500rpm-10mm-8h, which suggests that LiSn and Li_2Sn_5, and eventually Li-rich Li-Sn intermetallics, are the only phases present. The use of 6 mm and 15 mm balls, particularly 6 mm, is not as efficient since the 8 h milled samples still present unreacted β-Sn. On the other hand, all 8 h samples milled at 150 rpm present unreacted β-Sn.

As milling experiments at 500 rpm, using 10 mm balls, revealed to be the most promising due to their high y_M values and the absence of unreacted β-Sn, a DSC analysis of samples from this series milled for 0.5 h, 2 h, 16 h, 32 h, and 64 h was also carried out (Figure 4.19). As observed for the sample milled for 8 h, all samples present no peaks, meaning that no unreacted β-Sn nor (Li) remained in the samples. Sample milled for 2 h is the exception, for which a very small eutectic peak, followed by the referred exothermic peak, is present. Nevertheless, overall DSC analysis indicates that, for 500rpm-10mm milling experiments, shortly after 0.5 h milling, LiSn and Li_2Sn_5, and eventually Li-rich Li-Sn intermetallics, are the only phases present.

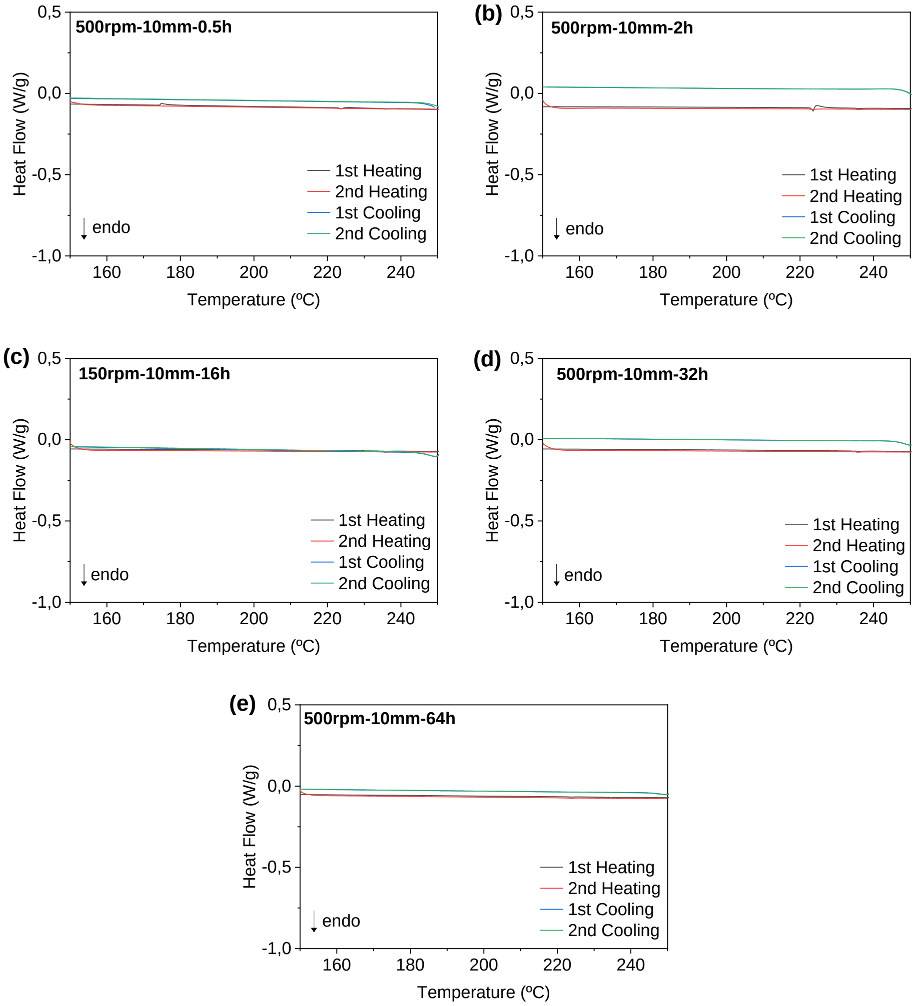

Figure 4.19 - DSC traces of samples from milling experiments 500rpm-10mm milled for: (a) 0.5 h, (b) 2 h, (c) 16 h, (d) 32 h, and (e) 64 h.

4.4.5.2. XRD results and discussion

In this subsection, discussion of XRD analysis of 24 samples is presented. All samples from milling experiments 150rpm-6mm, 150rpm-10mm, 150rpm-15mm, 500rpm-6mm, 500rpm-10mm, and 500rpm-15mm were characterized. Pw (for powder sample), Pl (for pellet sample), and D (for Discs) are the acronyms used for each sample condition. X-ray diffractograms were collected and analysed according to the procedure detailed in subsection 3.3.2. X-Ray diffraction (XRD), using XRD test parameters 15-55: 0.04: 0.8.

Figure 4.20 condenses the postprocessed diffractograms by milling time studied: 0.5 h (Figure 4.20a), 2 h (Figure 4.20b), and 8 h (Figure 4.20c), respectively. Figure 4.21 shows the diffractograms of the disc-like particles samples. As previously referred (subsection 3.2.1. Mechano-synthesis: equipment and process parameters), for certain time conditions, both powders and disc-like particles composed the mechano-synthesised product. For milling experiments with 150 rpm (using 6 mm, and 10 mm balls) and with 500 rpm (using 15 mm balls), disc-like particles were separated from the powders for characterization. Given the sample morphology, these diffractograms present poor quality and considerable background noise. Figure 4.23 groups all diffractograms from samples of the milling experiment with 500 rpm, using 10 mm balls, as these milling parameters seem to promote the highest y_M value. To ease interpretation, the relevant peaks for each phase are represented in the *xy* plane of the graphs by a line. The following line colour/type palette guideline was used: purple (solid) – β-Sn; pink (dash) - Li_2Sn_5; pink (solid) – LiSn; green (solid) - Li_7Sn_3; light blue (dash) - Li_5Sn_2; light blue (solid) - $Li_{13}Sn_5$; dark blue (dash) - Li_7Sn_2, and dark blue (solid) - $Li_{17}Sn_4$. The relative intensities of the three most intense peaks for each phase (four peaks for β-Sn), are represented in the *xz* plane. The red colour is reserved for unidentified peaks.

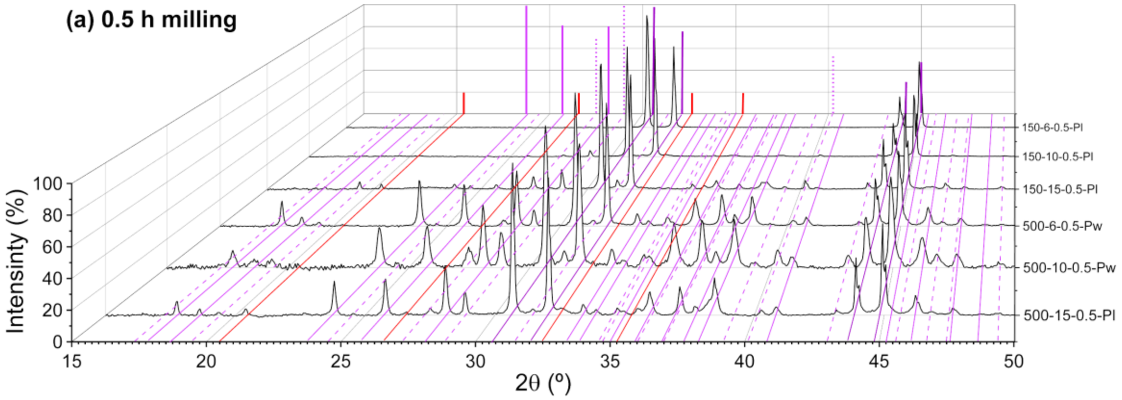

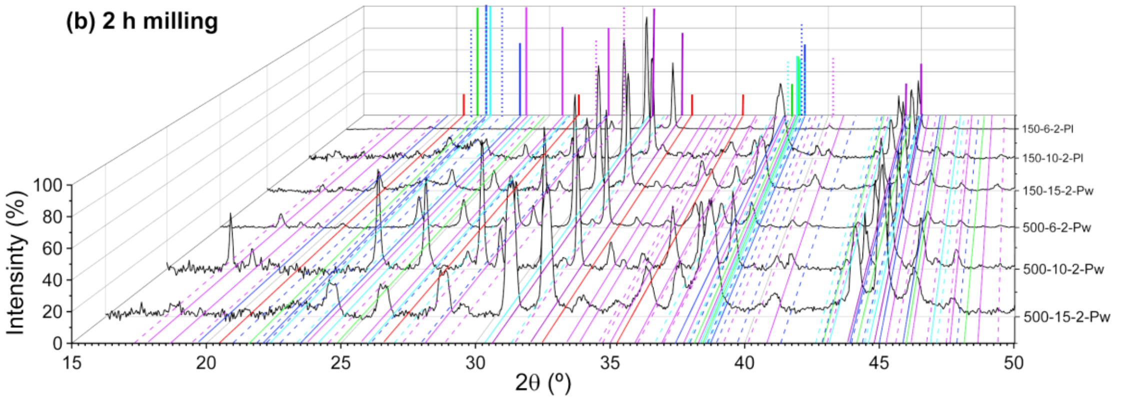

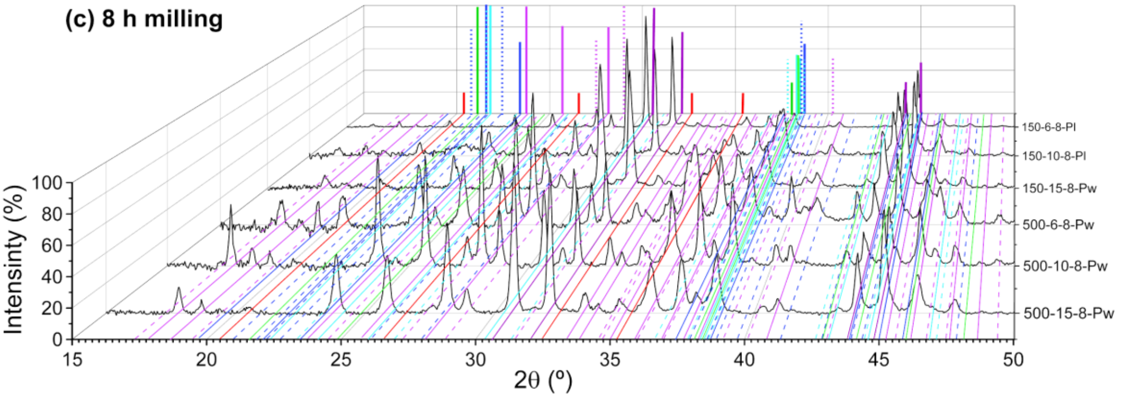

Figure 4.20 - XRD diffractograms of 50Li-Sn powders (Pw) and pellet (Pl) samples milled for: (a) 0.5 h, (b) 2 h, and (c) 8 h. Phase pattern code: β-Sn (solid purple), Li_2Sn_5 (dash pink), LiSn (solid pink), Li_7Sn_3 (solid green), Li_5Sn_2 (dash light blue), $Li_{13}Sn_5$ (solid light blue), Li_7Sn_2 (dash dark blue), and $Li_{17}Sn_4$ (solid dark blue), and unidentified peaks peaks (solid red).

After 0.5 h milling (Figure 4.20a), for powder (Pw) and pellet (Pl) samples milled at 150 rpm, detected peaks evolve, as the milling balls' diameter increases from 6 mm to 10 mm and to 15 mm, from single β-Sn to β-Sn and Li_2Sn_5, and to β-Sn, Li_2Sn_5 and LiSn, respectively. For all samples milled at 500 rpm, β-Sn, Li_2Sn_5 and LiSn peaks are clearly identified, although with different intensities.

After 2 h milling (Figure 4.20b), peaks of β-Sn, Li_2Sn_5 and LiSn are present for all powder and pellet samples, except for sample 150rpm-6mm-2h-Pl, for which no LiSn peaks are observed. It is noticeable the differences in peak intensities of phases Li_2Sn_5 and LiSn among the different samples. Peaks of Li-rich intermetallics also emerged: three large bumps distributed in the 2θ ranges of [20.8º; 24.0º], [36.4º; 41.2º], and [42.3º; 48.0º] can be observed in samples 150rpm-10mm-2h-Pl, 150rpm-15mm-2h-Pw, and 500rpm-15mm-2h-Pw. These bumps coincide with the position of the most intense peaks of the five Li-rich Li-Sn intermetallics, respectively Li_7Sn_3, Li_5Sn_2, $Li_{13}Sn_5$, Li_7Sn_2 and $Li_{17}Sn_4$. As will be discussed later in this subsection, precise phase identification of Li-rich Li-Sn intermetallics proved to be difficult.

After 8 h milling (Figure 4.20c), all powder and pellet samples (except sample 150rpm-10mm-8h-Pl which presents the above mentioned diffraction bumps, suggesting the presence of Li-rich Li-Sn intermetallics) only display diffraction peaks corresponding to β-Sn, Li_2Sn_5, and LiSn.

Analysis of disc samples (Figure 4.21) shows that (Li) peak is observed for all samples, except for sample 150rpm-10mm-2h-D. Considering the very low scattering factor of Li, its detection indicates that (Li) is a main constituent phase, implying that these discs correspond to under-reacted original Li cuts, that somehow encompass their original shape, albeit the milling action. For samples milled at 150 rpm for 0.5 h, the relative intensity of the (Li) peak is considerable higher. Moreover, all samples milled at 150 rpm present the referred characteristic bumps of Li-rich Li-Sn intermetallics (2θ ranges of [20.8º; 24.0º]; [36.4º; 41.2º]; [42.3º; 48.0º]). Particularly, in sample 150rpm-6mm-0.5-D, it is again noteworthy the intensity of the large broad peak located in the second bump at $2\theta = 38.4°$. Samples 150rpm-10mm-0.5h-D, 150rpm-6mm-2h-D, and 150rpm-10mm-2h-D display similar profiles for the [20.8º; 24.0º] bump, suggesting the presence of the same intermetallic. In turn, the two 500rpm-15mm samples are the only ones presenting Sn-rich Li-Sn intermetallic peaks (LiSn for sample 500rpm-15mm-2h-D, and both LiSn and Li_2Sn_5 for sample 500rpm-15mm-8h-D).

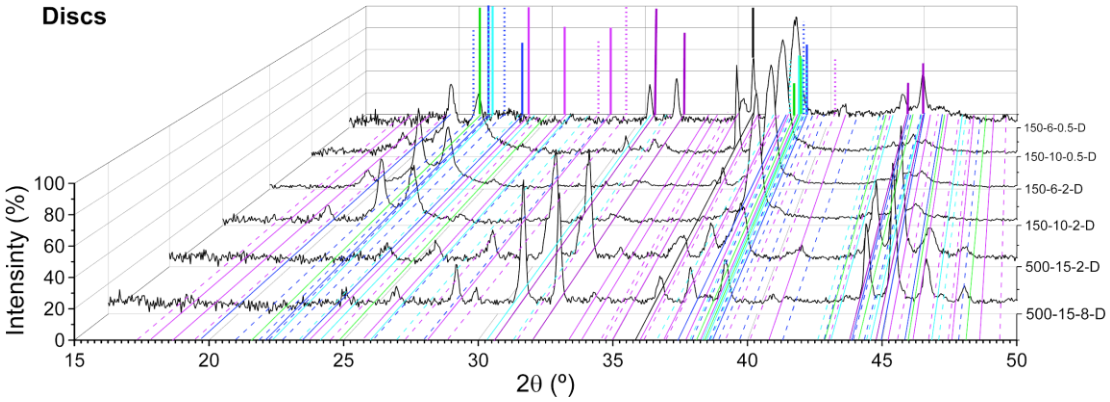

Figure 4.21 - XRD diffractograms of 50Li-Sn disc-like (D) samples. Phase pattern code: β-Sn (solid purple), Li_2Sn_5 (dash pink), LiSn (solid pink), Li_7Sn_3 (solid green), Li_5Sn_2 (dash light blue), $Li_{13}Sn_5$ (solid light blue), Li_7Sn_2 (dash dark blue), $Li_{17}Sn_4$ (solid dark blue), and (Li) (solid black).

XRD analysis of the disc samples complements the observations on the respective powder samples, allowing to conclude that mechano-synthesis progresses in two fronts: Li-rich Li-Sn intermetallics preferentially form at the surface of the initial (Li) cuts, whereas Sn-rich Li-Sn intermetallics preferentially form at the surface of the original β-Sn powders. These two fronts converge, at a later stage, to a base LiSn composition, with Li_2Sn_5 and possibly with small crystallite size Li-rich Li-Sn intermetallics. As will be discussed later in this section, for crystallite sizes of 5 nm, Li-rich intermetallics present a high detection limit (~15 wt.%).

Moreover, complementary XRD analysis of discs and respective powder samples indicates a lower alloying kinetics for the 150 rpm milling rate, whichever ball diameter used. Such observation agrees with the results from DSC analysis, for which unreacted β-Sn was detected for all samples milled at 150 rpm. Milling rate is in this case the most significant milling parameter in the mechano-synthesis kinetics.

As collision power and cumulative energy are proposed to play the governing role in determining the kinetics of MA [99,100], calculations of the cumulative energy released to the powders, as a function of milling time were carried out (Figure 4.22). *Abdellaoui et al.* [99] model was used for calculation of single ball-wall collision energy and single ball-wall collision frequency, whilst *Burgio et al.* [100] model was used to calculate the weight-normalized total collision power and weight-normalized cumulative energy transferred from all the balls to the powders, E_{cum} (see Appendix C). In Figure 4.22, two distinct energy regions are observed, corresponding to milling experiments carried out at the same milling rate: 150 rpm (10-10^4 J/g) and 500 rpm (10^3-10^6 J/g). For a constant milling rate, total energy lies in the same energy region, independently of the milling ball diameter used. Thus, the calculated values of total cumulative energy agree with the higher alloying kinetics observed experimentally for higher milling rates. Higher milling rates result in higher frequency of collision, with higher energy values transferred during collision (see Appendix C), which increases the reaction kinetics. Powders experience intense mechanical deformation, leading to generation of crystal defects, which together with the balance between cold-welding and fracture events among the powder particles is expected to enhance the microstructural changes of the powder [76]. Also, higher milling rates mean higher peak milling temperatures at collisions, which increases the reaction kinetics [76].

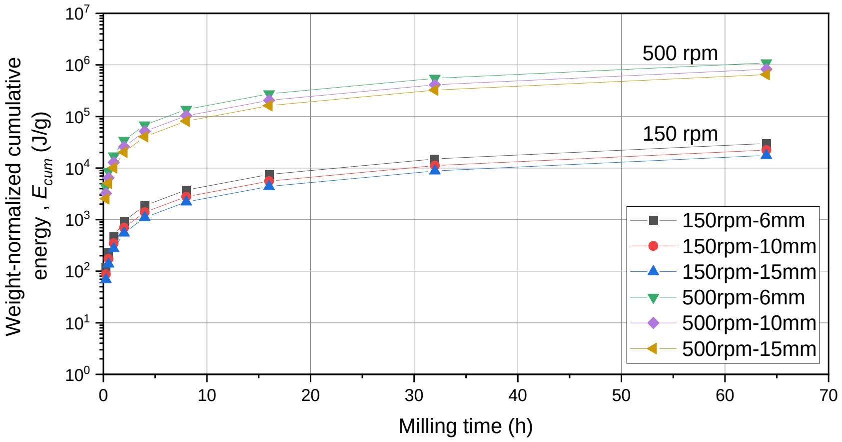

Figure 4.22 - Calculated weight-normalized cumulative energy transferred to the powders, E_{cum}, as a function of milling time. Based on *Abdellaoui et al.* [99] and *Burgio et al.* [100] models.

As milling experiments 500rpm-10mm seem the most promising, presenting the highest y_M value, three additional milling times were studied: 16 h, 32 h, and 64 h. Figure 4.23 groups the diffractograms of the six milling times studied for this milling condition (0.5 h, 2 h, 8 h, 16 h, 32 h and 64 h). It can be observed that the diffractograms of these additional milling times, all corresponding to film powder samples, are very similar, all presenting phases β-Sn, Li_2Sn_5, and LiSn. The unidentified low intensity peak located at 2θ=20.4° is observed for all milling times ≥ 8 h. It seems that shortly after 2 h milling, a steady state is achieved with all peak intensities being similar.

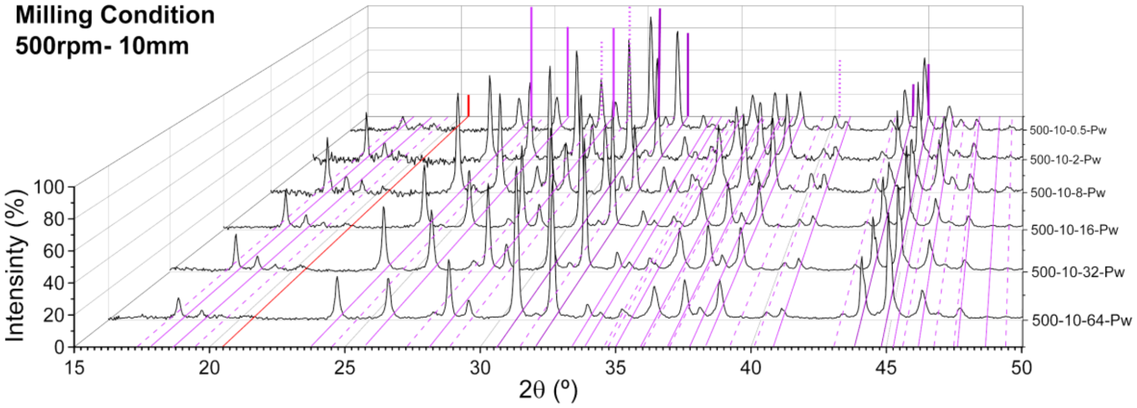

Figure 4.23 - XRD diffractograms of 500rpm-10mm powder samples (Pw) milled for 0.5 h, 2 h, 8 h, 16 h, 32 h, and 64 h. Phase pattern code: β-Sn (solid purple), Li_2Sn_5 (dash pink), LiSn (solid pink), and unidentified peaks (solid red).

The low intensity peaks located at 2θ=16.4°, 2θ=20.4°, 2θ=26.5°, 2θ=32.5°, and 2θ=35.4°, observed in several powder, pellet, and disc samples, could not be identified. These peaks do not match the diffractions of Li-rich Li-Sn intermetallics, nor of possible contaminant phases (SnO, SnO_2, Li_2O, Li_3N, Li_2C_2, LiH, $LiNO_3$, LiN_3O_4, $LiCO_3$, HLiO, and H_3LiO_2). IBA analysis showed that contamination from the milling media is residual. As such, phases resulting from contamination, even if formed, are not likely to be detectable by XRD. Mayo and Morris [51] predicted several new stable and metastable Li−Sn intermetallics. Considering that mechano-synthesis is a non-equilibrium processing method, the possibility of these peaks belonging to a metastable Li-Sn intermetallic should not be excluded. Further investigation would be required to disclose the nature of these low intensity unidentified peaks.

The three large bumps distributed in the 2θ ranges [20.8°; 24.0°], [36.4°; 41.2°], and [42.3°; 48.0°], observed mainly for samples milled for 2 h, coincide with the position of the most intense peaks of the five Li-rich Li-Sn intermetallics. However, precise phase identification proved to be challenging due to the crystallographic properties of these phases. As already mentioned, phases containing Li have peaks with lower intensity values, which hinders their detection. Moreover, Li-Sn phases have structures with low symmetry unit cells, which results in complex diffraction patterns with many peaks. To make phase identification even worse, the three most intense peaks of the Li-rich Li-Sn intermetallics are positioned very close to each other, some even being coincident, such is the case of the most intense peak of $Li_{17}Sn_4$ and Li_5Sn_2.

DSC analysis (subsection 4.4.5.1. DSC results and discussion) was not able to clarify which Li-rich Li-Sn intermetallics were present as these have melting points, or are involved in invariant transformations, outside the tested temperature range. Therefore, to complement the present analysis and to try to evaluate which Li-rich Li-Sn intermetallics could be contributing to the diffractograms observed, XRD diffractograms were simulated using GSAS-II software. For each of the five Li-rich Li-Sn intermetallics, seven simulations were carried out assuming a specific phase weight percentage and crystallite mean size (detailed of the simulation method used was described in subsection Simulation of XRD diffractograms).

The values of crystallite size considered for the simulations were based on the values obtained from Rietveld refinement of the diffractograms of the coated sample 500rpm-10mm-8h. For β-Sn, although a mean crystallite size of ~150 nm was obtained, an overvalue of 500 nm was considered as to be more representative of all samples, in particular samples milled for 0.5 h which have narrower peaks. For both LiSn and Li_2Sn_5, a mean crystallite size value of ~50 nm was obtained, which was used for the simulations. For Li-rich Li-Sn intermetallics, crystallite size was set as equal to those of Sn-rich intermetallics (50 nm). The high peak intensity observed for these Li-rich Li-Sn intermetallics (e.g.: Figure 4.20b, samples 150rpm-10mm-2h-Pl and 150rpm-15mm-2h-Pw) indicates high weight percentage values. Thus, the first simulations assumed a weight percentage of 40 wt.%, receiving the acronym 40wt.%-50nm.

Figure 4.24 comprises all carried out simulations. These simulations reveal that a broad and intense peak is indeed expected to occur in the [36.4º; 41.2º] 2θ range for $Li_{17}Sn_4$ (Figure 4.24a), Li_7Sn_2 (Figure 4.24b), $Li_{13}Sn_5$ (Figure 4.24c), and Li_7Sn_3 (Figure 4.24e), as observed in some experimental diffractograms (Figure 4.20b, samples 150rpm-10mm-2h-Pl, 150rpm-15mm-2h-Pw, and 500rpm-15mm-2h-Pw). However, the simulated profiles for the [20.8º; 24.0º] 2θ range, do not match the experimental results, that are much broader and less intense, suggesting a much smaller crystallite size. Thus, for a new set of simulations, the crystallite size of the Li-rich Li-Sn intermetallics was set to 5 nm and, to evaluate the sensitivity and limit of detectability of theses phases, different weight percentages (from 60 to 15 wt. %) were tested. Bearing in mind the high diffusivity of Li, the assumption of a 5 nm mean crystallite size can be considered a radical limit approximation, as these will tend to coarsen rapidly by Ostwald ripening.

For all five Li-rich Li-Sn intermetallics, the simulated profile, in the [20.8º; 24.0º] 2θ range, considering a 5 nm mean crystallite size was much similar to the experimental. However, the simulated profile in the [36.4º; 41.2º] 2θ range no longer agreed with the experimental. So, the experimental diffractograms seem to present conflicting features corresponding to either small crystallite sizes ([20.8º; 24.0º] 2θ range), or larger crystallite sizes ([36.4º; 41.2º] 2θ range). For crystallite sizes of 5 nm, this set of simulations also disclosed a considerably high detection limit (~15 wt.%) and low sensitivity for Li-rich Li-Sn intermetallics. Even for 60 wt.%, the reflections' intensity remains very low, below 30 % and close to the background level.

None of the previous simulations allowed to identify the Li-rich Li-Sn intermetallics present in samples 150rpm-10mm-2h-Pl, 150rpm-15mm-2h-Pw, and 500rpm-15mm-2h-Pw. They reinforced the known complexity and similarity of the diffractograms of these phases [37,67–70]. Nonetheless, a clear difference can be observed between the [20.8º; 24.0º] bump profile of sample 150rm-10mm-2h-PI and that of the remaining samples. This may suggest that either sample 150rpm-10mm-2h-PI has different phases, or the phases contributing to the bump are the same but with different weight fractions.

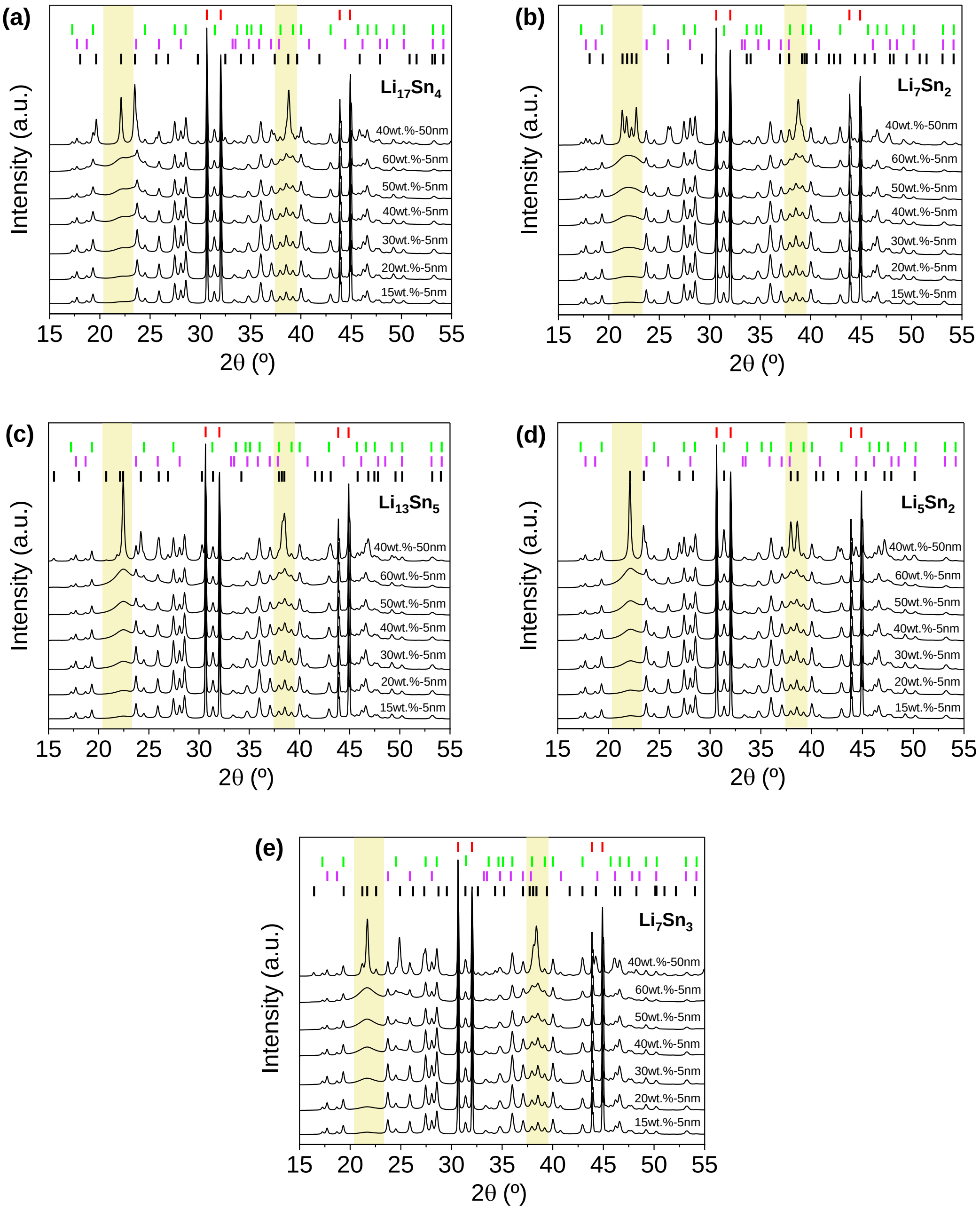

Figure 4.24 - Simulated diffractograms to test Li-rich Li-Sn intermetallic presence, for varying weight fraction and crystallite size: (a) Li$_{17}$Sn$_4$, (b) Li$_7$Sn$_2$, (c) Li$_{13}$Sn$_5$, (d) Li$_5$Sn$_2$, and (e) Li$_7$Sn$_3$. The patterns of for β-Sn (red), Li$_2$Sn$_5$ (pink), and LiSn (green) are displayed on top. In black, the pattern of the tested Li-rich intermetallic.

So, this simulation attempt confirms that, despite the conditions of the obtained experimental diffractograms (for which degradation occurs during data acquisition) and the complexity and similarity between the expected diffractograms of Li-rich Li-Sn intermetallics (which hinders their identification), some enlightenment can be obtained, and a more systematic simulation would be valuable for phase and crystallite size evaluation of the samples.

4.3.3. Powder phase evolution with milling time conclusions

XRD analysis allowed to disclose the reaction path leading to the final alloy microstructure and composition. The formation of Li-rich Li-Sn intermetallics in the disc-like particles, derived from the initial Li pieces, is simultaneously accompanied by the formation of the Sn-rich Li_2Sn_5 intermetallic on the original β-Sn powders. As milling progresses, both Li-rich and Sn-rich domains tend to evolve and transform towards the equilibrium phase LiSn. A final base LiSn composition, with Li_2Sn_5, and possibly with small crystallite size Li-rich Li-Sn intermetallics, is obtained. However, the results of DRX analysis, under the experimental conditions used (no portable controlled atmosphere sample holder), must be interpreted carefully and complemented with other techniques.

Both DSC and XRD analysis led to the conclusion that milling rate is the milling parameter presenting the major effect on reaction kinetics. The influence of milling ball diameter is not as pronounced. Such experimental observations agree with weight-normalized cumulative energy calculations, reinforcing the governing role of collision power and cumulative energy in determining the reaction kinetics of mechano-synthesis. Higher milling rates induce higher values of collision frequencies, energy transfer and peak temperature during collision events, which result in higher local temperatures, higher strain rates, and higher mechanical deformation of the powders. Enhanced diffusivity (due to local temperature increase), generation of crystal defects, and the balance between cold-welding and fracturing events among the powder particles, enhance the kinetics of the microstructural changes of the powder.

Regarding the samples milled with 500 rpm, milling experiments using 10 mm milling balls have revealed to be the best to produce the desired equimolar alloy. DSC analysis indicates that no remnant β-Sn remained after 0.5 h milling, whereas XRD results suggest that LiSn is the major phase present. However, no ascertained conclusions could be withdrawn regarding the presence of Li_2Sn_5, or Li-rich Li-Sn intermetallics.

4.4. Discussion Summary

In the present work, mechano-synthesis of an equimolar Li-Sn alloy proved to be successful. Milling efficiency of 50Sn-Li alloy has revealed to be considerable larger than of Li-Sn alloys with Li content below 25 at.% (< 20 % [16]). Overall, all milling experiments present milling mass yields above 40 %. As milling progresses, loss of process efficiency is observed due to material adhesion and cold-welding to the milling media. The main source of material loss is powder adhesion and cold-welding to the vial walls with a general increasing tendency with milling time. Adhesion, and cold-welding to the milling balls, accounts for less than 10% of the total mass loss. For the further explored 500rpm-10mm milling experiment series, where milling times up to 64 h were tested, a stationary $y_M \sim 86\%$ seems to be attained, indicating that balance is achieved between the kinetics of the mechanisms of adhesion and cold-welding, on one hand, and de-adhesion and fracture, on the other hand.

XRD and DSC analysis allowed to disclose the reaction path leading to the final alloy microstructure and composition. The formation of Li-rich Li-Sn intermetallics in the disc-like particles, derived from the initial Li pieces, is simultaneously accompanied by the formation of the Sn-rich Li_2Sn_5 intermetallic on the original β-Sn powders. As milling progresses, both Li-rich and Sn-rich domains tend to evolve and transform towards the equilibrium phase LiSn. A final base LiSn composition, with Li_2Sn_5, and possibly with small crystallite size Li-rich Li-Sn intermetallics, is obtained. Precise identification of Li-rich Li-Sn intermetallics on XRD diffractograms proved to be difficult due to the crystallographic properties of these phases and the experimental constraints of XRD data acquisition. As these Li-Sn intermetallics have melting points, or are involved in invariant transformations, outside the tested DSC temperature range, DSC analysis was not able to clarify which phases are present. Additional XRD diffractograms simulations carried out attested the complexity and similarity of Li-rich Li-Sn intermetallics, and the XRD low sensitivity towards these phase (for crystallite sizes of 5 nm, simulations disclosed a ~15 wt.% detection limit).

However, the results of DRX analysis, under the experimental conditions used, must be interpreted carefully, and complemented with other techniques. The preliminary XRD Context Study allowed to identify vulnerabilities in 50Li-Sn alloy characterization via XRD, when a portable controlled atmosphere sample stage is not available. XRD analysis, supported by complementary DSC analysis, revealed that an induced radiation damage process of the protective liquid paraffin coating is observed due to X-ray exposure. In addition, complementary GA analysis, disclosed that as degradation proceeds, Sn-enrichment in the vicinity of the metal-reaction layer interface reduces the X-rays beam depth of penetration (to 1.29 μm and to 1.55 μm, corresponding, respectively, to the θ incident angles of most intense LiSn and Li_2Sn_5 peaks) due to Sn high linear absorption coefficient [155]. As a result, LiSn and Li_2Sn_5 detectability decreases and XRD measurements become biased in favour of β-Sn phase. GA analysis, together with simulation of XRD diffractograms, demonstrated the incapacity of XRD technique to detect the formation of Li-air reaction products during 50Li-Sn degradation.

Regarding the influence of the milling parameters on milling efficiency, the stochastic nature of the mechano-synthesis process, together with the fact that only one milling experiment for each milling time was carried out, do not allow to draw trustworthy conclusions. On the other hand, both DSC and XRD analysis allowed to conclude that milling rate is the milling parameter presenting the major effect on reaction kinetics, and hence on the final microstructure and composition of an equimolar Li-Sn alloy. The influence of milling ball diameter is not as pronounced. DRX analysis indicates a lower kinetics for milling experiments with 150 rpm, agreeing with DSC analysis which confirmed the presence of unreacted β-Sn. Weight-normalized cumulative energy calculations indicate that milling experiments carried out at the same milling rate correspond to two distinct energy regions: 10-10^4 J/g for 150rpm, and 10^3-10^6 J/g for 500 rpm. For a constant milling rate, cumulative energy lies in the same energy region, independently of the milling ball diameter used. Such observations reinforce the governing role of collision power and cumulative energy in determining the reaction kinetics of mechano-synthesis [99,100].

Milling experiments at 500 rpm, using 10 mm milling balls, have revealed to be the best to produce the desired equimolar alloy. Upon 2 h milling, a quasi-steady state is achieved, with an almost stationary milling mass yield, $y_M \sim 86\%$, until 64 h of milling. XRD analysis disclosed that, shortly after 2 h milling, a steady state is achieved with all peak intensities (of β-Sn, Li_2Sn_5, and LiSn phases) being similar, with LiSn being the major phase present. DSC analysis indicates that no remnant β-Sn remained after 0.5 h milling. However, from powder phase composition characterization, no ascertained conclusions could be withdrawn regarding the presence of Li_2Sn_5, or small crystallite size Li-rich Li-Sn intermetallics due to the effect of sample degradation, XRD biased towards the β-Sn phase, and the limited temperature range of DSC analysis. Additional compositional characterization, through nuclear microprobe analysis, confirmed that the samples milled for 0.5 h, 2 h, 8 h, and 16 h present elemental homogeneity, with no Sn, nor Li rich zones observed, with Li widely spread in the samples. However, microprobe image pixel size of 3 x 3 μm^2 does not have sufficient resolution to distinguish between the formed Li-Sn intermetallics, LiSn and Li_2Sn_5, with mean crystallite size of ~50 nm, or even eventual smaller Li-rich Li-Sn intermetallics. μ-RBS-NRA quantitative elemental analysis of sample milled for 16 h yields an Li excess composition of 58Li-42Sn (at. %). This excess may be attributed to the limitations of the Li cross-sections published for the $^7Li(p,\alpha)^4He$ nuclear reaction used for Li quantification [149].

Chapter 5. Conclusions and Future Work

This chapter provides a closure to the thesis work. Section 5.1. Conclusions presents the main findings and conclusions of this work. Section 5.2. Future work addresses possible future routes of investigation to further developed the work of this thesis.

5.1. Conclusions

Mechano-synthesis of an equimolar Li-Sn alloy proved to be successful. Overall, all milling experiments present milling mass yields above 40 %, twice as much the values reported for Li-Sn alloys with Li content below 25 at.% (< 20 % [16]). The main source of material loss is powder adhesion and cold-welding to the vial walls with a general increasing tendency with milling time. Adhesion, and cold-welding to the milling balls, accounts for less than 10% of the total mass loss.

XRD and DSC analysis allowed to disclose the reaction path leading to the final targeted alloy microstructure and composition. Mechano-synthesis progresses in two fronts: Li-rich Li-Sn intermetallics preferentially form at the surface of the initial (Li) cuts, whereas Sn-rich Li-Sn intermetallics preferentially form at the surface of the original β-Sn powders. These two fronts converge, at a later stage, to a base LiSn composition, with Li_2Sn_5, and possibly with small crystallite size Li-rich Li-Sn intermetallics. Simulation of XRD diffractograms demonstrated that precise identification of Li-rich Li-Sn intermetallics on XRD diffractograms is a difficult task due to the crystallographic properties of these phases.

Under the experimental conditions used, the results of DRX analysis must be interpreted carefully and complemented with other techniques. The preliminary XRD Context Study allowed to identify vulnerabilities in sample characterization via XRD, when a portable controlled atmosphere sample stage is not available. XRD analysis, supported by complementary DSC analysis, revealed that an induced radiation damage process of the used protective liquid paraffin coating is observed due to X-ray exposure. In addition, complementary GA analysis, allowed the disclosure of XRD bias towards the β-Sn phase and its incapacity to detect the formation of Li-air reaction products during alloy degradation. The later was confirmed by XRD simulation.

As regards to the influence the milling parameters on the final microstructure of the equimolar Li-Sn alloy, both DSC and XRD analysis allowed to conclude that milling rate is the milling parameter presenting the major effect on reaction kinetics. The influence of milling ball diameter is not as pronounced. Weight-normalized cumulative energy calculations, and respective confrontation with the experimental observations, reinforce the governing role of collision power and cumulative energy in determining the reaction kinetics of mechano-synthesis [99,100].

Finally, milling experiments at 500 rpm, using 10 mm milling balls, have revealed to be the best to produce the desired equimolar alloy. Upon 2 h milling, a quasi-steady state is achieved, with an almost stationary milling mass yield, $y_M \sim 86\%$, up to 64 h milling. XRD and DSC analysis identified LiSn has the major phase present, whereas IBA analysis confirmed the elemental homogeneity, with no Sn, nor Li rich zones observed, with Li widely spread in the samples.

5.2. Future work

The successful identification of milling parameters (milling rate, and milling ball diameter), which result in both the highest milling mass yield and the most homogenous equimolar Li-Sn alloy, together with the gained comprehensive knowledge of the reaction path during mechano-synthesis, have laid the foundations for subsequent dilution of the equimolar Li-Sn alloy with pure Sn to produce Li-Sn alloys with Li content below 5 at.%. The wettability of these alloys on tungsten capillary porous systems (CPS) is aimed to be tested at the Dutch Institute for Fundamental Energy Research (DIFFER) and further exposed to deuterium plasmas in ISTTOK, sited at Instituto Superior Técnico (IST), and in MAGNUM-PSI facilities, sited at DIFFER, to evaluate the performance of said alloys as plasma facing components.

IBA analysis of samples from milling experiments with 500 rpm, using 10 mm balls, should be repeated, this time with a polarized particle detector and using a broad proton beam, so that alloy stoichiometry can be determined. To counter the observed surface roughness effect, for Sn, larger energy windows in RBS spectra (corresponding to Sn deeper analysis in the sample) should be considered.

Inductively Coupled Plasma – Optical Emission Spectrometry (ICP-OES) analysis of produced 50Li-Sn alloys would also provide information on the elemental composition, however studies on effective sample digestion methods are required. In the present work, two digestion methods (aqua regia and HNO_3, in an autoclave under 180 ºC, during 12h) were tested but were not successful.

The preliminary XRD Context Study demonstrated the necessity to design an air-tight argon-filled X-ray portable sample holder for sample full protection from degradation. Also, it allowed to identify knowledge gaps regarding Li-Sn alloys reactivity toward atmospheric gases, at NTP conditions, which would be interesting to explore. During the present work, development of a simple oxidation model to describe the evolution of phase fraction with time, during air exposure, has been initiated. Additional sample characterization, which could not be carried out in the present work, is required for better understanding of the oxidation process:

Scanning Electron Microscopy analysis of degraded 50Li-Sn alloy samples would provide valuable information on the powders' particle size and surface morphology of Li-air reaction products.

XRD analysis, using grazing incidence geometry, may allow the identification of the surface reaction product and its evolution with time. Also, the use of a portable controlled atmosphere sample holder would allow to ascertain the phase composition of the pristine milled powders.

Measurement of the specific surface area of the powders by means of the Brunauer-Emmett-Teller (BET) method, using Kr as an analysis gas, would be important to determine the specific mass gain (mg/cm^2) from GA analysis.

IBA analysis of 50Li-Sn powders exposed to air, at NTP conditions, would allow the identification of the formed Li-air reaction products (LiOH, Li_2CO_3, and/or Li_2O). Quantification of C and O would be made from their energy barriers detected in RBS. Direct quantification of hydrogen (^1H) would be accomplished through Elastic Recoil Detection Analysis (ERDA), an IBA technique soon to be available at IBA laboratory of IST.

Bibliography

[1] M.N. Obrovac, V.L. Chevrier, Alloy Negative Electrodes for Li-Ion Batteries, Chem. Rev. 114 (2014) 11444–11502. https://doi.org/10.1021/CR500207G.

[2] R.E. Nygren, F.L. Tabarés, Liquid surfaces for fusion plasma facing components—A critical review. Part I: Physics and PSI, Nucl. Mater. Energy. 9 (2016) 6–21. https://doi.org/10.1016/J.NME.2016.08.008.

[3] Z. Du, Z. Jiang, C. Guo, Thermodynamic optimizing of the Li-Sn system, Int. J. Mater. Res. 97 (2006) 10–16.

[4] F. Taubert, J. Seidel, R. Hüttl, M. Bobnar, R. Gumeniuk, F. Mertens, The heat capacity and entropy of the four lithium stannides Li17Sn4, Li7Sn2, Li13Sn5 and Li7Sn3 in the temperature range (2 to 865) K, J. Chem. Thermodyn. 130 (2019) 119–128. https://doi.org/10.1016/J.JCT.2018.09.035.

[5] T.L. Reichmann, C. Gebert, D.M. Cupid, Investigation of the Li solubility in the intermediate phase Li17Sn4 relevant to understanding lithiation mechanisms in Sn-based anode materials, J. Alloys Compd. 714 (2017) 593–602. https://doi.org/10.1016/J.JALLCOM.2017.04.232.

[6] R.A. Dunlap, D.A. Small, D.D. MacNeil, M.N. Obrovac, J.R. Dahn, Moessbauer effect investigation of the Li-Sn system, J. Alloys Compd. 289 (1999) 135–142. https://doi.org/10.1016/S0925-8388(99)00165-6.

[7] T.L. Reichmann, D. Li, D.M. Cupid, Heat capacities and an updated thermodynamic model for the Li–Sn system, Phys. Chem. Chem. Phys. 20 (2018) 22856–22866. https://doi.org/10.1039/C8CP04205E.

[8] J.P.S. Loureiro, H. Fernandes, F.L. Tabarés, G. Mazzitelli, C. Silva, R. Gomes, E. Alves, R. Mateus, T. Pereira, H. Figueiredo, H. Alves, Deuterium retention in tin (Sn) and lithium–tin (Li–Sn) samples exposed to ISTTOK plasmas, Nucl. Mater. Energy. 12 (2017) 709–713. https://doi.org/10.1016/j.nme.2016.12.026.

[9] Y. Nakajima, M. Kondo, T. Nozawa, Study on fabrication method of lithium alloys with metal grains, Fusion Eng. Des. 98–99 (2015) 2009–2014. https://doi.org/10.1016/j.fusengdes.2015.06.184.

[10] K. Natesan, W.E. Ruther, Fabrication and properties of a tin–lithium alloy, J. Nucl. Mater. 307–311 (2002) 743–748. https://doi.org/10.1016/S0022-3115(02)01221-7.

[11] F.L. Tabarés, E. Oyarzabal, A.B. Martin-Rojo, D. Tafalla, A. de Castro, F. Medina, M.A. Ochando, B. Zurro, K. McCarthy, Experimental tests of LiSn alloys as potential liquid metal for the divertor target in a fusion reactor, Nucl. Mater. Energy. 12 (2017) 1368–1373. https://doi.org/10.1016/J.NME.2016.11.026.

[12] R. Mateus, M.B. Costa, L.C. Alves, N. Catarino, R.C. da Silva, M. Dias, M. Guedes, A.C. Ferro, E. Alves, Ion beam analysis of Li-Sn alloys for fusion applications, in: Nucl. Instruments Methods Phys. Res. Sect. B Beam Interact. with Mater. Atoms, 2021: pp. 55–62. https://doi.org/10.1016/j.nimb.2020.09.019.

[13] R. Mateus, M.B. Costa, L.C. Alves, M. Guedes, E. Alves, A.C. Ferro, Lithium dilution in Li-Sn alloys, Nucl. Mater. Energy. 25 (2020). https://doi.org/10.1016/j.nme.2020.100783.

[14] M.B. Costa, R. Mateus, M. Guedes, A.C. Ferro, Mechanical alloying in the Li-Sn system, Mater. Lett. X. 6 (2020) 100045. https://doi.org/10.1016/j.mlblux.2020.100045.

[15] R. Mateus, M.B. Costa, L.C. Alves, M. Guedes, E. Alves, A.C. Ferro, Hampering deuterium retention in Li-Sn alloys, Nucl. Mater. Energy. (2020) 100783. https://doi.org/10.1016/j.nme.2020.100783.

[16] M.B. Costa, Development of Sn-Li alloys for application in Nuclear Fusion reactors, Instituto Superior Técnico, 2018.

[17] Technical data for the element Tin in the Periodic Table, (n.d.). https://periodictable.com/Elements/050/data.html (accessed October 18, 2021).

[18] D.D. Hillman, L.S. Chumbley, Characterization of tin oxidation products using sequential electrochemical reduction analysis (SERA), Solder. Surf. Mt. Technol. 18 (2006) 31–41. https://doi.org/10.1108/09540910610685420.

[19] M. Batzill, U. Diebold, The surface and materials science of tin oxide, Prog. Surf. Sci. 79 (2005) 47–154. https://doi.org/10.1016/j.progsurf.2005.09.002.

[20] B. Cornelius, S. Treivish, Y. Rosenthal, M. Pecht, The phenomenon of tin pest: A review, Microelectron. Reliab. 79 (2017) 175–192. https://doi.org/10.1016/j.microrel.2017.10.030.

[21] T. Sakai, A. Belyakov, R. Kaibyshev, H. Miura, J.J. Jonas, Dynamic and post-dynamic recrystallization under hot, cold and severe plastic deformation conditions, Prog. Mater. Sci. 60 (2014) 130–207. https://doi.org/10.1016/j.pmatsci.2013.09.002.

[22] S. Hotta, K. Matsumoto, T. Murakami, T. Narushima, C. Ouchi, Dynamic and static restoration behaviors of pure lead and tin in the ambient temperature range, Mater. Trans. 48 (2007) 2665–2673.

https://doi.org/10.2320/matertrans.MRA2007078.

[23] F. Thijssen, Effect of strain on microstructural evolution during dynamic recrystallization: Experiments on tin, 2004.

[24] M. Nagasaka, Strain-rate and temperature dependence of plastic deformation in white tin single crystals, Jpn. J. Appl. Phys. 38 (1999) 171–175. https://doi.org/10.1143/JJAP.38.171.

[25] P. Adeva, G. Caruana, O.A. Ruano, M. Torralba, Microstructure and high temperature mechanical properties of Tin, Mater. Sci. Eng. A. A194 (1995) 17–23. https://doi.org/10.4028/www.scientific.net/AMM.268-270.365.

[26] Cold and Hot Working Review of Materials - Engineers Edge, (n.d.). https://www.engineersedge.com/material_science/cold_hot_working.htm (accessed October 18, 2021).

[27] B. Zhou, T.R. Bieler, T.-K. Lee, W. Liu, Characterization of Recrystallization and Microstructure Evolution in Lead-Free Solder Joints Using EBSD and 3D-XRD, J. Electron. Mater. 42 (2013) 319–331. https://doi.org/10.1007/s11664-012-2307-z.

[28] I. Boguslavsky, P. Bush, Recrystallization principles applied to whisker growth in tin, in: APEX Conf March, 2003: pp. 1–14.

[29] Technical data for the element Lithium in the Periodic Table, (n.d.). https://periodictable.com/Elements/003/data.html (accessed October 18, 2021).

[30] S.-K. Otto, T. Fuchs, Y. Moryson, C. Lerch, B. Mogwitz, J. Sann, J. Rgen Janek, A. Henss, Storage of Lithium Metal: The Role of the Native Passivation Layer for the Anode Interface Resistance in Solid State Batteries, ACS Appl. Energy Mater. 4 (2021) 12798–12807. https://doi.org/10.1021/acsaem.1c02481.

[31] C. Naudin, J.L. Bruneel, M. Chami, B. Desbat, J. Grondin, J.C. Lassègues, L. Servant, Characterization of the lithium surface by infrared and Raman spectroscopies, J. Power Sources. 124 (2003) 518–525. https://doi.org/10.1016/S0378-7753(03)00798-5.

[32] E. Panabière, N. Emery, S. Bach, J.P. Pereira-Ramos, P. Willmann, Chemical stability of layered lithium cobalt nitrides in air, Corros. Sci. 58 (2012) 237–241. https://doi.org/10.1016/J.CORSCI.2012.01.032.

[33] K. Wang, P.N. Ross, F. Kong, F. McLarnon, The Reaction of Clean Li Surfaces with Small Molecules in Ultrahigh Vacuum: I. Dioxygen, J. Electrochem. Soc. 143 (1996) 422–428. https://doi.org/10.1149/1.1836460/XML.

[34] C.H. Skinner, R. Sullenberger, B.E. Koel, M.A. Jaworski, H.W. Kugel, Plasma facing surface composition during NSTX Li experiments, J. Nucl. Mater. 438 (2013) S647–S650. https://doi.org/10.1016/J.JNUCMAT.2013.01.136.

[35] W.R. Irvine, J.A. Lund, The Reaction of Lithium with Water Vapor, J. Electrochem. Soc. 110 (1963) 141. https://doi.org/10.1149/1.2425691/XML.

[36] M.M. Markowitz, D.A. Boryta, Lithium Metal-Gas Reactions., J. Chem. Eng. Data. 7 (2002) 586–591. https://doi.org/10.1021/JE60015A047.

[37] C. Lupu, J.G. Mao, J.W. Rabalais, A.M. Guloy, J.W. Richardson, X-ray and neutron diffraction studies on “Li4.4Sn,” Inorg. Chem. 42 (2003) 3765–3771. https://doi.org/10.1021/IC026235O.

[38] X. Wang, Z. Wen, X. Yang, B. Lin, Nanosized tin-based composite derived by in situ mechanochemical reduction for lithium ion batteries, Solid State Ionics. 179 (2008) 1238–1241. https://doi.org/10.1016/j.ssi.2008.01.049.

[39] J. Shi, Z. Wang, Y.Q. Fu, Density functional theory study of diffusion of lithium in Li–Sn alloys, J. Mater. Sci. 51 (2016) 3271–3276. https://doi.org/10.1007/s10853-015-9639-z.

[40] A.W. Overhauser, Crystal Structure of Lithium at 4.2 K, Phys. Rev. Lett. 53 (1984) 64–65. https://doi.org/10.1103/PhysRevLett.53.64.

[41] A. Masias, N. Felten, R. Garcia-Mendez, J. Wolfenstine, J. Sakamoto, Elastic, plastic, and creep mechanical properties of lithium metal, J. Mater. Sci. 54 (2019) 2585–2600. https://doi.org/10.1007/s10853-018-2971-3.

[42] J. Sangster, C.W. Bale, The Li-Sn (Lithium-Tin) system, J. Phase Equilibria. 19 (1998) 70–75. https://doi.org/10.1361/105497198770342788.

[43] J.F. Smith, Z. Moser, Thermodynamic properties of binary lithium systems - A review, J. Nucl. Mater. 59 (1976) 158–174. https://doi.org/10.1016/0022-3115(76)90131-8.

[44] D. Li, S. Fürtauer, H. Flandorfer, D.M. Cupid, Thermodynamic assessment and experimental investigation of the Li-Sn system, Calphad Comput. Coupling Phase Diagrams Thermochem. 47 (2014) 181–195. https://doi.org/10.1016/j.calphad.2014.09.002.

[45] J. Wang, J. Han, I.H. Jung, D. Bairos, P. Chartrand, Thermodynamic optimizations on the binary Li–Sn system and ternary Mg–Sn–Li system, Calphad Comput. Coupling Phase Diagrams Thermochem. 47 (2014) 100–113. https://doi.org/10.1016/J.CALPHAD.2014.07.001.

[46] P. Berger, H. Flandorfer, Enthalpy of mixing of liquid Li-Sb-Sn alloys, J. Mol. Liq. 298 (2020) 1–11. https://doi.org/10.1016/j.molliq.2019.112036.

[47] I. Courtney, J. Tse, O. Mao, J. Hafner, J. Dahn, Ab initio calculation of the lithium-tin voltage profile, Phys. Rev. B - Condens. Matter Mater. Phys. 58 (1998) 15583–15588. https://doi.org/10.1103/PhysRevB.58.15583.

[48] J.W. C., H. R. A., Thermodynamic study of the lithium-tin system, J. Electrochem. Soc. Electrochem. Sci. Technol. 128 (1976) 1181–1187. https://doi.org/10.1016/0022-5088(76)90245-9.

[49] M. Foster, C. Crouthamel, S. Wood, Thermodynamics of binary alloys. II. The lithium-tin system 1, J. Phys. Chem. 70 (1966) 3042–3045. https://doi.org/10.1021/j100882a004.

[50] W. Gasior, Z. Moser, W. Zakulski, Thermodynamic studies and the phase diagram of the Li-Sn system, J. Non. Cryst. Solids. 205–207 (1996) 379–382. https://doi.org/10.1016/S0022-3093(96)00446-2.

[51] M. Mayo, A.J. Morris, Structure Prediction of Li-Sn and Li-Sb Intermetallics for Lithium-Ion Batteries Anodes, Chem. Mater. 29 (2017) 5787–5795. https://doi.org/10.1021/acs.chemmater.6b04914.

[52] P. Zhang, Z. Ma, W. Jiang, Y. Wang, Y. Pan, C. Lu, Mechanical properties of Li-Sn alloys for Li-ion battery anodes: A first-principles perspective, AIP Adv. 6 (2016) 1–6. https://doi.org/10.1063/1.4940131.

[53] P. Zhang, Z. Ma, Y. Wang, Y. Zou, W. Lei, Y. Pan, C. Lu, A first principles study of the mechanical properties of Li-Sn alloys, RSC Adv. 5 (2015) 36022–36029. https://doi.org/10.1039/c5ra04685h.

[54] M.E. Stournara, P.R. Guduru, V.B. Shenoy, Elastic behavior of crystalline Li-Sn phases with increasing Li concentration, J. Power Sources. 208 (2012) 165–169. https://doi.org/10.1016/j.jpowsour.2012.02.022.

[55] J. Moon, K. Cho, M. Cho, Ab-initio study of silicon and tin as a negative electrode materials for lithium-ion batteries, Int. J. Precis. Eng. Manuf. 13 (2012) 1191–1197. https://doi.org/10.1007/s12541-012-0158-4.

[56] L. Bencze, D. Henriques, V. Motalov, T. Markus, Thermodynamic modelling of Li–Sn liquid alloy based on Knudsen effusion mass spectrometric measurements, J. Alloys Compd. 607 (2014) 183–192. https://doi.org/10.1016/J.JALLCOM.2014.03.166.

[57] ICDD Database Search Li22Sn5 – ICDD, (n.d.). https://www.icdd.com/pdfsearch/ (accessed October 12, 2021).

[58] ICDD Database Search Li17Sn4 – ICDD, (n.d.). https://www.icdd.com/pdfsearch/ (accessed October 12, 2021).

[59] T.B. Massalski, H. Okamoto, P.R. Subramanian, L. Kacprzak, Binary Alloy, Phase Diagrams, 2nd ed., ASM International: Materials Park, OH, 1996.

[60] J. Zemann, Crystal structures, 2 nd edition. Vol. 1 by R. W. G. Wyckoff, Acta Crystallogr. 18 (1965) 139–139. https://doi.org/10.1107/S0365110X65000361.

[61] W.J. Helfrich, R.A. Dodd, Densities and lattice parameters of tin (indium) solid solutions, Acta Metall. 12 (1964) 667–669. https://doi.org/10.1016/0001-6160(64)90039-2.

[62] C.S. Barret, T.B. Massalski, Structure of Materials, John Wiley & Sons, Ltd, 1966. https://doi.org/10.1002/CRAT.19810160904.

[63] G. Vincent, G. V Raynor, The lattice spacings of the primary solid solutions in magnesium of the metals of Group IIIB and of tin and lead, Proc. R. Soc. London. Ser. A. Math. Phys. Sci. 180 (1942) 107–121. https://doi.org/10.1098/RSPA.1942.0028.

[64] F. Zhang, J. Wang, S. Liu, Y. Du, Effects of the volume changes and elastic-strain energies on the phase transition in the Li-Sn battery, J. Power Sources. 330 (2016) 111–119. https://doi.org/10.1016/j.jpowsour.2016.08.136.

[65] D.A. Hansen, L.J. Chang, Crystal structure of Li 2 Sn 5, Acta Crystallogr. Sect. B Struct. Crystallogr. Cryst. Chem. 25 (1969) 2392–2395. https://doi.org/10.1107/s0567740869005760.

[66] W. Müller, H. Schäfer, Die Kristallstruktur der Phase LiSn, Zeitschrift Für Naturforsch. B. 28 (1973) 246–248. https://doi.org/10.1515/znb-1973-5-604.

[67] W. Müller, Darstellung und Struktur der Phase Li7Sn3 / Preparation und Crystal Structure of Li7Sn3, Zeitschrift Für Naturforsch. B. 29 (1974) 304–311. https://doi.org/10.1515/ZNB-1974-5-602.

[68] U. Frank, W. Müller, H. Schäfer, Die Struktur der Phase Li5Sn2 / The Crystal Structure of Li5Sn2, Zeitschrift Für Naturforsch. B. 30 (1975) 1–5. https://doi.org/10.1515/ZNB-1975-1-202.

[69] U. Frank, W. Müller, Darstellung und Struktur der Phase Li13Sn5 und die strukturelle Verwandtschaft der Phasen in den Systemen Li-Sn und Li-Pb / The Preparation and Crystal Structure of Li13Sn5 and the Structural Relations Between the Phases of the Systems Li-Sn and Li-Pb, Zeitschrift Für Naturforsch. B. 30 (1975) 316–322. https://doi.org/10.1515/ZNB-1975-5-605.

[70] U. Frank, W. Müller, H. Schäfer, Die Kristallstruktur der Phase Li7Sn2 / The Crystal Structure of Li7Sn2, Zeitschrift Für

Naturforsch. B. 30 (1975) 6–9. https://doi.org/10.1515/ZNB-1975-1-203.

[71] R. Berliner, O. Fajen, H.G. Smith, R.L. Hitterman, Neutron powder-diffraction studies of lithium, sodium, and potassium metal, Phys. Rev. B. 40 (1989) 12086. https://doi.org/10.1103/PhysRevB.40.12086.

[72] J.I. Gersten, F.W. Smith, The Physics and Chemistry of Materials, John Wiley & Sons, Ltd, New York, 2001.

[73] K. Ikeda, S. Terada, T. Mandai, K. Ueno, K. Dokko, M. Watanbe, Lithium-tin Alloy/Sulfur Battery with a Solvate Ionic Liquid Electrolyte, Electrochemistry. 83 (2015) 914–917.

[74] F. Robert, P.E. Lippens, J. Olivier-Fourcade, J.C. Jumas, F. Gillot, M. Morcrette, J.M. Tarascon, Mössbauer spectra as a “fingerprint” in tin-lithium compounds: Applications to Li-ion batteries, J. Solid State Chem. 180 (2007) 339–348. https://doi.org/10.1016/j.jssc.2006.10.026.

[75] F. Robert, P.E. Lippens, R. Fourcade, J.C. Jumas, F. Gillot, M. Morcrette, J.M. Tarascon, Mechanosynthesis and characterisation of the Li-Sn system, Hyperfine Interact. 167 (2006) 797–801. https://doi.org/10.1007/s10751-006-9360-z.

[76] C. Suryanarayana, Mechanical alloying and milling, Mech. Alloy. Milling. 46 (2004) 1–472. https://doi.org/10.4150/kpmi.2006.13.5.371.

[77] N. Llorca-Isern, C. Artieda-Guzmán, Metal-based composite powders, in: I. Chang, Y. Zhao (Eds.), Adv. Powder Metall. Prop. Process. Appl., Woodhead Publishing, 2013: pp. 241–272. https://doi.org/10.1533/9780857098900.2.241.

[78] C. Suryanarayana, Mechanical Alloying, in: Vol. 7 Powder Met. Technol. Appl., 1st ed., ASM International, 1998: pp. 193–194.

[79] P. Baláž, M. Achimovicová, M. Baláž, P. Billik, C.Z. Zara, J.M. Criado, F. Delogu, E. Dutková, E. Gaffet, F.J. Gotor, R. Kumar, I. Mitov, T. Rojac, M. Senna, A. Streletskii, W.C. Krystyna, Hallmarks of mechanochemistry: from nanoparticles to technology, Chem. Soc. Rev. 42 (2013) 7571–7637. https://doi.org/10.1039/C3CS35468G.

[80] B.S. Murty, S. Ranganathan, J.W. Yeh, P.P. Bhattacharjee, High-entropy alloys, 2nd ed., Elsevier, Amsterdam, 2019. https://doi.org/10.1016/C2017-0-03317-7.

[81] C. Suryanarayana, Recent Advances in the Synthesis of Alloy Phases by Mechanical Alloying/Milling, Met. Mater. 2 (1996) 195–209.

[82] C. Suryanarayana, A.A. Al-Joubori, Z. Wang, Nanostructured Materials and Nanocomposites by Mechanical Alloying: An Overview, Met. Mater. Int. 2021. (2021) 1–13. https://doi.org/10.1007/S12540-021-00998-5.

[83] H. Mio, J. Kano, F. Saito, Scale-up method of planetary ball mill, Chem. Eng. Sci. 59 (2004) 5909–5916. https://doi.org/10.1016/j.ces.2004.07.020.

[84] C. Burmeister, L. Titscher, S. Breitung-Faes, A. Kwade, Dry grinding in planetary ball mills: Evaluation of a stressing model, Adv. Powder Technol. 29 (2018) 191–201. https://doi.org/10.1016/J.APT.2017.11.001.

[85] C.F. Burmeister, A. Kwade, Process engineering with planetary ball mills, Chem. Soc. Rev. 42 (2013) 7660–7667. https://doi.org/10.1039/C3CS35455E.

[86] H.X. Kho, S. Bae, S. Bae, B.-W. Kim, J.S. Kim, Planetary Ball Mill Process in Aspect of Milling Energy, J. Korean Powder Metall. Inst. 21 (2014) 155–164. https://doi.org/10.4150/kpmi.2014.21.2.155.

[87] H. Mio, J. Kano, F. Saito, K. Kaneko, Optimum revolution and rotational directions and their speeds in planetary ball milling, Int. J. Miner. Process. 74 (2004) 85–92. https://doi.org/10.1016/j.minpro.2004.07.002.

[88] H. Mio, J. Kano, F. Saito, K. Kaneko, Effects of rotational direction and rotation-to-revolution speed ratio in planetary ball milling, Mater. Sci. Eng. A. 332 (2002) 75–80. https://doi.org/10.1016/S0921-5093(01)01718-X.

[89] X. Jiang, M.A. Trunov, M. Schoenitz, R.N. Dave, E.L. Dreizin, Mechanical alloying and reactive milling in a high energy planetary mill, J. Alloys Compd. 478 (2009) 246–251. https://doi.org/10.1016/J.JALLCOM.2008.12.021.

[90] S. Rosenkranz, S. Breitung-Faes, A. Kwade, Experimental investigations and modelling of the ball motion in planetary ball mills, Powder Technol. 212 (2011) 224–230. https://doi.org/10.1016/j.powtec.2011.05.021.

[91] M. Matsuoka, J. Hirata, S. Yoshizawa, Kinetics of solid-state polymorphic transition of glycine in mechano-chemical processing, Chem. Eng. Res. Des. 88 (2010) 1169–1173. https://doi.org/10.1016/J.CHERD.2010.01.011.

[92] A.S. Rogachev, D.O. Moskovskikh, A.A. Nepapushev, T.A. Sviridova, S.G. Vadchenko, S.A. Rogachev, A.S. Mukasyan, Experimental investigation of milling regimes in planetary ball mill and their influence on structure and reactivity of gasless powder exothermic mixtures, Powder Technol. 274 (2015) 44–52. https://doi.org/10.1016/j.powtec.2015.01.009.

[93] F. Baras, Q. Bizot, A. Fourmont, S. Le Gallet, O. Politano, Mechanical activation of metallic powders and reactivity of activated nanocomposites: a molecular dynamics approach, Appl. Phys. A. 127 (2021) 1–20.

https://doi.org/10.1007/S00339-021-04700-9.

[94] D.R. Maurice, T.H. Courtney, The physics of mechanical alloying: A first report, Metall. Trans. A. 21 (1990) 289–303. https://doi.org/10.1007/BF02782409.

[95] T.H. Courtney, Process Modeling of Mechanical Alloying (Overview), Mater. Trans. JIM. 36 (1995) 110–122. https://doi.org/10.2320/MATERTRANS1989.36.110.

[96] D. Maurice, T.H. Courtney, Milling dynamics: Part III. integration of local and global modeling of mechanical alloying devices, Metall. Mater. Trans. A. 27 (1996) 1981–1986. https://doi.org/10.1007/BF02651947.

[97] D. Maurice, T.H. Courtney, Modeling of mechanical alloying: Part II. Development of computational modeling programs, Metall. Mater. Trans. A 1995 269. 26 (1995) 2431–2435. https://doi.org/10.1007/BF02671257.

[98] M. Abdellaoui, E. Gaffet, Mechanical alloying in a planetary ball mill: kinematic description, J. Phys. IV. 4 (1994) 291–296. https://doi.org/10.1051/jp4:1994340.

[99] M. Abdellaoui, E. Gaffet, The physics of mechanical alloying in a planetary ball mill: Mathematical treatment, Acta Metall. Mater. 43 (1995) 1087–1098. https://doi.org/10.1016/0956-7151(95)92625-7.

[100] N. Burgio, A. Iasonna, M. Magini, S. Martelli, F. Padella, Mechanical alloying of the Fe-Zr system. Correlation between input energy and end products, Nuovo Cim. 13 (1991) 459–476. https://doi.org/10.1007/BF02452130.

[101] M. Magini, A. Iasonna, Energy Transfer in Mechanical Alloying (Overview), Mater. Trans. JIM. 36 (1995) 123–133. https://doi.org/10.2320/MATERTRANS1989.36.123.

[102] A. Iasonna, M. Magini, Power Measurements during Mechanical Milling. An Experimental way to investigate the energy transfer phenomena, Acta Mater. 44 (1996) 1109–1117.

[103] R. Watanabe, H. Hashimoto, G.G. Lee, Computer Simulation of Milling Ball Motion in Mechanical Alloying (Overview), Mater. Trans. JIM. 36 (1995) 102–109. https://doi.org/10.2320/MATERTRANS1989.36.102.

[104] F. Hirosawa, T. Iwasaki, Dependence of the dissipated energy of particles on the sizes and numbers of particles and balls in a planetary ball mill, Chem. Eng. Res. Des. 167 (2021) 84–95. https://doi.org/10.1016/J.CHERD.2020.12.024.

[105] K.C. Kim, T. Jiang, Y. Xu, N. Il Kim, H.S. Jin, J.C. Kim, Application of discrete element simulation in mechanical activation of boron concentrate, Powder Technol. 382 (2021) 441–453. https://doi.org/10.1016/J.POWTEC.2020.12.031.

[106] M. Broseghini, L. Gelisio, M. D'Incau, C.L. Azanza Ricardo, N.M. Pugno, P. Scardi, Modeling of the planetary ball-milling process: The case study of ceramic powders, J. Eur. Ceram. Soc. 36 (2016) 2205–2212. https://doi.org/10.1016/J.JEURCERAMSOC.2015.09.032.

[107] H. Ashrafizadeh, M. Ashrafizaadeh, Influence of processing parameters on grinding mechanism in planetary mill by employing discrete element method, Adv. Powder Technol. 23 (2012) 708–716. https://doi.org/10.1016/J.APT.2011.09.002.

[108] K. Chen, L. Wang, Y. Chen, Q. Wang, Molecular dynamics simulation of microstructure evolution and heat dissipation of nanoscale friction, Int. J. Heat Mass Transf. 109 (2017) 293–301. https://doi.org/10.1016/J.IJHEATMASSTRANSFER.2017.01.105.

[109] N.Q. Vo, J. Zhou, Y. Ashkenazy, D. Schwen, R.S. Averback, P. Bellon, Atomic Mixing in Metals Under Shear Deformation, JOM. 65 (2013) 382–389. https://doi.org/10.1007/S11837-012-0542-7.

[110] E.Q. Lin, L.S. Niu, H.J. Shi, Z. Duan, Molecular dynamics simulation of nano-scale interfacial friction characteristic for different tribopair systems, Appl. Surf. Sci. 258 (2012) 2022–2028. https://doi.org/10.1016/J.APSUSC.2011.04.117.

[111] F. Delogu, Forced chemical mixing in model immiscible systems under plastic deformation, J. Appl. Phys. 104 (2008) 1–7. https://doi.org/10.1063/1.2987476.

[112] S. Odunuga, Y. Li, P. Krasnochtchekov, P. Bellon, R.S. Averback, Forced Chemical Mixing in Alloys Driven by Plastic Deformation, Phys. Rev. Lett. 95 (2005) 1–4. https://doi.org/10.1103/PhysRevLett.95.045901.

[113] I.F. Vasconcelos, R.S. De Figueiredo, Driving mechanisms on mechanical alloying: experimental and molecular dynamics discussions, Nanostructured Mater. 11 (1999) 935–946. https://doi.org/10.1016/S0965-9773(99)00397-9.

[114] M. Abdellaoui, E. Gaffet, Physics of Mechanical Alloying in Planetary Ball Mill and the Horizontal Rod Mill: Kinematic Approach, Mater. Sci. Forum. 179–181 (1995) 339–344. https://doi.org/10.4028/WWW.SCIENTIFIC.NET/MSF.179-181.339.

[115] P.P. Chattopadhyay, I. Manna, S. Talapatra, S.K. Pabi, Mathematical analysis of milling mechanics in a planetary ball mill, Mater. Chem. Phys. 68 (2001) 85–94. https://doi.org/10.1016/S0254-0584(00)00289-3.

[116] S. Möller, D. Höschen, S. Kurth, G. Esser, A. Hiller, C. Scholtysik, C. Dellen, C. Linsmeier, A new high-throughput

focused mev ion-beam analysis setup, Instruments. 5 (2021) 1–13. https://doi.org/10.3390/instruments5010010.

[117] M. Jakšić, F. Paszti, A. Kotai, S. Fazinic, Instrumentation for PIXE and RBS, IAEA-TECDOC. 1190 (2000) 1–71. http://bib.irb.hr/prikazi-rad?rad=46529.

[118] C. Jeynes, M.J. Bailey, N.J. Bright, M.E. Christopher, G.W. Grime, B.N. Jones, V. V. Palitsin, R.P. Webb, “total IBA” - Where are we?, Nucl. Instruments Methods Phys. Res. Sect. B Beam Interact. with Mater. Atoms. 271 (2012) 107–118. https://doi.org/10.1016/j.nimb.2011.09.020.

[119] M. Nastasi, J. Mayer, Y. Wang, Backscattering Spectrometry, in: Ion Beam Anal. Fundam. Appl., 1st Editio, Taylor & Francis Group, LLC, Boca Raton, FL 33487-2742, 2014: pp. 3–78.

[120] M. Nastasi, J. Mayer, Y. Wang, Nuclear Reaction Analysis, in: Ion Beam Anal. Fundam. Appl., 1st Editio, Taylor & Francis Group, LLC, Boca Raton, FL 33487-2742, 2014: pp. 113–139.

[121] M. Nastasi, J. Mayer, Y. Wang, Elastic Recoil Detection Analysis, in: Ion Beam Anal. Fundam. Appl., 1st Editio, Taylor & Francis Group, LLC, Boca Raton, FL 33487-2742, 2014: pp. 79–112.

[122] W.A. Lanford, M. Parenti, B.J. Nordell, M.M. Paquette, A.N. Caruso, M. Mäntymäki, J. Hämäläinen, M. Ritala, K.B. Klepper, V. Miikkulainen, O. Nilsen, W. Tenhaeff, N. Dudney, D. Koh, S.K. Banerjee, E. Mays, J. Bielefeld, S.W. King, Nuclear reaction analysis for H, Li, Be, B, C, N, O and F with an RBS check, Nucl. Instruments Methods Phys. Res. Sect. B Beam Interact. with Mater. Atoms. 371 (2016) 211–215. https://doi.org/10.1016/j.nimb.2015.10.052.

[123] M. Nastasi, J. Mayer, Y. Wang, Particle-Induced X-Ray Emission Analysis, in: Ion Beam Anal. Fundam. Appl., 1st Editio, Taylor & Francis Group, LLC, Boca Raton, FL 33487-2742, 2014: pp. 141–170.

[124] N.P. Barradas, C. Jeynes, Advanced physics and algorithms in the IBA DataFurnace, Nucl. Instruments Methods Phys. Res. Sect. B Beam Interact. with Mater. Atoms. 266 (2008) 1875–1879. https://doi.org/10.1016/J.NIMB.2007.10.044.

[125] J.A. Maxwell, W.J. Teesdale, J.L. Campbell, The Guelph PIXE software package II, Nucl. Instruments Methods Phys. Res. Sect. B Beam Interact. with Mater. Atoms. 95 (1995) 407–421. https://doi.org/10.1016/0168-583X(94)00540-0.

[126] M. Graef, M. McHenry, Structure of Materials: an Introduction to Crystallography, Diffraction, and Symmetry, Cambridge University Press, Cambridge, 2007.

[127] J.A. Small, R.L. Watters, SRM 660c: Line Position and Line Shape Standard for Powder Diffraction, U.S. Department of Commerce: Gaithersburg, MD, 2015. https://www-s.nist.gov/srmors/certificates/660C.pdf.

[128] U. Wietelmann, Stabilized, pure lithium metal powder and method for producing the same, 2012.

[129] N. Doebelin, R. Kleeberg, IUCr, Profex: a graphical user interface for the Rietveld refinement program BGMN, Urn:Issn:1600-5767. 48 (2015) 1573–1580. https://doi.org/10.1107/S1600576715014685.

[130] T. Kawada, I; Isobe, M.; Okamura, F.P.; Watanabe, H.; Ohsumi, K.; Horiuchi, H.; Sato, T.; Ishii, Time-of-flight neutron diffraction study of Li3N at high temperature, Mineral. J. 13 (1986) 28–33.

[131] U. Ruschewitz, R. Poettgen, Structural phase transition in Li2 C2, Zeitschrift Fuer Anorg. Und Allg. Chemie. 625 (1999) 1599–1603.

[132] R. Pepinsky, Crystal Structure of Lithium Hydroxide Monohydrate, Zeitschrift Fuer Krist. Krist. Krist. Krist. 102 (1940) 119–140.

[133] J. Zemann, Die Kristallstruktur von Li2 C O3, Acta Crystallogr. 10 (1957) 664–666.

[134] W.H. Zachariasen, Untersuchungen ueber die Kristallstruktur von Sesquioxyden und Verbindungen A B O3, Skr. Utg. Av Det Nor. Videnskaps-Akademi i Oslo 1 Mat. Naturvidenskapelig Klasse. (1928) 1–165.

[135] R. Gilardi, J. Flippen-Anderson, C. George, R.J. Butcher, A New Class of Flexible Energetic Salts: The Crystal Structures of the Ammonium, Lithium, Potassium, and Cesium Salts of Dinitramide, J. Am. Chem. Soc. 119 (1997) 9411–9416.

[136] R.A. Young, The Rietveld Method, Oxford University Press, Oxford, 1995.

[137] L.B. Mccusker, R.B. Von Dreele, D.E. Cox, D. Louër, P. Scardi, Rietveld refinement guidelines, Urn:Issn:0021-8898. 32 (1999) 36–50. https://doi.org/10.1107/S0021889898009856.

[138] B.H. Toby, R.B. Von Dreele, GSAS-II: The genesis of a modern open-source all purpose crystallography software package, J. Appl. Crystallogr. 46 (2013) 544–549. https://doi.org/10.1107/S0021889813003531.

[139] B.H. Toby, International Tables for Crystallography, Volume H, Powder Diffraction, 1st Editio, Wiley, Chichester, 2019.

[140] Determining Profile Parameters from a Standard, (n.d.). https://subversion.xray.aps.anl.gov/pyGSAS/Tutorials/CWInstDemo/FindProfParamCW.htm (accessed December 3, 2021).

[141] Variable knife edge features | Rigaku Global Website, (n.d.).

https://www.rigaku.com/applications/bytes/xrd/miniflex/19550973 (accessed March 14, 2022).

[142] A.C. Larson, R.B. Von Dreele, eds., GSAS Technical Manual, Los Alamos, NM 87545, 2004.

[143] B.H. Toby, R factors in Rietveld analysis: How good is good enough?, Powder Diffr. 21 (2006) 67–70. https://doi.org/10.1154/1.2179804.

[144] Simulating Powder Diffraction, (n.d.). https://subversion.xray.aps.anl.gov/pyGSAS/Tutorials/Simulation/SimTutorial.htm (accessed February 7, 2022).

[145] F.H. Chung, Quantitative Interpretation of X-ray Diffraction Patterns of Mixtures. II. Adiabatic, J. Appl. Crystallogr. 7 (1974) 526–531.

[146] C.R. Hubbard, E.H. Evans, D.K. Smith, IUCr, The reference intensity ratio, I/Ic, for computer simulated powder patterns, Urn:Issn:0021-8898. 9 (1976) 169–174. https://doi.org/10.1107/S0021889876010807.

[147] K. Hildal, J.H. Perepezko, GA, in: Handb. Therm. Anal. Calometry, 2018: pp. 781–828.

[148] S.L. Molodtsov, A.F. Gurbich, C. Jeynes, Accurate ion beam analysis in the presence of surface roughness, J. Phys. D. Appl. Phys. 41 (2008) 1–7. https://doi.org/10.1088/0022-3727/41/20/205303.

[149] J.W. Mayer, E. Rimini, Ion Beam Handbook for Material Analysis, Academic Press, London, UK, 1977.

[150] G.C. Rosa, A.J. Souza, E. V. Possamai, H.J. Amorim, P.D. Neis, Wear analysis of ultra-fine grain coated carbide tools in hard turning of AISI 420C stainless steel, Wear. 376–377 (2017) 172–177. https://doi.org/10.1016/j.wear.2017.01.088.

[151] I. Barin, Thermochemical Data of Pure Substances, Third Ed., VCH Verlagsgesellschaft mbH, Weinheim, 1995.

[152] I. Brian, Thermochemical Data of Pure Substances, Third Ed., VCH Verlagsgesellschaft mbH, Weinheim, 1995.

[153] I. Barin, Thermochemical Data of Pure Substances, Third Ed., VCH Verlagsgesellschaft mbH, Weinheim, 1995.

[154] D.E. Bedolla, G. Birarda, S. Giannotta, V. Faoro, A. Cescato, L. Vaccari, A. Gianoncelli, Oxidation of ultralene and paraffin due to radiation damage after exposure to soft X-rays probed by FTIR microspectroscopy and X-ray fluorescence, Urn:Issn:1600-5775. 28 (2021) 231–239. https://doi.org/10.1107/S160057752001471X.

[155] NIST: X-Ray Mass Attenuation Coefficients - Tin, (n.d.). https://physics.nist.gov/PhysRefData/XrayMassCoef/ElemTab/z50.html (accessed April 26, 2022).

[156] H. Okamoto, Al-Li (Aluminum-Lithium), J. Phase Equilibria Diffus. 33 (2012) 500–5001. https://doi.org/10.1007/s11669-012-0119-8.

[157] K.S. Son, T.E. Park, J.S. Kim, S.M. Kang, T.H. Kim, D. Kim, Microstructural control of Al-Sn alloy with addition of Cu and Si, J. Korean Inst. Met. Mater. 48 (2010) 248–255. https://doi.org/10.3365/KJMM.2010.48.03.248.

[158] R. Hill, The elastic behaviour of a crystalline aggregate, Proc. Phys. Soc. 65 (1952) 349–354. https://iopscience.iop.org/article/10.1088/0370-1298/65/5/307/meta (accessed April 17, 2022).

Appendix A

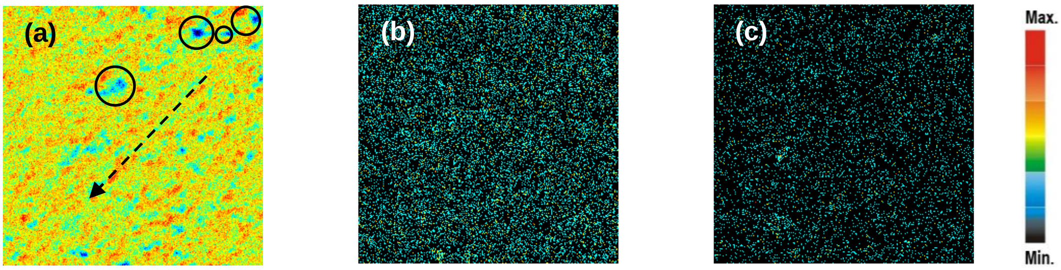

Sn, RBS

Li bulk, NRA

Li surface, NRA

Figure A.1 - Sample 500rpm-10mm-0.5h (Scan 2). 512 x 512 μm^2 maps of (a) Sn-RBS/ Sn map obtained from Sn barrier in RBS, (b) Li bulk NRA/ Li map obtained from Li barrier in NRA, and (c) Li surface NRA/ Li map obtained from Li barrier in NRA. Dashed arrows indicate the direction of the preferred orientation. Black circles indicate Sn-depleted regions.

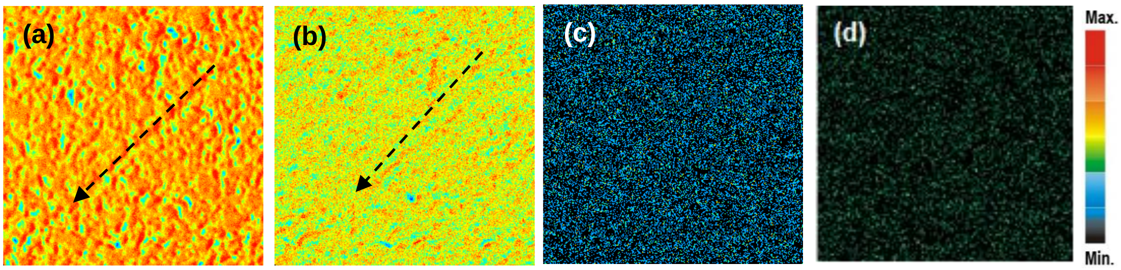

Sn-L_{α}, PIXE

Sn, RBS

Li bulk, NRA

Li surface, NRA

Figure A.2 – Sample 500rpm-10mm-2h (Scan 2). 512 x 512 μm^2 maps of (a) Sn-L_{α} PIXE/ Sn map obtained from Sn-L_{α} emission in PIXE spectra, (b) Sn-RBS/ Sn map obtained from Sn barrier in RBS, (c) Li bulk NRA/ Li map obtained from Li barrier in NRA, and (d) Li surface NRA/ Li map obtained from Li barrier in NRA. Dashed arrows indicate the direction of the preferred orientation.

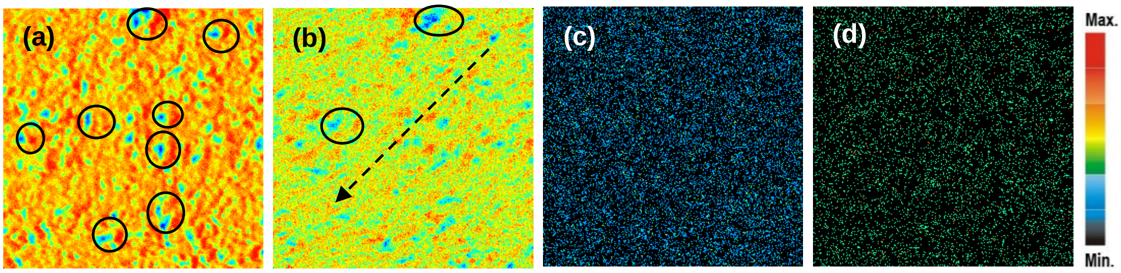

Sn-L_{α}, PIXE

Sn, RBS

Li bulk, NRA

Li surface, NRA

Figure A.3 - Sample 500rpm-10mm-8h (Scan 2). 512 x 512 μm^2 maps of (a) Sn-L_{α} PIXE/ Sn map obtained from Sn-L_{α} emission in PIXE spectra, (b) Sn-RBS/ Sn map obtained from Sn barrier in RBS, (c) Li bulk NRA/ Li map obtained from Li barrier in NRA, and (d) Li surface NRA/ Li map obtained from Li barrier in NRA. Dashed arrows indicate the direction of the preferred orientation. Black circles indicate Sn-depleted regions.

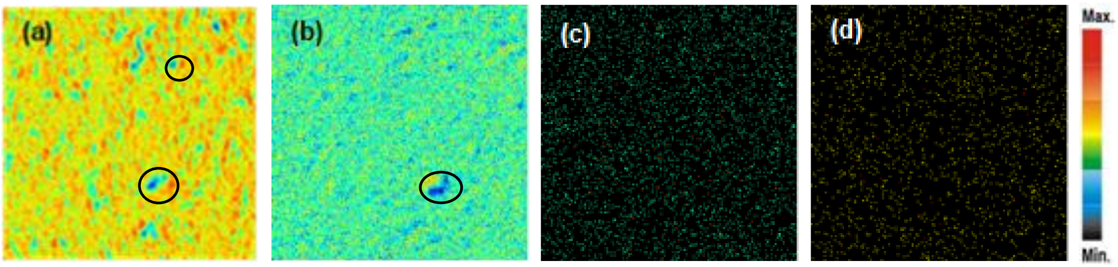

Sn-L_α, PIXE Sn, RBS Li bulk, NRA Li surface, NRA

Figure A.4 - Sample 500rpm-10mm-16h (Scan 2). 512 x 512 μm^2 maps of (a) Sn-L_α PIXE/ Sn map obtained from Sn-L_α emission in PIXE spectra, (b) Sn-RBS/ Sn map obtained from Sn barrier in RBS, (c) Li bulk NRA/ Li map obtained from Li barrier in NRA, and (d) Li surface NRA/ Li map obtained from Li barrier in NRA. Black circles indicate Sn-depleted regions.

Appendix B

The following line colour/type palette guideline is used: dark blue line - experimental data; green line - calculated diffractogram; red line - background function used; bottom light blue line - difference between the experimental and calculated diffractograms divided by the standard uncertainty of the experimental intensity measured at each 2θ value; light blue ticks - Li_2Sn_5; red ticks - LiSn, and dark blue ticks - β-Sn.

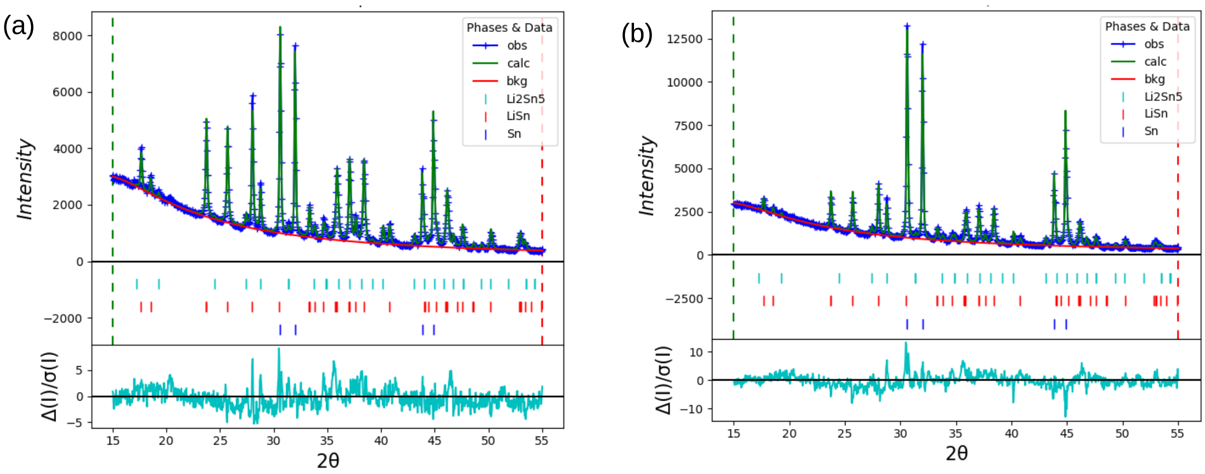

Figure B.1 - Experimental diffractograms of coated film sample exposed to X-ray and air for: (a) 11 min, and (b) 27 min, and their Rietveld analysis.

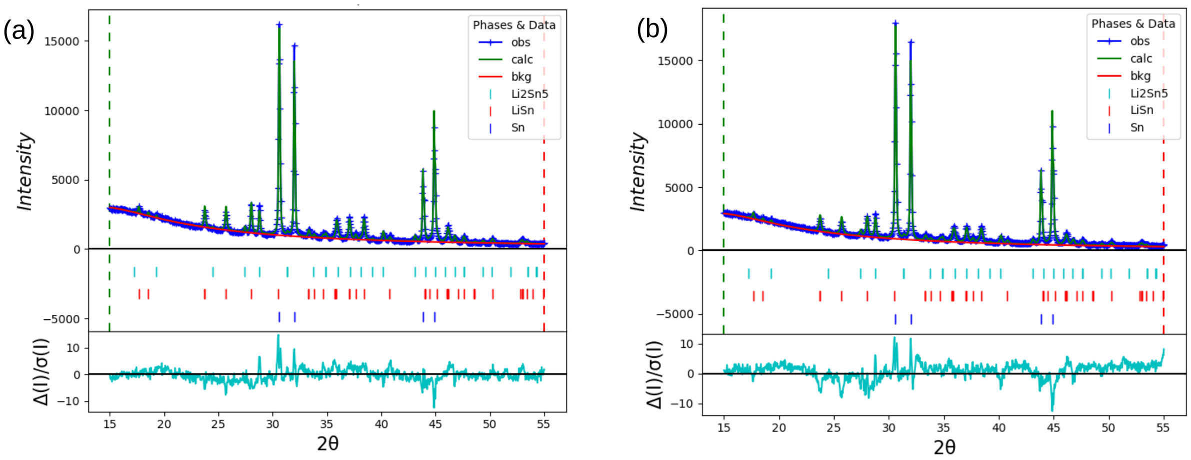

Figure B.2 - Experimental diffractograms of coated film sample exposed to X-ray and air for: (a) 43 min, and (b) 59 min, and their Rietveld analysis.

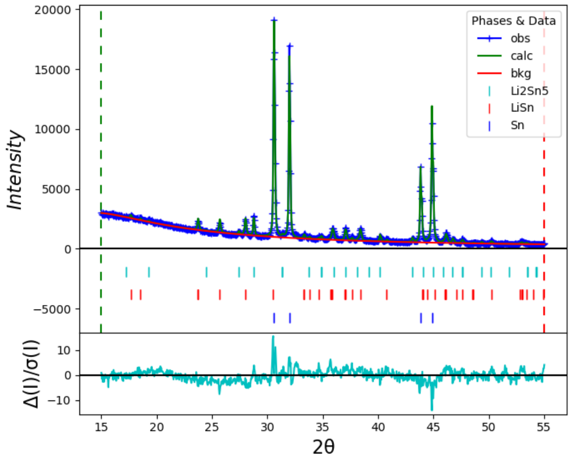

Figure B.3 - Experimental diffractogram of coated film sample exposed to X-ray and air for 75 min, and its Rietveld analysis.

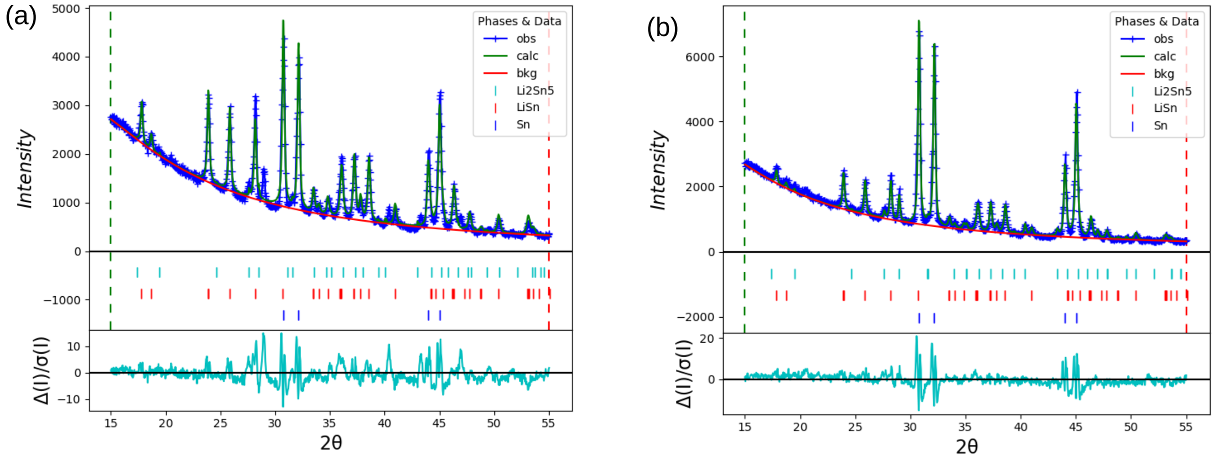

Figure B.4 - Experimental diffractograms of uncoated film sample exposed to X-ray and air for: (a) 10 min, and (b) 26 min, and their Rietveld analysis.

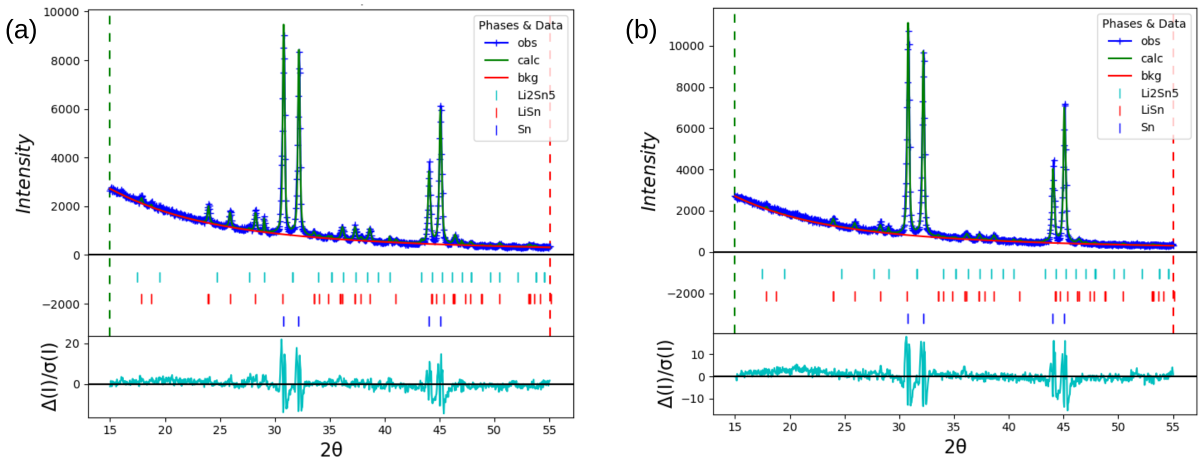

Figure B.5 - Experimental diffractograms of uncoated film sample exposed to X-ray and air for: (a) 42 min, and (b) 58 min, and their Rietveld analysis.

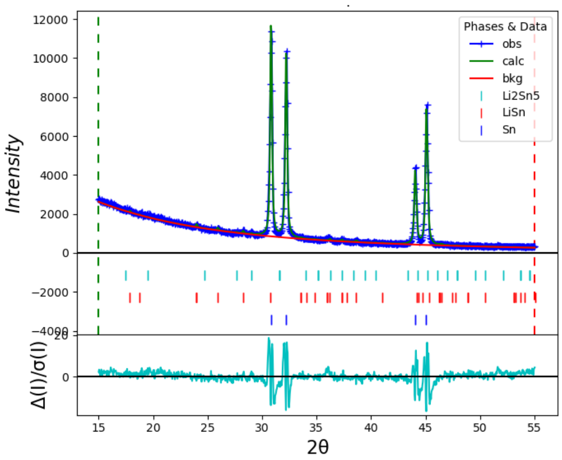

Figure B.6 - Experimental diffractogram of coated film sample exposed to X-ray and air for 74 min, and its Rietveld analysis.

Appendix C

Collision power and cumulative energy are proposed to play the governing role in determining the kinetics of MA [99,100]. The Abdellaoui and Gaffet mathematical model [99], based on the kinematic modelling of the planetary ball mill, for energy transfer from the milling system to the powders, was used to estimate the single ball-wall collision energy, E_b in J/hit (Equation C. 1); the single ball-wall collision frequency, f in s^{-1} (Equation C. 3), using as inputs the milling parameters for the operation and the geometric characteristics of the planetary mill used:

$$E_b = \frac{1}{2}\, m_b\, v_a \qquad \text{(Equation C. 1)}$$

$$V_a = \sqrt{(\omega_p R_d)^2 + \omega_v^2 (R_v - r_b)^2 (1 + 2\frac{\omega_v}{\omega_d})} \qquad \text{(Equation C. 2)}$$

$$f = \frac{1}{T_1 + T_2} \qquad \text{(Equation C. 3)}$$

Where m_b is the mass of the milling ball, and v_a the absolute velocity of the milling ball, after a detachment event (from the vial wall); v_a is calculated as a function of milling parameters (ω_d and ω_v, the disc and vial angular velocities, respectively), planetary mill and vial geometry (R_d and R_v the distance between the centre of the disc and the centre of the vial, and the vial radius, respectively) and milling ball radius (r_b) as given in (Equation C. 2). f in s^{-1} (Equation C. 3) is calculated recurring to T_1 and T_2, where T_1 is the period of time between ball detachment and collision event, and T_2 is the period of time between the first collision event and the next detachment event. Please consult the work of Abdellaoui and Gaffet [99] for a detailed explanation of the modelling of the planetary ball mill, and respective numerical resolution required for T_1 and T_2 calculation.

Burgio et al. [100] mathematical model was used to estimate the weight-normalized total collision power, P_t in W/g (Equation C. 4); and the weight-normalized cumulative energy transferred to the powders, E_{cum} in J/g (Equation C. 6):

$$P_t = \frac{\varphi_b N_b E_b f}{m_p} \qquad \text{(Equation C. 4)}$$

$$\varphi_b = 1 - \frac{N_b}{\pi (D_v - d_b) H_v / 3\, d_b^2} \qquad \text{(Equation C. 5)}$$

$$E_{cum} = P_t\, t \qquad \text{(Equation C. 6)}$$

where φ_b accounts for the degree of filling of the vial, N_b is the number of balls, and m_p is the mass of the powders. The degree of filling of the vial, φ_b, defined in (Equation C. 5), depends on D_v, the diameter of the vial; d_b, the diameter of the milling ball; and H_v, the height of the vial. The full deduction of the equations above can be seen in the work of *Burgio et al.* [100]. Table C. 1 compiles the intermediate calculations for estimate of cumulative energy transferred to the powders.

Table C. 1 – Intermediate calculations for estimate of cumulative energy transferred to the powders.

ω_d (rpm)	d_b (mm)	N_b	E_b (mJ/hit)	f (s^{-1})	P_t (W/g)	$t_{milling}$ (h)	E_{cum} (J/g)
150	6	34	1.56	7.48	0.13	0.5	235
						1	470
						2	640
						4	1879
						8	3759
						16	7518
						32	15036
						64	30072
	10	7	6.45	6.54	0.10	0.5	174
						1	349
						2	698
						4	1395
						8	2791
						16	5581
						32	11163
						64	22326
	15	2	18.93	6.14	0.07	0.5	138
						1	275
						2	550
						4	1101
						8	2201
						16	4403
						32	8806
						64	17612
500	6	34	17.37	24.62	4.77	0.5	8591
						1	17182
						2	34365
						4	68730
						8	137459
						16	274919
						32	549838
						64	1099676
	10	7	71.63	21.76	3.58	0.5	6453
						1	12906
						2	25811
						4	51622
						8	103244
						16	206488
						32	412977
						64	825954
	15	2	210.35	20.43	2.83	0.5	5085
						1	10171
						2	20341
						4	40682
						8	81364
						16	162728
						32	325457
						64	650913

ω_d – disc angular velocity, N_b – number of milling balls, E_b- single ball-wall collision energy, f – single ball-wall collision frequency, P_t - weight-normalized total collision power, $t_{milling}$ – milling time, E_{cum} – weight-normalized cumulative energy transferred to powders.